

Physical Modeling of Dust Polarization from Magnetically Enhanced Radiative Torque (MRAT) Alignment in Protostellar Cores with POLARIS

Nguyen Chau Giang,^{1,2} Thiem Hoang,^{1,2} Jeong-Gyu Kim,^{2,3} Le Ngoc Tram⁴

¹ Korea Astronomy and Space Science Institute, Daejeon 34055, Republic of Korea

² Korea University of Science and Technology, 217 Gajeong-ro, Yuseong-gu, Daejeon, 34113, Republic of Korea

³ National Astronomical Observatory of Japan, National Institutes of Natural Sciences, 2-21-1 Osawa, Mitaka, Tokyo 181-8588, Japan

⁴ Max-Planck-Institut für Radioastronomie, Auf dem Hügel 69, 53-121, Bonn, Germany

Accepted XXX. Received YYY; in original form ZZZ

ABSTRACT

Magnetic fields (\mathbf{B}) are an important factor that controls the star formation process. The leading method to observe \mathbf{B} orientation is using polarized thermal emission from dust grains aligned with \mathbf{B} . However, in dense environments such as protostellar cores, dust grains may have inefficient alignment due to strong gas randomizations, so that using dust polarization to trace \mathbf{B} is uncertain. Hoang & Lazarian (2016) demonstrated that the grain alignment by Radiative Torques is enhanced if dust grains contain embedded iron inclusions. Here we extend POLARIS code to study the effect of iron inclusions on grain alignment and thermal dust polarization toward a protostellar core, assuming uniform \mathbf{B} . We found that paramagnetic grains produce a low polarization degree of $p \sim 1\%$ in the envelope and negligible $p \ll 1\%$ in the central region due to the loss of grain alignment. In contrast, grains with a high level of iron inclusions have perfect alignment and produce high $p \sim 40\%$ in the envelope and low $p \leq 10\%$ in the central region. Grains with a moderate level of iron inclusions induce the polarization flipping from $\mathbf{P} \parallel \mathbf{B}$ at millimeter to $\mathbf{P} \perp \mathbf{B}$ at submillimeter due to the change in the internal alignment caused by slow internal relaxation. The weak alignment of very large grains of $a \geq 10 \mu\text{m}$ reduces dichroic extinction efficiency at submillimeter. We found a positive correlation between p and the level of iron inclusions, which opens a new window to constrain the abundance of solid iron locked in dust through dust polarimetry.

Key words: magnetic field, grain alignment, star formation, protostellar core

1 INTRODUCTION

Magnetic fields (\mathbf{B}) play an important role in controlling the star and planet formation in the Universe (McKee & Ostriker 2007, Crutcher 2012, Pattle & Fissel 2019). During the initial stage, they produce magnetic pressure that prevents the gravitational collapse of dense molecular clouds (Nakano & Nakamura 1978, Krumholz & Federrath 2019), but regulate the gas flow from the cloud inward to form denser structure called filament where stars can start to form (Seifried & Walch 2015). In the late phase, \mathbf{B} -fields help to launch outflows and jets due to magnetocentrifugal force, which reduces the angular momentum of protostellar disks and facilitates the growth of protostars (Shu et al. 1987, Allen et al. 2003, Frank et al. 2014).

Magnetic fields on the plane of sky are usually studied by the polarization of background starlight (Clemens et al. 2020) and polarized thermal emission from dust grains that align with the magnetic field direction (B-RAT) (see e.g., Pattle & Fissel 2019 for a review). The basic idea of such a method relies on the assumption that dust grains are aligned with the longest axis perpendicular to \mathbf{B} . As a result, thermal emission from aligned grains is polarized with the polarization vector (\mathbf{P}) perpendicular with magnetic field directions, i.e., $\mathbf{P} \perp \mathbf{B}$ (see Lazarian 2007; Andersson et al. 2015; Tram & Hoang 2022 for reviews). Then, by rotating \mathbf{P} by 90° , one can get the magnetic field morphology on the plane of sky. Moreover, the observed po-

larization pattern and polarization fraction contain both information of magnetic fields and dust properties in local environments (e.g., Planck Collaboration et al. 2015, Hensley & Draine 2021). Therefore, interpreting dust polarization is key to studying the roles of magnetic fields (Pattle & Fissel 2019, Hull et al. 2014) and dynamics of dust grains during the star and planet formation.

However, the question of how and where dust grains can be aligned with \mathbf{B} is the long-standing question in astrophysics. The process of grain alignment includes (1) the alignment of the axis of maximum moment of inertia ($\hat{\mathbf{a}}_1$) with the angular momentum \mathbf{J} , so-called internal alignment and (2) the alignment of \mathbf{J} with a preferred direction in space, so-called external alignment (e.g., \mathbf{B} , see Lazarian 2007). The leading mechanism for grain alignment is based on Radiative Torques (RATs, see Lazarian et al. 2015 and Andersson et al. 2015 for reviews). Dolginov & Mitrofanov (1976) first suggested that the interaction of an anisotropic radiation with a helical grain can induce RATs due to the differential scattering/absorption of left- and right-handed circularly polarized photons. The numerical calculations of RATs with three irregular shapes by using DDSCAT (Draine & Weingartner 1996) confirmed the efficient spin-up of dust grains by RATs, but the properties of RATs depend complexly on grain properties (e.g., grain shape, grain size). Lazarian & Hoang (2007) then introduced an Analytical Model (AMO) of RATs which

is based on a helical grain consisting of an oblate spheroid and a weightless mirror. The AMO is shown to reproduce the basic properties of RATs obtained from numerical calculations for irregularly shaped grains (Lazarian & Hoang 2007; Hoang & Lazarian 2008; Herranen et al. 2021), and enables us to make quantitative predictions of grain alignment by RATs with various conditions (Hoang & Lazarian 2014) and dust compositions (Hoang & Lazarian 2016b). Many observed optical-NIR polarization features of background stars in the interstellar medium (ISM) and toward molecular clouds (MCs) can be successfully explained by the dichroic extinction of aligned dust grains by RATs (see Andersson et al. 2015 for a review).

For polarized thermal emission from aligned dust grains, synthetic modeling of dust polarization based on solid grain alignment physics and radiative transfer is a unique way to accurately interpret observational data and constrain basic alignment theory and dust properties. The first attempts to model polarized thermal dust using the basic RAT theory (Lazarian & Hoang 2007) and radiative transfer are presented in Bethell et al. (2007) for a clumpy molecular cloud and Cho & Lazarian (2007) for an accretion disk. Later on, Reissl et al. (2016) developed the POLARized Radiation Simulator (POLARIS) code that combines the RAT alignment theory (Hoang & Lazarian 2014) and radiative transfer. POLARIS is based on the improved RAT theory for grains with ordinary paramagnetic material (PM grains) (Hoang & Lazarian 2014), which assumed that grains have fast internal relaxation due to various effects, including Barnett relaxation and inelastic relaxation (Purcell 1979). Such assumptions are well-known to be valid for the diffuse ISM and MCs where grains are small of sub-micron sizes and the randomization through gas-grain collisions is not strong enough to significantly affect the internal alignment (Lazarian 2007). Thus, POLARIS can be used to accurately model the RAT alignment and dust polarization to interpret observed dust polarization in these environments (Reissl et al. 2017; Seifried et al. 2018), especially for interpreting *Planck* polarization data at sub-millimeter and millimeter wavelengths (Reissl et al. 2020).

The measurements of dust polarization toward dense environments such as protostellar cores and protoplanetary disks are significantly improved thanks to the advanced interferometric observations by SMA, VLA, JVL, and especially ALMA. These observations reveal in detail the complex magnetic field morphology from the core scale of few thousands of au to the disk scale of few hundreds of au (see Cox et al. 2018, Pattle & Fissel 2019, Hull & Zhang 2019 for a review), and show many anomalous polarization features. The first anomalous feature is the detection of high polarization degree $p \sim 20 - 40\%$ in the envelope but low $p \sim 1\%$ in the central 100 au region of low mass Class 0/I young stellar objects (YSOs) by ALMA (Hull et al. 2014; Galametz et al. 2018; Cox et al. 2018). The maximum polarization fraction up to $p \sim 40\%$ detected in protostellar envelopes is twice times higher than the maximum $p \sim 20\%$ observed in the ISM by *Planck* (Collaboration et al. 2020). It is inconsistent with the prediction of reduced polarization level in protostellar environments due to the decrease of grain alignment efficiency at higher gas density due to stronger gas randomization (Hoang et al. 2021). Bethell et al. (2007) showed that the high polarization degree in dense environments can be due to the increase of maximum grain size. A theoretical study by Hirashita & Li (2013) showed that grains can grow to micron-size in dense clouds via the gas accretion and grain-grain collision. A recent study by Guillet et al. (2020) shows that the grain drift due to ambipolar diffusion and turbulence can increase grain growth and form $\sim 1 - 10 \mu\text{m}$ grains in protostellar cores. Observations by Kwon et al. (2009) and Galametz et al. (2019) reported the evidence for the presence of very large grains (VLGs) of size $a > 10 \mu\text{m}$ in both the protostellar envelopes and protostellar

disks around Class 0 YSOs. The modelling with current version of POLARIS by Valdivia et al. (2019) also showed that grains must grow to $a > 50 \mu\text{m}$ and are efficiently aligned with \mathbf{B} to reproduce the detected level of polarization toward Class 0 YSOs. However, whether large grains can maintain their magnetic alignment in such high gas collision environments is still not well clarified.

The rapid decrease of $p \sim 20 - 40\%$ in the envelope to $p \sim 1\%$ toward protostars, termed as polarization hole, is another anomalous feature because it is inconsistent with the prediction of higher polarization degree toward the radiation source in the RAT theory. The origin of the polarization hole is still unclear. Kataoka et al. (2012) suggested the polarization hole due to the increase in the toroidal component caused by the collapse of rotating protostellar cores and the effect of inclined magnetic fields. Brauer et al. (2016) suggested it is due to the extinction by aligned VLGs. Hoang et al. (2021) found that the removal of large grains by RAdiative Torque Disruption (RAT-D) around the protostar also can reduce polarized thermal emission from the central region. However, whether VLGs can efficiently have the magnetic alignment in dense protostellar environments is still not well studied.

Another anomalous feature is the 90 degrees flipping of the polarization pattern with wavelengths detected in two Class 0 YSOs NGC1333-IRAS4A (Liu et al. 2016, Ko et al. 2020) and OMC-3/MMS 6 (Liu 2021), and the MC NGC 2071 (Fanciullo et al. 2022). The origin of the polarization flipping is unclear. Ko et al. (2020) and Liu (2021) assigned the polarization flipping in two dense protostellar cores to the change of the polarization mechanism from dichroic emission to dichroic extinction by aligned dust grains. For the MC NGC 2071, Fanciullo et al. (2022) suggested this feature may arise from the change of the grain alignment direction from magnetic fields to radiation fields, i.e., k-RAT, or the change of the internal alignment direction due to slow internal relaxation (Hoang et al. 2022). Understanding the physical mechanisms of the dust polarization signal is crucially important for us to understand whether dust polarization can trace \mathbf{B} -fields in a given astrophysical environments. And if yes, in what conditions we can rotate the thermal dust polarization \mathbf{P} by 90° to obtain \mathbf{B} -fields.

Recently, Le Gouellec et al. (2020) interpreted ALMA polarization data of a dozen Class 0 YSOs (Hull et al. 2014) by post-processing non-ideal magnetohydrodynamic (MHD) simulations of protostellar cores with the current version of POLARIS to perform synthetic observations of dust polarization produced by aligned dust grains. They found that the model of RATs currently implemented in POLARIS produces a much lower polarization degree than values measured by ALMA. However, the observational data can be reproduced by the model with fixed perfect grain alignment, revealing the efficient grain alignment in protostellar cores. But how grains can achieve perfect alignment in such dense environments remains unknown.

Within the RAT paradigm, theoretical studies by Lazarian & Hoang (2008) and detailed numerical calculations by Hoang & Lazarian (2016b) showed that grains with embedded iron inclusions, i.e., superparamagnetic material (SPM), can be efficiently aligned with \mathbf{B} due to the combined effect of RATs and enhanced magnetic relaxation, which is termed as Magnetically Enhanced RAdiative Torque (MRAT) alignment. Recently, Hoang (2022) and Hoang et al. (2022) carried out detailed analytical studies on the effect of iron inclusions on grain alignment in protostellar cores and disks. They found that in protostellar cores and disks, only SPM grains can be efficiently aligned with \mathbf{B} due to the enhanced internal alignment (IA) and enhanced Larmor precession by iron inclusions. VLGs can be aligned with \mathbf{B} and can even have perfect alignment in protostellar environments if they contain a very high level of iron inclusions and

produce high levels of dust polarization. Such a sensitive correlation between the level of iron inclusions locked inside dust grains and observed polarization fraction provides a new avenue for constraining iron abundance in dust, which is still a mystery now.

The modelling of dust polarization by Lam et al. (2021) also found that micron-sized grains of $a \sim 1 \mu\text{m}$ must have the magnetic susceptibility enhanced by a factor of ~ 20 compared to PM to reproduce the observed $p \sim 1\%$ in the central regions of ten Class 0 YSOs by ALMA (Cox et al. 2018). The modelling with POLARIS by Valdivia et al. (2019) concluded that grains must grow to $a > 50 \mu\text{m}$ to reproduce observed $p > 1\%$ toward protostellar cores. It indirectly implies that VLGs around Class 0 YSOs must be SPM with a high level of iron inclusions.

However, the study by Lam et al. (2021) simply considered the perfect alignment for grains with the Larmor precession timescale being shorter than the gas damping timescale (Hoang & Lazarian 2016b), instead of accounting for grain alignment physics. Furthermore, Lam et al. (2021) and Valdivia et al. (2019) did not consider the effect of internal alignment, which is crucially important for VLGs in protostellar environments. Hoang (2022) and Hoang et al. (2022) showed that in contrast to the diffuse ISM and MCs where sub-micron grains always have efficient IA by fast internal relaxation, large grains in dense environments tend to have inefficient IA due to slow internal relaxation as a result of the stronger gas randomization. In contrast to grains with fast internal relaxation, with the grain major axis of inertia moment $\hat{\mathbf{a}}_1$ always parallel to \mathbf{J} , i.e., $\hat{\mathbf{a}}_1 \parallel \mathbf{J}$ (right IA), grains with slow internal relaxation do not have well-defined IA. A numerical study for grains without internal relaxation by Hoang & Lazarian (2009) found that grains aligned at high- J attractors (see Section 3.3 of grain alignment theory by RATs for details) still can have right IA due to the spinning torques by RATs, but grains at low- J attractors may have right or wrong IA. In the latter case, grains will align with $\hat{\mathbf{a}}_1$ perpendicularly to \mathbf{B} and radiate polarized emission with $\mathbf{P} \parallel \mathbf{B}$. The conditions that support the internal alignment of grains with slow internal relaxation are not well studied. It thus raises the uncertainty on determining the orientation between polarization vectors arising from the emission of aligned dust grains and the magnetic field direction.

Hoang (2022) and Hoang et al. (2022) found that the presence of grains with slow internal relaxation is reduced with increasing the fraction of iron locked inside dust grains. It implies the crucial role of iron inclusions in determining both the internal alignment direction and the grain alignment efficiency in dense environments. However, the current version of POLARIS only includes the RAT mechanism for paramagnetic grains. The dependence of grain alignment on the magnetic properties of grains and the presence of grains with slow internal relaxation are not taken into account in POLARIS. Thus, up to date, no detailed numerical modeling of dust polarization that takes the effect of iron inclusions and the co-existence of grains with fast and slow internal relaxation have been performed. This leaves a big gap between theory and observations and limits the diagnostic power of dust polarimetry.

To connect theory to observations and extend the power of POLARIS on studying magnetic fields and dust physics in dense and dynamic environments around protostars, we include the magnetic susceptibility and the detailed grain alignment physics with the MRAT mechanism into the code. To demonstrate the capability of our implementation, we simulate the polarized thermal emission from a protostellar core. We adopt a simple Bonnor-Ebert sphere and a uniform magnetic field to isolate the effect of iron inclusions on grain alignment and dust polarization by aligned dust grains. In subsequent publications, we will use the updated POLARIS code to perform in

detail the synthetic modeling of dust polarization toward protostellar cores and protostellar disks with more realistic \mathbf{B} -fields and gas density distribution from MHD simulations.

Our paper is organized as follows. We first describe the magnetic properties of grains in Section 2. Then, we describe the fundamental mechanisms of the internal and external grain alignment, and the main points of the external alignment by RATs for grains with iron inclusions in Section 3. The improvements of POLARIS, the model setup, and the numerical results of grain alignment in the protostellar core are given in Sections 4 and 5, respectively. We then show the results for the effect of iron inclusions on the polarization pattern in Section 6, the intensity-dependent polarization degree in Section 7, the efficiency of polarization by dichroic extinction of aligned VLGs in Section 8, and the wavelength-dependent polarization degree in Section 9. Implications of our results for observations and the summary of our main findings are presented in Sections 10 and 11, respectively.

2 MAGNETIC PROPERTIES OF DUST GRAINS

2.1 Paramagnetic material

Dust grains with diffusely embedded iron atoms (e.g., silicate) are called PM due to the existence of unpaired electrons. The magnetic susceptibility of PM grains of temperature T_d in a static magnetic field is given by the Curie's law:

$$\chi_{\text{pm}}(0) = \frac{n f_p \mu^2}{3 k_B T_d} = 0.006 n_{23} f_{p,-1} \hat{p}^2 T_{d,1}^{-1} \quad (1)$$

where n is the atomic density of grain material, f_p is the fraction of iron atoms within the grain, $\mu = p \mu_B = g_e \sqrt{J(J+1)} \mu_B$ is the magnetic moment per iron atom with $g_e \approx 2$ the electron-Lande factor, J the angular momentum quantum number of electron in the outer partially filled shell, μ_B the Bohr magneton, and k_B is the Boltzmann constant and T_d the dust temperature (see Draine & Weingartner 1996). In the numerical form, $n_{23} = n / (10^{23} \text{ cm}^{-3})$, $f_{p,-1} = f_p / 0.1$, $\hat{p} = p / 5.5$, and $T_{d,1} = T_d / (10 \text{ K})$ (Draine & Weingartner 1996).

If the external magnetic field varies with time at frequency ω , electron spins inside PM cannot respond immediately to the change in the external field, resulting in the phase lag that dissipates magnetic energy into thermal energy of grains. **The phase lag of electron spins at frequency ω and the energy dissipation of electromagnetic waves are characterized by the imaginary part of the magnetic susceptibility of dust grains, χ_2 , which is given by (see e.g., Hoang & Lazarian 2016b):**

$$\chi_{2,\text{pm}}(\omega) = \frac{\chi_{\text{pm}}(0) \omega \tau_{\text{el}}}{[1 + (\omega \tau_{\text{el}}/2)^2]^2}, \quad (2)$$

where $\tau_{\text{el}} \approx 2.9 \times 10^{-12} (f_p n_{23})^{-1} \text{ s}$ is the spin-spin relaxation timescale of electron spins (Draine 1996).

2.2 Superparamagnetic material

Beside being distributed diffusely inside dust grains, iron atoms also can be embedded in the form of clusters (Jones & Spitzer 1967). Each iron cluster can be considered as a giant magnetic moment, and the presence of many iron clusters will enhance the magnetic susceptibility of grains and make them SPM. Assuming that each cluster contains N_{cl} iron atoms, the magnetic moment of each cluster is given by $m = N_{\text{cl}} \mu$ with μ the magnetic moment of each iron atom.

The magnetic susceptibility of SPM at zero frequency $\chi_{\text{spm}}(0)$ is then given by (Hoang & Lazarian 2016b):

$$\begin{aligned}\chi_{\text{spm}}(0) &= \frac{n_{\text{cl}} m^2}{3k_B T_d} = \frac{N_{\text{cl}} \phi_{\text{sp}} \mu^2}{4\pi a_{\text{iron}}^3 k_B T_d} \\ &\approx 0.52 N_{\text{cl},3} \phi_{\text{sp},-2} \bar{\rho}^2 T_{d,1}^{-1},\end{aligned}\quad (3)$$

where $n_{\text{cl}} = N/V$ is the number of iron cluster per unit volume. $N = (\phi_{\text{sp}}/N_{\text{cl}})(a_{\text{eff}}/a_{\text{iron}})^3$ is the total number of iron clusters with ϕ_{sp} the volume filling factor of iron clusters, a_{eff} the effective radius of grains (see Section 3), $a_{\text{iron}} = 1.26 \times 10^{-4} \mu\text{m}$ the radius of an iron atom, and $V = (4/3)\pi a_{\text{eff}}^3$ the grain volume. In the numerical form, $N_{\text{cl},3} = N_{\text{cl}}/10^3$, $\phi_{\text{sp},-2} = \phi_{\text{sp}}/0.01$.

Similar to PM grains, the imaginary part of the magnetic susceptibility of SPM grains at frequency ω is given by (Hoang & Lazarian 2016b):

$$\chi_{2,\text{spm}}(\omega) = \frac{\chi_{\text{spm}}(0)\omega\tau_{\text{sp}}}{[1 + (\omega\tau_{\text{sp}}/2)^2]^2}, \quad (4)$$

where $\tau_{\text{sp}} = \nu_0^{-1} \exp(N_{\text{cl}} T_{\text{act}}/T_d)$ with $\nu_0 = 10^9 \text{s}^{-1}$ and $T_{\text{act}} = 0.011 \text{K}$ is the timescale for SPM to undergo thermally activated remagnetization (Morrish 2001).

The magnetic susceptibility at zero frequency of PM and SPM grains decreases with increasing dust temperature due to increasing thermal fluctuations of electron spins. In addition, the magnetic susceptibility at frequency ω decreases when the oscillation rate of magnetic field is larger than the inverse of the relaxation timescale of spin systems, i.e., $\omega \gtrsim 2/\tau_{\text{el}}$ (for PM grains) and $\omega \gtrsim 2/\tau_{\text{sp}}$ (for SPM grains).

3 PHYSICS OF GRAIN ALIGNMENT

In this section, we briefly describe the physics of grain alignment that includes the internal and external alignment (see Lazarian et al. 2015 and Andersson et al. 2015 for reviews). The internal alignment brings the angular momentum \mathbf{J} and the angular velocity $\mathbf{\Omega}$ to align with the major axis of inertia moment in which grains have the lowest rotational energy level. The external alignment brings \mathbf{J} to align with some preferred direction (i.e., magnetic field, radiation field, or gas flow) that allows grains to radiate polarized thermal emission (see Hoang et al. 2022 for more details). In our paper, we focus on modeling the alignment of grains with iron inclusions with magnetic fields using the MRAT model (Hoang & Lazarian 2016b). We first describe the damping timescale due to the random gas-grain collisions, then the mechanisms and the corresponding timescales for the internal and external alignment by RATs and magnetic relaxation.

3.1 Gas damping timescale

We consider an oblate spheroidal grain with the principal axes $\hat{\mathbf{a}}_1, \hat{\mathbf{a}}_2, \hat{\mathbf{a}}_3$ with the corresponding semi-minor axis of length c and the semi-major axes of length a (see Figure 1). The minor axis $\hat{\mathbf{a}}_1$ has the maximum inertia moment of $I_{\parallel} = I_1 = 8\pi/15 \rho s a^5$ and the major axes $\hat{\mathbf{a}}_2, \hat{\mathbf{a}}_3$ have the minimum inertia moment of $I_{\perp} = I_2 = I_3 = 4\pi/15 \rho s (1 + s^2) a^5$ with ρ the dust mass density and $s = c/a < 1$ the axial ratio. The ratio of the maximum and minimum inertia moment is $h = I_{\parallel}/I_{\perp} = 2/(1 + s^2)$. All notations used in our study are summarized in Table 1.

Atoms and molecules with Brownian motion colliding with a grain only increase the grain rotational energy, but do not increase the grain angular momentum due to the averaging effect. Subsequently, their

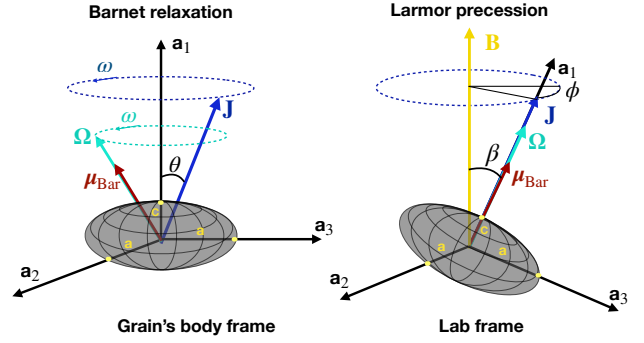


Figure 1. Left panel: Illustration of the internal alignment due to Barnett relaxation viewed from the grain's body frame. The precession of the angular momentum \mathbf{J} and angular velocity $\mathbf{\Omega}$ around the major axis of inertia moment $\hat{\mathbf{a}}_1$ at the precession rate ω induces the precession of the magnetic moment μ_{Bar} gained by the Barnett effect around $\hat{\mathbf{a}}_1$. The rotating magnetization induces the dissipation of rotational energy, leading to the alignment of \mathbf{J} and $\mathbf{\Omega}$ (and also μ_{Bar}) with $\hat{\mathbf{a}}_1$. Right panel: Illustration of Larmor precession due to the magnetic torques caused by the interaction between μ_{Bar} and \mathbf{B} . For the external alignment by magnetic relaxation, the rotating magnetic moment induces the dissipation of rotational energy that leads to the alignment between \mathbf{J} and \mathbf{B} .

evaporation from the grain surface takes away the grain angular momentum and makes grains rotate slower with time (e.g., Draine & Weingartner 1996). The gas damping timescale is given by (see e.g., Hoang et al. 2022):

$$\begin{aligned}\tau_{\text{gas}} &= \frac{3}{4\sqrt{\pi}} \frac{I_{\parallel}}{1.2 n_{\text{H}} n_{\text{H}} v_{\text{th}} a^4 \Gamma_{\parallel}} \\ &\approx 0.083 \hat{\rho} \left(\frac{s a_{-5}}{n_{\text{H},8} T_{\text{gas},1}^{1/2} \Gamma_{\parallel}} \right) \text{yr},\end{aligned}\quad (5)$$

where n_{H} is the number density of hydrogen atom, $v_{\text{th}} = \sqrt{2k_B T_{\text{gas}}/m_{\text{H}}}$ is the thermal velocity with T_{gas} the gas temperature, $\hat{\rho} = (\rho/3 \text{g cm}^{-3})$, and Γ_{\parallel} is the geometrical factor of unity (Roberge et al. 1993, Hoang & Lazarian 2016b, Hoang et al. 2022). We obtain $\Gamma_{\parallel} = 0.62$ for an oblate spheroidal with $s = 1/2$. In the above, $a_{-5} = a/(10^{-5} \text{cm})$, $n_{\text{H},8} = n_{\text{H}}/(10^8 \text{cm}^{-3})$, and $T_{\text{gas},1} = T_{\text{gas}}/(10 \text{K})$.

3.2 Internal Alignment by the Barnett Relaxation

In the rest state, grains with embedded iron atoms have no magnetic moment due to the random orientation of electron spins. When they rotate at $\mathbf{\Omega}$, the rotational energy can force all electron spins to orient along $\mathbf{\Omega}$ direction, inducing the net magnetic moment (Barnett 1915). The grain magnetic moment due to the Barnett effect is given by:

$$\mu_{\text{Bar}} = \frac{\chi(0)V}{\gamma_e} \mathbf{\Omega}, \quad (6)$$

where $\gamma_e = -g_e \mu_B/\hbar$ is the gyromagnetic ratio of electron spin, $V = 4\pi s a^3/3$ is the grain volume, and $\chi(0)$ is the magnetic susceptibility at zero frequency (Section 2).

According to Purcell (1979), irregular grains have the high rotational energy due to the misalignment of \mathbf{J} and $\mathbf{\Omega}$ with their major axis of inertia moment $\hat{\mathbf{a}}_1$. In the grain's frame of reference, the

misalignment of \mathbf{J} and $\mathbf{\Omega}$ causes the precession of \mathbf{J} and $\mathbf{\Omega}$ around $\hat{\mathbf{a}}_1$ at an angular rate $\omega = \Omega(h-1)\cos\theta$ with θ the angle between \mathbf{J} and $\hat{\mathbf{a}}_1$ (Figure 1, left part). For magnetic grains, the rotating $\mathbf{\Omega}$ induces the rotation of magnetic moment μ_{Bar} around $\hat{\mathbf{a}}_1$ that dissipates the rotational energy into thermal energy. Consequently, grains can stably rotate around $\hat{\mathbf{a}}_1$, i.e., $\mathbf{J} \parallel \hat{\mathbf{a}}_1$, which corresponds to the state that grains have the minimum rotational energy. This internal alignment due to the rotating magnetization is called the Barnett relaxation (Purcell 1979, Roberge et al. 1993), which occurs on a timescale of (see Hoang & Lazarian 2016b):

$$\tau_{\text{BR}} = \frac{\gamma_e^2 I_{\parallel}^3}{VK(\omega)h^2(h-1)J^2}. \quad (7)$$

where $K(\omega) = \chi_2(\omega)/\omega$. The Barnett relaxation timescale for PM grains is numerically given by:

$$\tau_{\text{BR,pm}} \simeq 0.5\hat{\rho}^2 a_{-5}^7 f(\hat{s}) \left[1 + \left(\frac{\omega\tau_{\text{el}}}{2} \right)^2 \right]^2 \left(\frac{J_d}{J} \right)^2 \text{ yr}, \quad (8)$$

and for SPM grains (Hoang et al. 2022):

$$\begin{aligned} \tau_{\text{BR,spm}} &\simeq 1.6 \times 10^{-4} \hat{\rho}^2 f(\hat{s}) a_{-5}^7 \left(\frac{1}{N_{\text{cl},3}\phi_{\text{sp},-2}\hat{\rho}^2} \right) \\ &\times \left(\frac{J_d}{J} \right)^2 \left(\frac{T_{d,1}}{k_{\text{sp}}(\omega)} \right) \text{ yr}, \end{aligned} \quad (9)$$

where $f(\hat{s}) = \hat{s}[(1+\hat{s}^2)/2]^2$ with $\hat{s} = s/0.5$, $J_d = \sqrt{k_B T_d I_{\parallel}/(h-1)}$ is the thermal angular momentum, and $k_{\text{sp}}(\omega)$ is given by:

$$k_{\text{sp}}(\omega) = \exp\left(\frac{N_{\text{cl}}T_{\text{act}}}{T_d}\right) \left[1 + \left(\frac{\omega\tau_{\text{sp}}}{2} \right)^2 \right]^{-2}. \quad (10)$$

Equations (8) and (9) show that large grains experience slower Barnett relaxation. Therefore, in dense environments where the gas damping is significantly shorter (Equation 5), large grains could have inefficient IA due to the slow internal relaxation (Hoang et al. 2022). Following Hoang et al. (2022), we define the lower and upper cutoff for grain sizes with fast internal relaxation determined by the condition $\tau_{\text{BR}} = \tau_{\text{gas}}$ as $a_{\text{min},\text{aJ}}$ and $a_{\text{max},\text{aJ}}$. The range of grains with fast internal relaxation extends with increasing rotational rate and the magnetic susceptibility of grains, i.e., super-Barnett relaxation.

3.3 External alignment with Magnetic field direction

3.3.1 Larmor precession

The interaction between the grain magnetic moment μ_{Bar} and the ambient magnetic field \mathbf{B} produces the magnetic torques that cause the grain angular momentum \mathbf{J} to precess around \mathbf{B} , so-called Larmor precession (Figure 1, right panel). The characteristic timescale of the Larmor precession is given by (see Hoang & Lazarian 2016b):

$$\tau_{\text{Lar}} = \frac{2\pi}{d\phi/dt} = \frac{2\pi I_{\parallel} \Omega}{\mu_{\text{Bar}} B}, \quad (11)$$

where ϕ the precession angle of \mathbf{J} with respect to \mathbf{B} (Figure 1, right panel). The typical Larmor precession timescale for PM grains is:

$$\tau_{\text{Lar,pm}} \simeq 7 \times 10^{-4} \frac{\hat{\rho} T_{d,1} a_{-5}^2}{f_{p,-1} \hat{\rho}^2 B_2} \text{ yr}, \quad (12)$$

and for SPM grains is:

$$\tau_{\text{Lar,spm}} \simeq 8.1 \times 10^{-6} \frac{\hat{\rho} T_{d,1} a_{-5}^2}{N_{\text{cl},3}\phi_{\text{sp},-2}\hat{\rho}^2 B_2} \text{ yr}, \quad (13)$$

where $B_2 = B/100\mu\text{G}$.

Dust grains are considered to have the magnetic alignment when grains rapidly precess around \mathbf{B} , so that \mathbf{J} cannot be randomized by gas collisions, which requires $\tau_{\text{Lar}} < \tau_{\text{gas}}$. Equations (12) and (13) show that large grains are more difficultly aligned with \mathbf{B} due to slower Larmor precession. Following Hoang et al. (2022), we define the maximum size that grain still can be aligned with \mathbf{B} is $a_{\text{max},\text{JB}}^{\text{Lar}}$. More large grains can be aligned with \mathbf{B} , i.e., higher $a_{\text{max},\text{JB}}^{\text{Lar}}$, if they have higher magnetic susceptibility by iron inclusions (Equation 13).

3.3.2 Magnetic relaxation

A paramagnetic grain rotating with the angular velocity $\mathbf{\Omega}$ misaligned with the ambient field \mathbf{B} experiences the dissipation of the grain rotational energy due to the lag of the grain magnetization with respect to the ambient field, which eventually brings $\mathbf{\Omega}$ (also \mathbf{J}) to be aligned with \mathbf{B} that corresponds to the minimum rotational energy (Davis & Greenstein 1951, so-called the Davis-Greenstein mechanism). The timescale for the magnetic relaxation is given by (e.g., Hoang & Lazarian 2016b):

$$\tau_{\text{mag}} = \frac{I_{\parallel}}{VK(\Omega)B^2}. \quad (14)$$

where $K(\Omega) = \chi_2(\Omega)/\Omega$. The timescale of paramagnetic relaxation is:

$$\tau_{\text{mag,pm}} \simeq 3440 \frac{\hat{\rho} a_{-5}^2 T_{d,1}}{\hat{\rho} B_2^2} \left(1 + \left(\frac{\Omega\tau_{\text{el}}}{2} \right)^2 \right)^2 \text{ yr}, \quad (15)$$

and the timescale of superparamagnetic relaxation (for SPM) is (Hoang et al. 2022):

$$\tau_{\text{mag,spm}} \simeq 1.5 \frac{\hat{\rho} a_{-5}^2}{N_{\text{cl},3}\phi_{\text{sp},-2}\hat{\rho}^2 B_2^2} \frac{T_{d,1}}{k_{\text{sp}}(\Omega)} \text{ yr}, \quad (16)$$

where $k_{\text{sp}}(\Omega)$ is given by Equation (10).

To describe the strength of magnetic relaxation on aligning dust grains, we use the magnetic relaxation parameter:

$$\begin{aligned} \delta_m &= \frac{\tau_{\text{gas}}}{\tau_{\text{mag,spm}}} \\ &\approx 0.056 a_{-5}^{-1} \frac{N_{\text{cl},3}\phi_{\text{sp},-2}\hat{\rho}^2 B_2^2}{\hat{\rho} n_{H,8} T_{\text{gas},1}^{1/2}} \frac{k_{\text{sp}}(\Omega)}{T_{d,1}}. \end{aligned} \quad (17)$$

Grains can have some degree of alignment by magnetic relaxation when the magnetic relaxation happens faster than gas randomization, which is given by $\delta_m > 1$. Following Hoang et al. (2022), we denote the maximum size at which the magnetic relaxation is still effective as $a_{\text{max},\text{JB}}^{\text{DG}}$. SPM grains experience stronger magnetic relaxation due to larger magnetic susceptibility (Equation 16). However, Hoang & Lazarian (2016b); Hoang & Lazarian (2016a) showed that the grain alignment by magnetic relaxation is still inefficient even for $\delta_m \gg 1$ in the absence of grain suprathermal rotation due to internal thermal fluctuations.

3.4 Radiative Torque Alignment (RAT) Paradigm

The RAdiative Torque (RAT) mechanism is demonstrated to efficiently drive grain alignment, even for paramagnetic grains (Lazarian

& Hoang 2007; Hoang & Lazarian 2008). Moreover, the joint effect between RATs and superparamagnetic relaxation can lead grains to achieve perfect alignment with magnetic fields, which is known as the MRAT mechanism (Hoang & Lazarian 2008; Hoang & Lazarian 2016b). Here, we describe the main properties of the RAT and MRAT alignment mechanisms for reference (see Hoang et al. 2022 for more details).

3.4.1 Suprathermal rotation by RATs

Dolginov & Mitrofanov (1976) proposed that irregular grains receive RATs due to differential scattering and absorption of photons with the left and right-hand angular momentum. Let $a_{\text{eff}} = as^{1/3}$ be an effective radius of a spherical grain that has the same volume as the irregular grain (Draine & Weingartner 1996; Lazarian & Hoang 2007), the maximum angular speed that the grain achieve by RATs in the constant radiation field is given by (Hoang & Lazarian 2014):

$$\Omega_{\text{RAT}} = \frac{\Gamma_{\text{RAT}} \cos \psi \tau_{\text{damp}}}{I_{\parallel}}, \quad (18)$$

where Γ_{RAT} is the total radiative torques that the grain receives, which is:

$$\Gamma_{\text{RAT}} = \int_{\lambda_{\min}}^{\lambda_{\max}} \pi a_{\text{eff}}^2 \left(\frac{\lambda}{2\pi} \right) \gamma_{\lambda} u_{\lambda} Q_{\Gamma} d\lambda, \quad (19)$$

where u_{λ} is the radiation energy density at wavelength λ , λ_{\min} and λ_{\max} are the lower and upper boundary of the working region of RAT mechanism (i.e., FUV-FIR), and γ_{λ} is the anisotropic degree at wavelength λ , which is defined as (Bethell et al. 2007):

$$\gamma_{\lambda} = \frac{1}{4\pi J_{\lambda}} \left| \int I_{\lambda} \mathbf{k} d\Omega \right|, \quad (20)$$

where I_{λ} and J_{λ} are the specific intensity and the mean intensity at wavelength λ , and \mathbf{k} is the propagation direction of photon. In Equation (19), Q_{Γ} is the RAT efficiency, which is a constant for large grains of size $a_{\text{eff}} \geq \lambda/1.8$ and decreases with decreasing grain sizes for $a_{\text{eff}} < \lambda/1.8$ (see Lazarian & Hoang 2007, Hoang & Lazarian 2008).

The second term ψ in Equation (18) is the angle between \mathbf{B} and the radiation field direction \mathbf{k} , and the third term $\tau_{\text{damp}} = \tau_{\text{gas}}/(1 + F_{\text{IR}})$ is the total grain damping timescale caused by gas collisions (the term τ_{gas}) and re-emit IR radiation (the dimensionless coefficient F_{IR} describes the rotational damping due to IR emission) (see Draine & Lazarian 1998 for a detail).

3.4.2 Minimum grain size for the RAT alignment

Hoang & Lazarian (2008) showed that grains can efficiently align with \mathbf{J} parallel to \mathbf{B} against gas randomization when they are spun up to suprathermal rotation with $\Omega_{\text{RAT}} \geq 3\Omega_{\text{th}} = 3\sqrt{k_{\text{B}}T_{\text{gas}}/I_{\parallel}}$. The grain size at which $\Omega_{\text{RAT}} = 3\Omega_{\text{th}}$ is called alignment size, a_{align} , at which all larger grains will be efficiently aligned with \mathbf{B} (e.g., B-RAT mechanism, Hoang et al. 2022), provided that their Larmor precession is faster than the gas randomization, i.e., $a < a_{\text{max,JB}}^{\text{Lar}}$ (Section 3.3.1).

3.4.3 A model in the RAT alignment: low- J and high- J attractors

RATs not only can spin up grains to suprathermal rotation but also can align \mathbf{J} with \mathbf{B} by the alignment torque component (Lazarian & Hoang 2007, Hoang & Lazarian 2008, Hoang & Lazarian 2016b).

Theoretical and numerical studies of RATs in Hoang & Lazarian (2008) show that, for aligned grains of $a_{\text{align}} < a < a_{\text{max,JB}}^{\text{Lar}}$, a fraction of grains can stably align with \mathbf{B} at their maximum angular velocity, Ω_{RAT} (so-called high- J attractors). The rest of grains are spun down by RATs and align with \mathbf{B} at thermal rotation Ω_{th} (so-called low- J attractors). The fraction of grains aligning with \mathbf{B} at high- J attractors is parameterized by the parameter $f_{\text{high-J}}$. The exact value of $f_{\text{high-J}}$ depends complexly on the physical properties of grains and the orientation of grains with the ambient radiation and magnetic fields (Hoang & Lazarian 2008; Hoang & Lazarian 2016b; Lazarian & Hoang 2021). For grains at low- J attractors, the gas randomization can gradually transport grains from low- J to high- J attractors. The value of $f_{\text{high-J}}$ for irregular compact grains can vary within 0.25 – 0.7 (Herranen et al. 2021).

Hoang & Lazarian (2016b) found that the fraction $f_{\text{high-J}}$ is increased for SPM grains due to enhanced magnetic relaxation via the MRAT mechanism. Their numerical calculations of the MRAT alignment showed that SPM grains can have perfect alignment of $f_{\text{high-J}} = 1$ for $\delta_{\text{m}} \geq 10$ (Equation 17).

4 MODELLING OF GRAIN ALIGNMENT AND DUST POLARIZATION WITH POLARIS

In this section, we will first describe the fundamental components of POLARIS in Section 4.1, then describe how we incorporate the new physical effects induced by iron inclusions on grain alignment in Section 4.2.

4.1 An overview of the POLARIS code

There are two main simulations inside POLARIS: the three-dimensional (3D) radiative transfer simulation using the Monte-Carlo technique that provides the information of radiation field required for calculating dust and gas temperature and radiative torques for grain alignment by RATs. The results from the Monte-Carlo Radiative Transfer (MCRT) simulation are used to solve the polarized radiative transfer of Stokes parameters by the ray-tracing method to obtain the polarization degree p and polarization angle (PA). The detailed description of the working flow in POLARIS is given in detail in Reissl et al. (2016) and Reissl et al. (2020). Here, we just briefly describe the main features of POLARIS.

4.1.1 Monte Carlo Radiative Transfer

For the MCRT simulation, given the 3D gas density distribution of an astronomical object and the dust model, POLARIS simulates the interactions of photons emitted from the radiation source with surrounding dust grains by using the MCMC technique introduced by Lucy (1999), which allows us to immediately correct dust temperatures to simulate the spontaneous thermal emission of dust grains. In detail, when each absorption event between grain of size a and photon happens, POLARIS assumes the temporary thermal equilibrium between the current radiation absorption and dust emission to immediately correct the grain temperature $T_{\text{d}}(a)$ (see Section 4.1.2). One new photon with a wavelength sampled from the Planck function of grains with updated $T_{\text{d}}(a)$ is sent to the grid cell immediately to guarantee the energy conservation between the stellar absorption and thermal dust emission. For the radiation field, the mean intensity at wavelength J_{λ} inside each cell is calculated by summing energy deposited from all photons entering, being scattering or absorbing

Table 1. Notations and meanings

Notation	Meaning	Notation	Meaning
f_p	Iron fraction of PM grains	a	Major axis of oblate spheroidal grain
τ_{el}	Electron spin relaxation timescale	s	Axial ratio
$\chi_{pm}(0)$	Magnetic susceptibility at $\omega = 0$ of PM	a_{eff}	Effective radius
$\chi_{pm}(\omega)$	Magnetic susceptibility at frequency ω of PM	a_{align}	Minimum grain alignment size
N_{cl}	Number of iron atoms/cluster	$a_{max,JB}^{Lar}$	Maximum grain alignment size
ϕ_{sp}	Volume filling factor of iron clusters	f_{high-J}	Fraction of aligned grains at high- J
τ_{sp}	Thermally activated remagnetization timescale	$a_{min,J}^{low-J}$	Minimum size with fast internal relaxation at low- J
$\chi_{spm}(0)$	Magnetic susceptibility at $\omega = 0$ of SPM	$a_{max,J}^{low-J}$	Maximum size with fast internal relaxation at low- J
$\chi_{spm}(\omega)$	Magnetic susceptibility at frequency ω of SPM	$a_{min,J}^{high-J}$	Minimum size with fast internal relaxation at high- J
μ_{Bar}	Magnetic moment gained by Barnett effect	$a_{max,J}^{high-J}$	Maximum size with fast internal relaxation at high- J
τ_{Lar}	Larmor precession timescale	$a_{max,JB}^{DG,0.5}$	Maximum grain size has $f_{high-J} = 0.5$
τ_{BR}	Barnett relaxation timescale	$a_{max,JB}^{DG,1}$	Maximum grain size has $f_{high-J} = 1$
τ_{mag}	Magnetic relaxation timescale	Γ_{RAT}	Radiative torque
δ_m	Magnetic relaxation parameter	γ_{rad}	Mean anisotropic degree
τ_{gas}	Gas damping timescale	Q_{Γ}	RAT efficiency
θ	Angle between $\hat{\mathbf{a}}_1$ and \mathbf{J}	Ω_{RAT}	Maximum angular velocity gained by RATs
β	Angle between \mathbf{J} and \mathbf{B}	Ω_T	Thermal angular velocity
ψ	Angle between \mathbf{k} and \mathbf{B}	R	Rayleigh reduction factor
$Q_{X,low-J}$	Internal alignment (IA) efficiency at low- J	$Q_{X,high-J}$	IA efficiency at high- J
$Q_{I,low-J}$	External alignment (EA) efficiency at low- J	$Q_{I,high-J}$	EA efficiency at high- J

by dust grains inside cell, and leaving the cell. The direction of photons inside the cell is saved to calculate the anisotropic degree at wavelengths λ , γ_{λ} , as defined by Equation (20).

4.1.2 Dust and gas temperature

Knowing the mean intensity inside each cell after the MCRT simulation, the temperature of grain of size a , $T_d(a)$, is calculated following the thermal equilibrium between the radiation absorption and emission, which is (Lucy 1999, Reissl et al. 2016):

$$\int C_{abs,\lambda} J_{\lambda} d\lambda = \int C_{abs,\lambda} B_{\lambda}(T_d(a)) d\lambda, \quad (21)$$

where C_{abs} is the absorption cross section of grain size a with wavelength λ (see Appendix A). The average dust temperature in the cell is taken by integrating over the grain size distribution dn/da , i.e., $T_d = \int_{a_{min}}^{a_{max}} T_d(a) (dn/da) da$. The gas temperature is considered to correlate with the dust temperature via a dimensionless coefficient α , giving $T_{gas} = \alpha T_d$. For dense environments as protostellar cores, gas is mainly heated by colliding with grains, inducing the coupling between gas and dust temperature. For our calculations, we consider the thermal equilibrium between gas and grains with $T_{gas} = T_d$ (or $\alpha = 1$).

4.1.3 Modelling Grain Alignment by RATs

(a) Minimum grain size of RAT alignment, a_{align}

Figure 2 shows the flow to determine the grain alignment degree with \mathbf{B} in POLARIS. From the top of the figure, given the radiation field and gas temperature from the MCRT simulation and the input dust model, POLARIS can calculate the radiative torques Γ_{RAT} and the maximum angular speed gained by RATs, Ω_{RAT} , for all grain sizes as described in Section 3.4.1. The minimum alignment size, a_{align} , is calculated by the alignment criteria described in Section 3.4.2.

(b) Maximum size of grain alignment with \mathbf{B} by Larmor precession, $a_{max,JB}^{Lar}$

Another criterion for stable grain alignment with \mathbf{B} (i.e., magnetic alignment) is that the Larmor precession must be faster than the grain randomization by gas collisions, which is described by the maximum alignment size $a_{max,JB}^{Lar}$ (Section 3.3.1). In the current version of POLARIS, PM grains are considered to have the magnetic alignment if $\tau_{Lar} \leq \tau_{gas}$ (Hoang & Lazarian 2009; Hoang et al. 2022), giving ¹:

$$a_{max,JB}^{Lar} \approx 7.589 \frac{s^2 B_2}{n_{H,8} T_{d,1} \sqrt{T_{gas,1}}} \mu m. \quad (22)$$

(c) Degree of grain alignment: Rayleigh reduction factor, R
Greenberg (1968) introduced the Rayleigh reduction factor R which describes the degree of internal alignment between \mathbf{J} and $\hat{\mathbf{a}}_1$ and external alignment between \mathbf{J} and \mathbf{B} , which is defined as $R = \langle Q_X Q_I \rangle$ where the bracket denotes the averaging over an ensembles of grains. The exact calculations of R for dust grains using the RAT theory are rather challenging and require numerical simulations (Hoang & Lazarian 2008; Hoang & Lazarian 2016b). Therefore, POLARIS uses the parametric model of the RAT alignment proposed in Hoang & Lazarian (2014). This parametric model is based on the fact that, in general, RATs can align a fraction f_{high-J} of grains at high- J attractors, and the remaining fraction $(1 - f_{high-J})$ of grains are aligned

¹ There is a misprint in Equation (31) in Reissl et al. (2016) where the prefactor of 4.1×10^{-9} is written instead of the correct one of 4.1×10^{-19} , in which $a_{max,JB}^{Lar}$ is given in m, n_H is given in m^{-3} , and B is given in T. In POLARIS, they adopt the constant of 4.1×10^{-21} , two orders of magnitude smaller than the exact values derived for PM grains, which overestimate the value of $a_{max,JB}^{Lar}$ by two orders of magnitude. Although this misprint does not cause any problem with grain alignment in the ISM and MCs with low density, it will overestimate the effect of magnetic alignment for large PM grains in dense cores and protostellar environments of very high density.

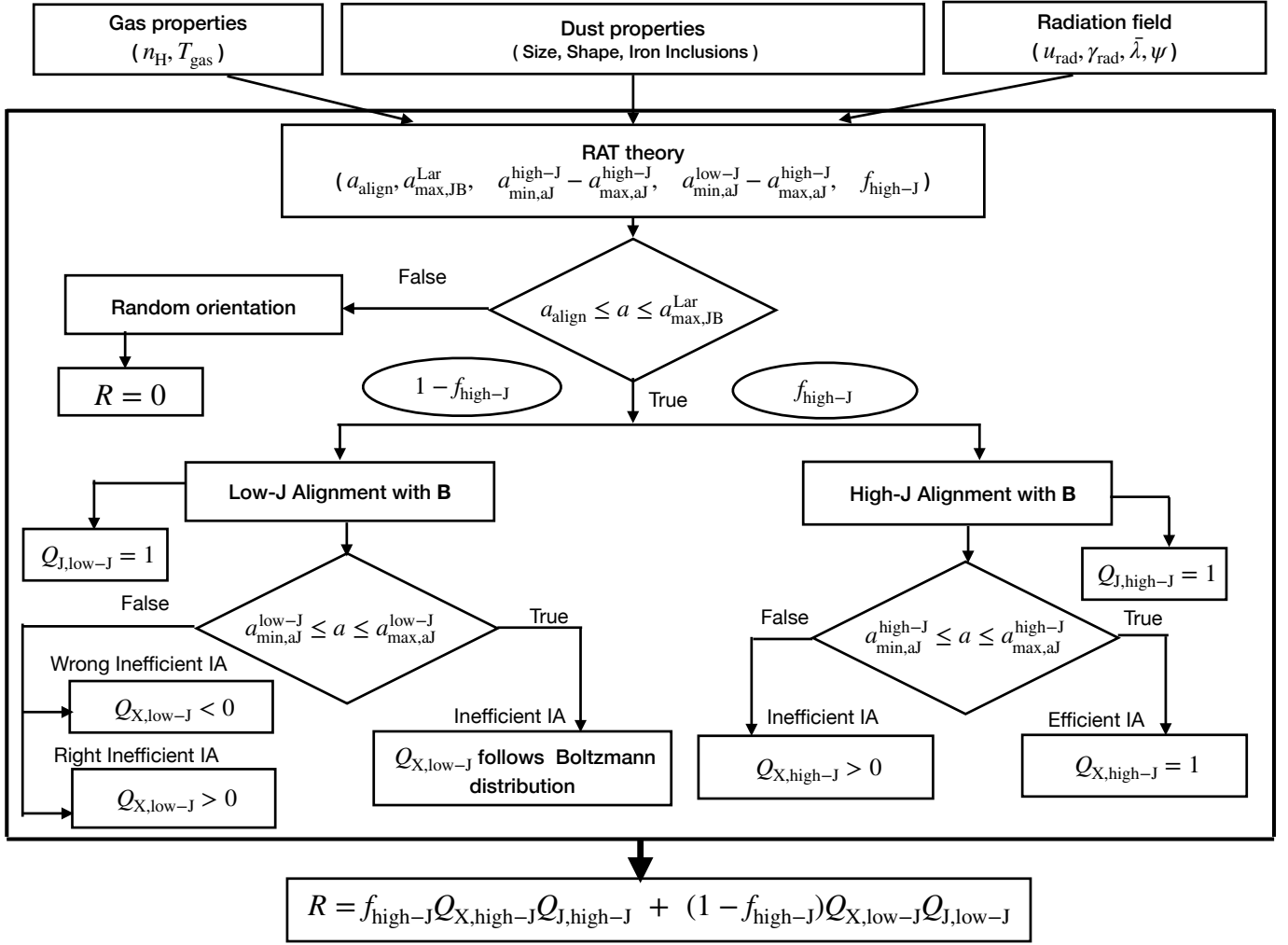


Figure 2. Schematic to determine the alignment degree of grains with magnetic fields in POLARIS. Given the dust model, gas properties, and radiation field information (u_λ , γ_λ , ψ), POLARIS can determine the typical grain size for grain alignment by RATs ($a_{\text{align}} - a_{\text{max,JB}}^{\text{Lar}}$), the internal alignment degree Q_X of grains at low and high- J attractors, and the fraction of grains aligned with **B** at high- J attractors $f_{\text{high-J}}$. Finally, one can calculate the Rayleigh reduction factor R that describes the total internal and external alignment degree of grains with **B**.

at low- J attractors. Therefore, the Rayleigh reduction factor for the RAT alignment can be written as (the bottom of Figure 2):

$$R = f_{\text{high-J}} Q_{X,\text{high-J}} Q_{J,\text{high-J}} + (1 - f_{\text{high-J}}) Q_{X,\text{low-J}} Q_{J,\text{low-J}}, \quad (23)$$

where $Q_{X,\text{high-J}}$, $Q_{J,\text{high-J}}$ are the degrees of internal and external alignment for grains at high- J attractors, and $Q_{X,\text{low-J}}$, $Q_{J,\text{low-J}}$ are for grains at low- J attractors.

The degree of internal alignment is defined as $Q_X = \langle G(\cos^2 \theta) \rangle$ with $G(\cos^2 \theta) = 1/2(3 \cos^2 \theta - 1)$ and θ the angle between **J** and $\hat{\mathbf{a}}_1$ ($\theta \in [0 - \pi]$, Figure 1). For grains at high- J attractors, we adopt $Q_{X,\text{high-J}} = 1$ because grains can have perfect IA due to their suprathermal rotation. In contrast, grains at low- J attractors have inefficient IA due to the thermal fluctuations inside grains (Purcell 1979). POLARIS assumes that internal relaxation process is always faster than gas randomization, i.e., fast internal relaxation, i.e., $\tau_{\text{Bar}} < \tau_{\text{gas}}$ (Section 3.2), such that there is an efficient energy exchange between the grain rotational energy and the grain vibrational system. The angle θ between **J** and $\hat{\mathbf{a}}_1$ for grains rotating

thermally then can be described by the local thermal equilibrium (TE) Boltzmann distribution (Lazarian & Roberge 1997):

$$f_{\text{TE}}(\theta) = Z \exp \left(-\frac{J_{\text{th}}^2}{2I_{\parallel} k_B T_d} [1 + (h-1) \sin^2(\theta)] \right), \quad (24)$$

where Z is the normalization factor such that $\int_0^\pi f_{\text{LE}} \sin \theta d\theta = 1$, and J_{th} is the thermal angular momentum.

The degree of internal alignment by fast internal relaxation at low- J attractors is calculated as:

$$Q_{X,\text{low-J}} = \int_0^\pi G(\cos^2 \theta) f_{\text{LE}}(\theta) \sin \theta d\theta. \quad (25)$$

The external alignment degree is described by $Q_J = \langle G(\cos^2 \beta) \rangle$ with β the angle between **J** and **B** (Figure 1). POLARIS considers that grains at both low and high- J attractors have perfect external alignment by RATs, giving $Q_{J,\text{low-J}} = Q_{J,\text{high-J}} = 1$. Grains are assumed to be randomly oriented with $R = 0$ for $a < a_{\text{align}}$ and $a > a_{\text{max,JB}}^{\text{Lar}}$.

4.1.4 Polarized radiative transfer of Stokes vector and the Dust polarization information

After the Monte-Carlo calculation of the radiation field for RAT alignment, POLARIS calculates the polarized radiative transfer of the Stokes vector $\vec{S} = [I \ Q \ U \ V]^T$ with Stokes I representing the total intensity, Stokes Q and U the linear polarization, and Stokes V It uses the Runge-Kutta method to solve the full polarized radiative transfer equation of \vec{S} along the propagation of photons, given the gas density, grain temperature, and the alignment degree of grains with local magnetic fields, i.e., the Rayleigh reduction factor R , in the grid space calculated from the first simulation (Sections 4.1.2 and 4.1.3). The detailed description of the polarized radiative transfer of the Stokes vector is given in Appendix A.

The degree of linear polarization p is given by:

$$p = 100 \frac{\sqrt{Q^2 + U^2}}{I} (\%), \quad (26)$$

and the polarization angle (PA) is:

$$PA = \frac{1}{2} \arctan \left(\frac{Q}{U} \right). \quad (27)$$

4.2 Extending POLARIS for dust grains with Iron Inclusions

As discussed above, the current version of POLARIS is based on the classical RAT theory for PM grains and assumed aligned dust grains always have fast internal relaxation (Hoang & Lazarian 2014), which is valid only for sub-micron grains in the diffuse ISM and MCs. In very dense environments such as protostellar cores and disks, both the gas density and grain sizes increase many orders of magnitudes, which requires a detailed treatment of internal and external alignment to accurately model the synthetic dust polarization toward this regions (Hoang 2022; Hoang et al. 2022). Here, we describe our improvements of POLARIS by taking into account new effects which are important for large grains in protostellar environments, including grains with iron inclusions, effects of iron inclusions on Barnett relaxation and internal alignment, Larmor precession and enhanced external alignment by MRAT alignment.

4.2.1 Treatment of Enhanced Magnetic Susceptibility by Iron Inclusions

Following Section 2, we describe the magnetic susceptibility of PM grains by using the parameter f_p (the fraction of iron atoms diffusely distributed inside grains), and SPM grains by using parameter ϕ_{sp} (the volume filling factor of iron clusters) and N_{cl} (the number of iron atoms in a single cluster). For given f_p , ϕ_{sp} , N_{cl} , and the grain temperature calculated in Section 4.1.2, we can calculate $\chi_{pm}(0)$ for PM grains using Equation (1) and $\chi_{spm}(0)$ for SPM grains using Equation (3). Note that, for SPM grains, even with a fixed ϕ_{sp} (i.e., constant volume of iron clusters locked in dust), the SPM susceptibility can be increased by increasing N_{cl} .

4.2.2 Improved treatment of the Larmor precession and Magnetic alignment

The first effect that we revisit is the disalignment of grains by gas collisions when the Larmor precession is slower than gas randomization (Section 3.3.1). As shown in Section 4.1.3, the current version of POLARIS adopts smaller prefactor (i.e., 4.1×10^{-21}) for the maximum

alignment size $a_{\max,JB}^{\text{Lar}}$ of PM grains, that certainly overestimates the range of grain alignment in dense environments. In addition, dust grains are currently considered to be efficiently aligned with \mathbf{B} if they can complete one Larmor precession before being randomized by gas collisions, or $\tau_{\text{Lar}} \leq \tau_{\text{gas}}$. This condition may be insufficient for grains to be strongly coupled with \mathbf{B} in high gas-grains collision environments (Yang 2021). Here, we assume that grains can only be coupled to \mathbf{B} when the Larmor precession is at least ten times faster than the gas randomization, or in terms of timescales, $\tau_{\text{Lar}} \leq \tau_{\text{gas}}/10$ (e.g., Yang 2021).

To calculate $a_{\max,JB}^{\text{Lar}}$ for PM and SPM grains, we plug $\chi(0)$ calculated in Section 4.2.1 in Equation (6) to obtain the grain magnetic moment μ_{Bar} . Then, we use the value of μ_{Bar} for Equation (11) to obtain τ_{Lar} . By comparing τ_{Lar} to $\tau_{\text{gas}}/10$ with τ_{gas} given by Equation (5) over the grain size distribution, one can determine the value of $a_{\max,JB}^{\text{Lar}}$.

4.2.3 Modeling the dependence of Internal Alignment on Grain Magnetic properties

The second effect that we take into account is the dependence of internal alignment on the grain magnetic properties. As discussed in the previous section, the current version of POLARIS assumes that all grains have *right* IA with $\hat{\mathbf{a}}_1$ parallel to \mathbf{B} due to fast internal relaxation. However, as shown in Equation (7), the rate of internal relaxation by Barnett effect depends sensitively on the grain size, the magnetic susceptibility (χ), and the grain angular momentum (J), which can be faster or slower than the gas randomization. Therefore, it is critically important to determine the range of grain sizes which has fast internal relaxation (see Hoang 2022; Hoang et al. 2022). Here, we follow the approach proposed in Hoang et al. (2022) by considering separately grains aligned at high- J and low- J attractors.

(a) Grains at high- J attractors

Grains aligned with \mathbf{B} at high- J attractors have suprathermal rotation with the grain angular velocity of $\Omega = \Omega_{\text{RAT}}$. The precession rate of \mathbf{J} around $\hat{\mathbf{a}}_1$ is given by $\omega = \Omega_{\text{RAT}}(h - 1) \cos \theta$. We take $\theta = 45^\circ$ be the average angle between \mathbf{J} and $\hat{\mathbf{a}}_1$ for numerical calculations (Purcell 1979, Hoang et al. 2022). For PM grains, we calculate $\chi_{2,pm}(\omega)$ by putting $\chi(0)$ (**which is calculated** in Section 4.2.1) and Ω_{RAT} (**which is calculated in** Section 4.1.3) to Equation (2), then put $\chi_{2,pm}(\omega)$ and $J = I_{\parallel} \Omega_{\text{RAT}}$ to Equation (7) to obtain the Barnett relaxation timescale τ_{BR} . Then, by comparing τ_{BR} with τ_{gas} over the grain size distribution, one can determine the minimum size ($a_{\min,aJ}^{\text{high-J}}$) and maximum size ($a_{\max,aJ}^{\text{high-J}}$) that PM grains have fast internal relaxation at high- J attractors. We follow the same method for SPM grains, but $\chi_{2,spm}(\omega)$ is calculated by putting $\chi_{spm}(0)$ (**which is calculated in** Section 4.2.1) into Equation (4).

(b) Grains at low- J attractors

Grains aligned with \mathbf{B} at low- J attractors rotate with thermal angular velocity of $\Omega = \Omega_d = J_d/I_{\parallel}$ with J_d the thermal angular momentum (Section 3.2). The precession rate of \mathbf{J} around $\hat{\mathbf{a}}_1$ is $\omega = \Omega_d(h - 1) \cos(\theta)$. Following the same flow as grains at high- J attractors, we first calculate $\chi_2(\omega)$ and put it into Equation (7) to get τ_{BR} . Then following the condition of $\tau_{\text{BR}} \leq \tau_{\text{gas}}$, we can determine the range of grains with fast internal relaxation at low- J attractors [$a_{\min,aJ}^{\text{low-J}}$ – $a_{\max,aJ}^{\text{low-J}}$].

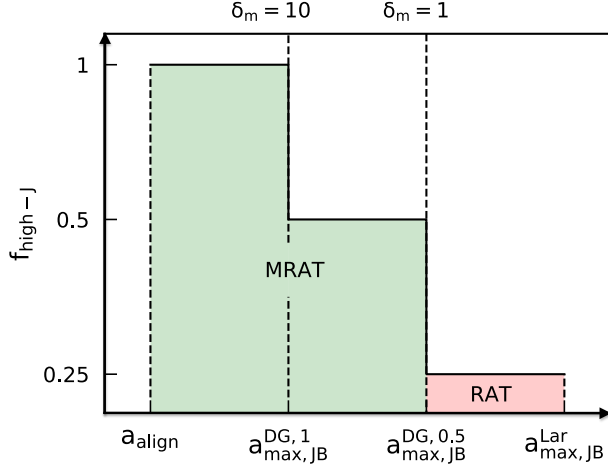


Figure 3. Illustration of the variation of $f_{\text{high-J}}$ with alignment grain size within $[a_{\text{align}} - a_{\text{max,JB}}^{\text{Lar}}]$ by MRAT alignment, see Equation (28). Vertical dashed lines mark the location where $\delta_m = 1, 10$ and the corresponding critical sizes, $a_{\text{max,JB}}^{\text{DG},0.5}$, $a_{\text{max,JB}}^{\text{DG},1}$, respectively.

4.2.4 Modeling the increase of $f_{\text{high-J}}$ with superparamagnetic relaxation

The last effect that we consider is the increase in the RAT alignment by magnetic relaxation, described by the MRAT model (Hoang & Lazarian 2016b). The current version of POLARIS treats $f_{\text{high-J}}$ as the free parameter (Section 4.1.3), which does not change with the grain size and grain magnetic properties. However, the value of $f_{\text{high-J}}$ is found to increase with the magnetic relaxation, which is described by the magnetic parameter δ_m (Hoang & Lazarian 2016b). To model the increase of $f_{\text{high-J}}$ with δ_m as numerically calculated in Hoang & Lazarian (2016b), we introduce the following parametric model:

$$f_{\text{high-J}}(\delta_m) = \begin{cases} 0.25 & \text{for } \delta_m < 1 \\ 0.5 & \text{for } 1 \leq \delta_m \leq 10 \\ 1 & \text{for } \delta_m > 10 \end{cases}, \quad (28)$$

where δ_m depends on the grain size, magnetic susceptibility, and gas density. Above, we have adopted a typical value of $f_{\text{high-J}} = 0.25$ for the case $\delta_m < 1$ at which grains are mainly aligned with **B** by RATs.² For grains with significantly enhanced magnetic relaxation, i.e., $\delta_m > 10$, we take $f_{\text{high-J}} = 1$ due to the joint effect of RATs and

Table 2. Grain alignment physics in the current and updated version of POLARIS

Effect	Current POLARIS	Update POLARIS
Magnetic properties	Paramagnetic	Grains with Iron Inclusions
Internal Alignment		
Internal relaxation rate	Fast	Fast and Slow
External Alignment		
Fast Larmor precession	$\tau_{\text{Lar}} \leq \tau_{\text{gas}}$	$\tau_{\text{Lar}} \leq \tau_{\text{gas}}/10$
Alignment mechanism	RAT, fixed $f_{\text{high-J}}$	MRAT, $f_{\text{high-J}}$ depends on magnetic susceptibility.

superparamagnetic relaxation (Hoang & Lazarian 2016b; Lazarian & Hoang 2021). And we adopt the intermediate value of $f_{\text{high-J}} = 0.5$ for grains with $1 \leq \delta_m \leq 10$.

For a given local condition, $f_{\text{high-J}}$ is a function of the grain size and magnetic susceptibility because δ_m depends on these parameters (Equation 17). To obtain the function $f_{\text{high-J}}(a)$ for SPM grains, we first calculate $\chi_{2,\text{spm}}(\Omega_{\text{RAT}})$ by using Equation (4), then put this parameter to Equation (14) to obtain superparamagnetic relaxation timescale. Then, by calculating δ_m (Equation 17) over the grain size distribution and following Equation (28), we can determine the maximum size that grains have $f_{\text{high-J}} = 0.5$ (denoted by $a_{\text{max,JB}}^{\text{DG},0.5}$) and $f_{\text{high-J}} = 1$ (denoted by $a_{\text{max,JB}}^{\text{DG},1}$).

Figure 3 presents the schematic illustration of the variation of $f_{\text{high-J}}$ with grain alignment size within $[a_{\text{align}} - a_{\text{max,JB}}^{\text{Lar}}]$ and critical sizes for grain alignment by the MRAT mechanism. Small SPM grains of size $a < a_{\text{max,JB}}^{\text{DG},1}$ can have $f_{\text{high-J}} = 1$ because of their faster magnetic relaxation (Equation 14). Larger grains of size $a_{\text{max,JB}}^{\text{DG},1} < a < a_{\text{max,JB}}^{\text{DG},0.5}$ have smaller $f_{\text{high-J}} = 0.5$ because of their slower magnetic dissipation. Large grains of $a > a_{\text{max,JB}}^{\text{DG},0.5}$ have $f_{\text{high-J}} = 0.25$ due to the negligible contribution of magnetic relaxation to RAT alignment.

4.2.5 Improved Rayleigh reduction factor

Due to the dependence of the internal and external alignment of grains on iron inclusions and local conditions described in the previous section, the Rayleigh reduction factor R also changes. The illustration of our new flow for calculating R is shown in the middle and bottom parts of Figure 2 as following:

For grains aligning with **B** at high- J attractors (right panel), grains of size $a_{\text{min,aJ}}^{\text{high-J}} < a < a_{\text{max,aJ}}^{\text{high-J}}$ will have fast internal relaxation and then efficient IA due to suprathermal rotation of grains, giving $Q_{\text{X,high-J}} = 1$, as adopted in the current version of POLARIS (Section 4.1.3). Grains beyond this range have the slow internal relaxation, which induces the inefficient IA. The study of RAT alignment for grains without internal relaxation by Hoang & Lazarian (2016b) showed that RATs could drive grains to have right IA ($\hat{\mathbf{a}}_1 \parallel \mathbf{J}$) if they align with **B** at high- J attractors, but may have right or wrong IA ($\hat{\mathbf{a}}_1 \perp \mathbf{J}$) for grains at low- J attractors. For the latter case, the alignment degree of grains with wrong IA is described by the negative value of $Q_{\text{X}} < 0$. The detailed angle distribution $f(\theta)$ for grains with slow internal relaxation is still missing, thus we assume Q_{X} to be a free parameter for grains beyond the range $a_{\text{min,aJ}} - a_{\text{max,aJ}}$. For the modelling of grains with inefficient IA at high- J attractors, we adopt $Q_{\text{X,high-J}} = 0.15$ as a typical value in this paper.

² The value of $f_{\text{high-J}}$ driven by RATs can vary between $\sim 0.2 - 0.7$, depending on grain shapes and radiation fields (Herranen et al. 2021).

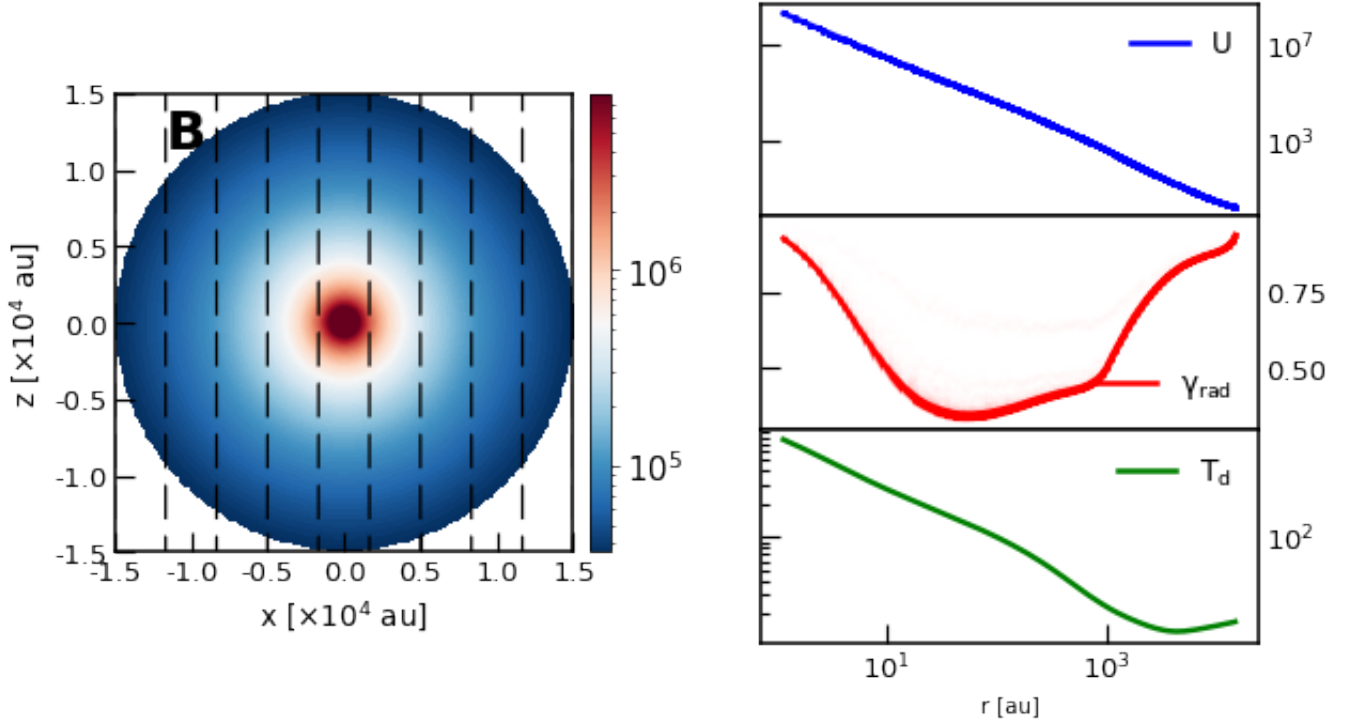


Figure 4. Left panel: Model of a spherical protostellar core of size 15000 au with the embedded low-mass protostar in the center. The gas density is uniform with $n_{\text{H}} = 7 \times 10^6 \text{ cm}^{-3}$ in the central region of size 1000 au (red circle) and decreases with $n_{\text{H}} \sim r^{-2}$ in the envelope. The white dashed line shows the magnetic field direction, with the constant magnetic field strength of $B = 134 \mu\text{G}$. Right panel: Variation of the radiation field strength U , the average anisotropic degree γ_{rad} , and the dust temperature T_{d} along r direction.

For grains aligned with \mathbf{B} at low- J attractors (left part), grains within $a_{\text{min},\text{J}}^{\text{low-J}} < a < a_{\text{max},\text{J}}^{\text{low-J}}$ have fast internal relaxation but inefficient IA due to thermal fluctuations inside grains. The angle θ follows the Boltzmann distribution given by Equation (24) and the internal alignment degree $Q_{\text{X},\text{low-J}}$ is given by Equation (25). Grains beyond this range have slow internal relaxation and inefficient IA with right or wrong IA. We adopt $Q_{\text{X},\text{low-J}} = -0.1$ for the case of wrong IA and $Q_{\text{X},\text{low-J}} = 0.05$ for grains with right IA to study the effect of grains with slow internal relaxation on synthetic polarizations of protostellar cores. The choice of low $Q_{\text{X}} \sim 0$ for grains with slow internal relaxation is to present the weak internal alignment between $\hat{\mathbf{a}}_1$ and \mathbf{J} (grains with random orientation has $Q_{\text{X}} = 0$).

For the alignment between \mathbf{J} and \mathbf{B} , we use the same assumption of the perfect external alignment as in the current version of POLARIS. Then, by plugging the terms Q_{X} and Q_{J} for grains at high and low- J attractors into Equation (23), one can calculate the alignment degree of grains with \mathbf{B} (i.e., R), and use it to perform synthetic polarizations as described in Section 4.1.4. The summary of new effects that we incorporate into POLARIS is given in Table 2.

5 MODELLING RESULTS FOR A PROTOSTELLAR CORE

5.1 Physical model of a protostellar core

We consider a spherical protostellar core and describe it by the spherical grid with $N_r \times N_\theta \times N_\varphi = 250 \times 101 \times 1$ where N_r, N_θ , and

N_φ are the number of cells along the radial, polar, and azimuthal direction.³

The gas density follows the Bonor-Ebert distribution:

$$n_{\text{H}} = n_{\text{H},0} \begin{cases} 1 & \text{for } r \leq R_{\text{center}} \\ (r/r_{\text{center}})^{-2} & \text{for } R_{\text{center}} < r \leq R_{\text{outer}} \end{cases}, \quad (29)$$

which is constant in the central region of $r < R_{\text{center}}$ and decreases outward. We take the model of the protostellar core B335 adopted in Brauer et al. (2016) with $R_{\text{center}} = 1000$ au and $R_{\text{outer}} = 15000$ au. We assume the total gas mass in the protostellar core is $M_{\text{gas}} = 8M_{\odot}$, which lies in the range of gas mass between $M_{\text{gas}} = 4M_{\odot}$ and $\sim 40M_{\odot}$ for the Bok globule (Bok 1977, Leung 1985, Clemens et al. 1991). The gas density distribution on the x - z plane is illustrated in the left panel of Figure 4, with the constant gas density of $n_{\text{H}} = 7 \times 10^6 \text{ cm}^{-3}$ in the central region and $n_{\text{H}} = 4 \times 10^4 \text{ cm}^{-3}$ at $R_{\text{outer}} = 15000$ au. The magnetic field is uniform along the vertical direction z (white dashed line in the left panel of Figure 4), with the constant magnetic field strength of $B = 134 \mu\text{G}$ measured by Wolf et al. (2004) toward B335.

For the radiation source, we consider a single low-mass protostar in the center of the core and assume it is a blackbody with the temperature of $T_{\text{star}} = 6000$ K, the stellar radius of $R_{\text{star}} = 2R_{\odot}$, and the total luminosity of $L_{\text{star}} = 4.6L_{\odot}$ (Brauer et al. 2016). We also consider ISRF, which is the main source for grain alignment in the outer boundary of the protostellar envelope (Hoang et al. 2021), with

³ The choice of one cell in the azimuthal direction φ is to save the computation time due to the symmetric of gas density around the the protostar (see Appendix ??).

the spectral energy density distribution given by Mathis et al. (1983). In contrast to the protostellar source that sends out photons to the grid, photons from the interstellar radiation field (ISRF) are ejected randomly from the outer boundary of the envelope inward during the MCRT simulation. For the range of radiation field, we choose the lower limit of $\lambda_{\min} = 0.1 \mu\text{m}$ at which all shorter wavelengths are mostly absorbed by the photoionization of hydrogen atoms and the upper limit of $\lambda = 3 \text{ mm}$ at which RATs efficiency is negligible with grain size.

For the dust model, we adopt the composite grains including 67.5% of silicate and 37.5% of graphite (e.g., Draine & Hensley 2021). This composite dust model is motivated by the astro dust model proposed by Draine & Hensley (2021) and is reasonable in protostellar environments when sub-micron grains bounded by ice mantles can collide and stick together to form larger fluffy composite grains (Kataoka et al. 2013, Okuzumi et al. 2012). We assume the uniform dust-to-gas mass ratio of $\eta = 0.01$ in the entire protostellar core, and consider that they follow the standard MRN distribution $dn/da = Ca^{-3.5}$ (Mathis et al. 1977) with C the normalization constant derived from η (see Mathis et al. 1977 and the derivation in Section A). We adopt the minimum grain size of $a_{\min} = 3.5 \text{ \AA}$ and the maximum grain size of $a_{\max} = 100 \mu\text{m}$. Our choice of the maximum grain size is motivated by the detection of grains of $a > 10 \mu\text{m}$ in the envelope and the central region of Class 0 YSOs (Miotello et al. 2014, Kwon et al. 2009). Indeed, recent studies about Class II YSOs show that the maximum grain size in this stage should be $a_{\max} \leq 100 \mu\text{m}$ (see e.g., Dent et al. 2019, Okuzumi & Tazaki 2019). Thus, the presence of VLGs up to $a_{\max} = 100 \mu\text{m}$ may be not common around Class 0/I YSOs. However, Brauer et al. (2016) showed that the alignment of VLGs allows polarization by dichroic extinction to become the main source of polarization at sub-mm. Therefore, to quantify the efficiency of all available polarization mechanisms around the protostellar core, we choose $a_{\max} = 100 \mu\text{m}$. The modelling results for the maximum grain size of $a_{\max} = 10 \mu\text{m}$ are shown in Appendix E.

To model the effect of iron inclusions on grain alignment and synthetic polarizations, we consider PM grains with $f_p = 0.14285$. For SPM grains, we fix $\phi_{\text{sp}} = 0.005$ that corresponds to $\sim 1.67\%$ of iron abundance presented in the form of iron clusters (Hoang & Lazarian 2016b), and vary N_{cl} to describe different magnetic properties of grains. The parameters used in our model are summarized in Table 3.

5.2 Results for grain alignment

5.2.1 Radiation field distribution

The right panel of Figure 4 shows the radial distribution of the radiation field strength $U = u_{\text{rad}}/u_{\text{ISRF}}$ with u_{rad} the energy density of the radiation spectrum and $u_{\text{ISRF}} = 8.64 \times 10^{-13} \text{ erg cm}^{-3}$ the energy density of ISRF (Mathis et al. 1983), the mean anisotropic degree $\gamma_{\text{rad}} = \int \gamma_{\lambda} u_{\lambda} d\lambda / \int u_{\lambda} d\lambda$, and the dust temperature T_d , from top to bottom, respectively. Generally, U and T_d decrease outward due to the dust extinction. However, T_d slightly increases in the envelope scale of $r > 10000 \text{ au}$ due to the increasing contribution from ISRF and the drop of gas density in the envelope (Equation 29). The protostellar radiation field is highly anisotropic ($\gamma_{\text{rad}} \sim 1$) within 10 au from the protostar, then becomes less anisotropic (γ_{rad} decreases to ~ 0.7) outward due to the strong scattering of protostellar radiation by dust and the strong emission from hot dust in the dense central region. The radiation field becomes highly anisotropic again (γ_{rad} increases to 1) beyond $r > 1000 \text{ au}$ due to the weak interaction between thermal dust emission and dust grains in the envelope.

Table 3. Parameters used in POLARIS

Quantity	Symbol	Value
Protostellar core model and radiation sources		
Central boundary	R_{center}	1000 au
Envelope boundary	R_{outer}	15000 au
Total gas mass	M_{gas}	$8M_{\odot}$
Stellar radius	R_{star}	$2R_{\odot}$
Effective temperature	T_{star}	6000 K
Stellar luminosity	L_{star}	$4.6L_{\odot}$
Magnetic field	B	$134 \mu\text{G}$
Dust model		
Grain axial ratio	s	0.5
Dust-to-gas mass ratio	η	0.01
Grain size distribution	dn/da	$Ca^{-3.5}$
Minimum grain size	a_{\min}	3.5 \AA
Maximum grain size	a_{\max}	$100 \mu\text{m}$
Fraction of silicate		67.5%
Fraction of graphite		32.5%
Iron fraction	f_p	0.14285
Volume filling factor	ϕ_{sp}	0.005
Iron atoms/cluster	N_{cl}	$10 - 10^4$
Observation parameters		
Distance to observer		100 pc
Map size - Resolution	Full map	30000 au - 120 au
	Zoom in 1000 au	1000 au - 4 au
Wavelengths		89, 250, 450, 870 μm , 1.3 mm, 2 mm

5.2.2 Critical sizes for external alignment via B-RAT (a_{align} , $a_{\text{max,JB}}^{\text{Lar}}$)

Figure 5 shows the variation of the minimum size of external alignment determined by RATs, a_{align} (black dashed line), and the maximum size of magnetic alignment determined by the Larmor precession condition, $a_{\text{max,JB}}^{\text{Lar}}$ (solid lines) for PM and SPM at different distances to the central protostar r . Different values of N_{cl} from 100 to 10^4 are considered. Note that the range $a_{\text{align}} - a_{\text{max,JB}}^{\text{Lar}}$ determines the range of grain sizes which can be aligned with \mathbf{B} by RATs (i.e., B-RAT mechanism).

For the minimum size of B-RAT alignment, one can see that a_{align} increases continuously with radial distances due to the decrease of RAT alignment caused by the attenuation of protostellar radiation. The grain alignment size reaches the maximum of $a_{\text{align}} \sim 1 \mu\text{m}$ at the boundary between the central region and the envelope at $r \sim 10^3 \text{ au}$, then decreases to $a_{\text{align}} \sim 0.2 \mu\text{m}$ at $r = 15000 \text{ au}$ due to the additional contribution from ISRF and the reduced gas density in the envelope (see analytical studies in Hoang et al. 2021).

For the maximum size of B-RAT alignment, in the central region of $r < 1000 \text{ au}$ with the constant gas density, $a_{\text{max,JB}}^{\text{Lar}}$ increases outward due to the fast Larmor precession driven by the increased magnetic susceptibility with decreasing grain temperature (Equations 5 and 12). Beyond $r > 1000 \text{ au}$, $a_{\text{max,JB}}^{\text{Lar}}$ increases faster due to the reduced gas randomization in the envelope.

The maximum size of B-RAT alignment is larger for SPM with higher N_{cl} due to the enhanced Larmor precession by iron inclusions. Consequently, more large (micron-sized) grains are able to align with \mathbf{B} even in the dense central region of protostellar environments. In particular, PM grains cannot be aligned with \mathbf{B} in the central region with $n_{\text{H}} \sim 10^7 \text{ cm}^{-3}$ due to its slow Larmor precession, i.e.,

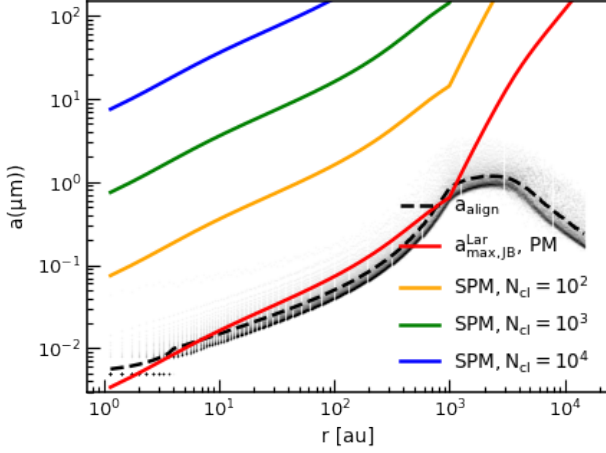


Figure 5. Variation of the average minimum a_{align} (black dashed line) and maximum alignment size $a_{\text{max},JB}^{\text{Lar}}$ (color lines) as a function of distance r of PM and SPM grains with different N_{cl} , assuming $\phi_{\text{sp}} = 0.005$. Within 1000 au, the alignment range shifts from sub-micron size near the protostar to micron size at $r \sim 1000$ au due to the reduced RAT alignment efficiency by dust extinction. Beyond 1000 au, the alignment range is broader, i.e., smaller a_{align} and larger $a_{\text{max},JB}^{\text{Lar}}$, due to the enhanced RAT alignment by ISRF and the reduced gas randomization in the envelope. More large grains can be aligned with **B** with increasing N_{cl} due to the enhanced Larmor precession by iron inclusions. Typically, VLGs can have the magnetic alignment even in the central region with $n_{\text{H}} = 1.6 \times 10^7 \text{ cm}^{-3}$ if they have $N_{\text{cl}} \geq 10^4$ and $\phi_{\text{sp}} \geq 0.005$.

$a_{\text{max},JB}^{\text{Lar}} < a_{\text{align}}$. In contrast, VLGs can have magnetic alignment in this region if they are SPM with $N_{\text{cl}} \sim 10^4$ and $\phi_{\text{sp}} = 0.005$.

5.2.3 Critical sizes with fast internal relaxation ($a_{\text{min},aJ}$, $a_{\text{max},aJ}$)

The left panel of Figure 6 shows the variation at different distances r of the minimum size, $a_{\text{min},aJ}^{\text{high-J}}$ (dashed lines), and maximum size, $a_{\text{max},aJ}^{\text{high-J}}$ (solid lines), of grains having fast internal relaxation by Barnett relaxation for PM and SPM grains aligned with **B** at high- J attractors. The range of grains having fast internal relaxation is more extended toward the protostar, i.e., broader range of $a_{\text{min},aJ}^{\text{high-J}} - a_{\text{max},aJ}^{\text{high-J}}$, due to the faster Barnett relaxation driven by suprathermal rotation of grains by efficient RATs. In the inner region of the envelope of $r \sim 5000$ au, grains tend to have slow internal relaxation due to the reduced Barnett relaxation as a result of the slow rotation of grains in attenuated radiation fields. In the outer envelope of $r > 5000$ au, aligned grains can have fast internal relaxation again due to the increased grain rotational rate by ISRF and the decreased gas randomization. The size range of fast internal relaxation is more extended to large micron-sized grains and also in space for SPM grains with larger N_{cl} due to stronger Barnett relaxation by iron inclusions. For example, all SPM grains of $a \geq a_{\text{align}}$ (black dashed line) can have fast internal relaxation at high- J attractors and then efficient IA in the entire protostellar core with $N_{\text{cl}} \sim 10^4$ and $\phi_{\text{sp}} = 0.005$.

The right panel of Figure 6 shows the similar results as the left panel but for grains aligning with **B** at low- J attractors. In contrast to the complex variation of grains with fast internal relaxation at distances at high- J attractors, the size range of grains with fast relaxation at low- J attractors simply increases from the central region toward the envelope due to the reduced effect of gas randomization.

This simple tendency is because grains at low- J attractors rotate with the thermal angular velocity Ω_T which is not sensitive to the change in the radiation field as grains at high- J attractors. The smaller value of $a_{\text{max},aJ}^{\text{low-J}}$ in the central region is caused by the decrease of the magnetic susceptibility with increasing grain temperature near the protostellar source (Equations 1 and 3 and Figure 4, right panel). The size range of grains with fast relaxation is extended for SPM grains with larger N_{cl} . However, for grains at low- J , only small grains of $a < 1 \mu\text{m}$ can have fast relaxation, while larger grains of $a > 1 \mu\text{m}$ always have slow internal relaxation due to their slow rotation.

5.2.4 Critical sizes for magnetically enhanced RAT alignment (MRAT), $a_{\text{max},JB}^{\text{DG}}$

Figure 7 shows our numerical results for the critical sizes at which the magnetic relaxation is efficient in enhancing the RAT alignment (i.e., the MRAT mechanism), $a_{\text{max},JB}^{\text{DG},0.5}$ (solid lines) and $a_{\text{max},JB}^{\text{DG},1}$ (dashed lines), for different magnetic properties of grains. For PM grains (red lines), they are mainly aligned by RATs because of the negligible effect of magnetic relaxation, i.e., $a_{\text{max},JB}^{\text{DG},0.5} \ll a_{\text{align}}$. In contrast, SPM grains with high N_{cl} can have efficient external alignment in the envelope by the MRAT mechanism. In particular, the high level of iron inclusions with $N_{\text{cl}} = 10^4$ and $\phi_{\text{sp}} = 0.005$ allows 100% of grains to be aligned with **B** at high- J attractors beyond ~ 1000 au.

However, the high level of iron inclusions cannot significantly increase the efficiency of MRAT alignment in the central region of $r < 1000$ au, i.e., $a_{\text{max},JB}^{\text{DG}}$ drops toward the center. The decreased magnetic relaxation is due to the decrease of the magnetic susceptibility with increasing grain temperature toward the protostar (Equations 1 and 3). In addition, the increase in gas randomization also results in the reduction of the efficiency of the MRAT mechanism here. Thus, grains in the central region are mainly aligned with **B** by RATs with the typical values of $f_{\text{high-J}} = 0.25$.

6 EFFECT OF IRON INCLUSIONS ON POLARIZATION PATTERN

Using above critical sizes for grain alignment, we can calculate the new Rayleigh reduction factor R described in Section 4.2.5 and use it to model synthetic polarization maps at optically thin wavelengths of $870 \mu\text{m}$ and $450 \mu\text{m}$ (Table 5), which can be observed by ALMA. We place the detector at 100 pc from the protostellar core along y direction. The plane detector has $N_x \times N_z = 250 \times 250$ pixels on x direction and z direction, giving the spatial resolution of 120 au when observing the entire protostellar core of 30000 au and 4 au when zooming into the central region of scale 1000 au (Observation parameters are summarized in Table 3).

We first consider the model Ideal in which all grains larger than a_{align} have the perfect alignment with **B**, i.e., $f_{\text{high-J}} = 1$. Then, we consider the realistic models that include the new effects of slow Larmor precession, slow internal relaxation, and the enhanced external alignment by the MRAT mechanism as presented in Section 4.2. As discussed in Section 4.2.3, grains with slow internal relaxation at low- J attractors can have right or wrong IA. However, the fraction and conditions that drive the grain internal alignment state are still unclear. Therefore, we consider two scenarios, the first scenario with 100% of grains with slow internal relaxation at low- J having right IA, denoted as model Realistic-rIA, and the second case with 100% of grains with slow internal relaxation at low- J attractors having wrong IA, denoted as Realistic-wIA. The summary of parameters of our models are listed in the first four rows in Table 4.

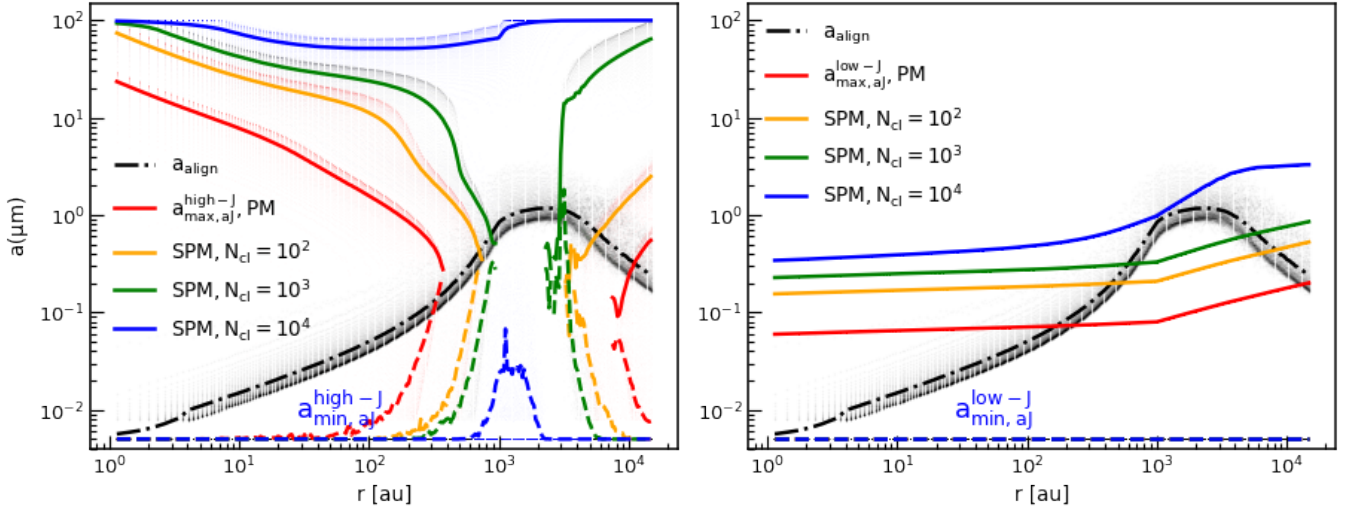


Figure 6. Variation of the average minimum and maximum size with fast internal relaxation for PM and SPM grains with different N_{cl} . The left panel shows the results for grains aligned with \mathbf{B} at high- J attractors ($a_{min,aj}^{high-J} - a_{max,aj}^{high-J}$), and the right panel is for grains at low- J attractors ($a_{min,aj}^{low-J} - a_{max,aj}^{low-J}$). At high- J , the range of grains with fast internal relaxation is broader near the protostar and in the outer boundary of the envelope irradiated by ISRF. In contrast, at low- J , grains tend to have fast internal relaxation in the envelope due to the reduced gas randomization. However, grains only rotate at thermal rotation, thus, all large grains of $a \geq 1 \mu\text{m}$ cannot have fast internal relaxation.

Table 4. Parameters of the grain alignment model

Model name	$a_{max} (\mu\text{m})$	Magnetic properties	Slow Larmor precession	Slow internal relaxation	Internal Alignment at low- J attractors	$B (\mu\text{G})$
Ideal ¹	100	--	no	no	right IA ($\hat{\mathbf{a}}_1 \parallel \mathbf{J}$)	134
Realistic ² -rIA	100	PM, SPM	yes	yes	right IA	134
Realistic-wIA	100	PM, SPM	yes	yes	wrong IA ($\hat{\mathbf{a}}_1 \perp \mathbf{J}$)	134
Realistic-rIA-amax	[5 – 150] ³	PM, SPM	yes	yes	right IA	134
Realistic-wIA-amax	[5 – 150]	PM, SPM	yes	yes	wrong IA	134
Realistic-rIA-amax-B	[5 – 150]	PM, SPM	yes	yes	right IA	[134 – 1000] ⁴
Realistic-wIA-amax-B	[5 – 150]	PM, SPM	yes	yes	wrong IA	[134 – 1000]
Ideal-a10	10	--	no	no	right IA	134
Realistic-rIA-a10 ⁵	10	PM, SPM	yes	yes	right IA	134
Realistic-wIA-a10	10	PM, SPM	yes	yes	wrong IA	134

(¹): In Ideal model, all grains of $a \geq a_{align}$ are considered to align with \mathbf{B} , with $f_{high-J} = 1$.

(²): In Realistic model, all effects described from Section 4.2.2 to Section 4.2.4 are taken into account, with the maximum alignment size is determined by the condition $\tau_{Lar} \leq \tau_{gas}/10$, the grain with fast internal relaxation is determined by condition $\tau_{BR} \leq \tau_{gas}$, and f_{high-J} varies with δ_m given by Equation (28).

(³): The maximum grain size a_{max} varies from $5 \mu\text{m}$ to $150 \mu\text{m}$.

(⁴): Consider two values of magnetic fields, $B = 1000 \mu\text{G}$ in the central 1000 au region and $B = 100 \mu\text{G}$ in the envelope.

(⁵): Results for model ... - a10 are shown in Appendix E.

Table 5. Optical depth in the central region of 1000 au scale

Wavelength	89 μm	250 μm	450 μm	870 μm	2 mm
τ_λ	2.75	1.14	0.59	0.08	0.02

Figures 8 and 9 show the comparison of the synthetic polarization pattern obtained from the protostellar envelope and the central region of 1000 au on x-z plane at 870 μm (upper panels) and 450 μm (lower panels) between model Ideal (first column) and model Realistic-rIA (second to fourth columns). The color code shows the polarization fraction p (%), black segments show polarization vectors \mathbf{P} with the length representing the degree of polarization. The magnetic field is

along the vertical direction (z-axis). One can clearly see that with the presence of grains with slow internal relaxation, both PM and SPM grains with $N_{cl} = 100$ or $N_{cl} = 10^4$ produce the uniform polarization pattern with $\mathbf{P} \perp \mathbf{B}$ as the Ideal model if they have right IA with $\hat{\mathbf{a}}_1 \parallel \mathbf{J}$. The polarization pattern is uniform in the entire protostellar core and does not change with wavelengths. In addition, the polarization degree along the equatorial plane is smaller than ones at higher latitudes. It is a result of the reduced RAT alignment efficiency, i.e., larger a_{align} , and the reduced amount of grains having perfect magnetic alignment, i.e., smaller $a_{max,JB}^{DG,0.5}$ and $a_{max,JB}^{DG,1}$, in the area where the radiation field is perpendicular to B-fields (see Appendix C for the detailed variation of grain alignment on x and z direction).

However, if grains with slow internal relaxation have wrong IA with $\hat{\mathbf{a}}_1 \perp \mathbf{J}$ (model Realistic-wIA), the synthetic polarization pat-

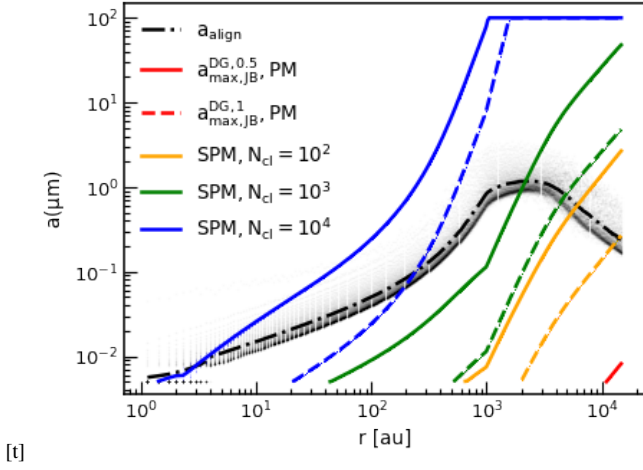


Figure 7. Variation of the maximum size for magnetic alignment by the MRAT mechanism, $a_{\max,JB}^{DG,0.5}$ and $a_{\max,JB}^{DG,1}$, for PM and SPM grains with different N_{cl} . The values of $a_{\max,JB}^{DG}$ increase with increasing N_{cl} , but decrease toward the central protostar. The range of grains with efficient external alignment ($a \sim [a_{align} - a_{\max,JB}^{DG}]$) is more extended in the envelope due to the reduced gas randomization.

tern becomes much more complicated depending on the level of iron inclusions locked inside dust grains. The results obtained in the envelope for model Realistic-wIA is shown in Figure 10.

In particular, PM grains (second column) produce the uniform polarization pattern in the entire envelope at $870\ \mu\text{m}$ and $450\ \mu\text{m}$, but with $\mathbf{P} \parallel \mathbf{B}$ arising from the emission of grains with wrong IA (i.e., most PM grains have slow internal relaxation, Figure 6, left panel, red line). For SPM with the moderate level of iron inclusions ($N_{cl} = 100$, third column), the polarization pattern is uniform with $\mathbf{P} \parallel \mathbf{B}$ at $870\ \mu\text{m}$ because VLGs in the envelope have wrong IA by slow internal relaxation. At shorter wavelengths of $450\ \mu\text{m}$, the polarization pattern becomes complicated with $\mathbf{P} \perp \mathbf{B}$ beyond ~ 5000 au and $\mathbf{P} \parallel \mathbf{B}$ in the inner region. The change of the polarization pattern in the outer envelope is caused by the change in IA of the emission source from VLGs with wrong IA to micron-sized grains with right IA. In contrast, the polarization pattern with $\mathbf{P} \parallel \mathbf{B}$ within 5000 au does not change with wavelengths because most of grains have slow internal relaxation with wrong IA here (Figure 6, left panel).

If SPM grains have the high level of iron inclusion ($N_{cl} = 10^4$, fourth column), they can produce the uniform polarization pattern with $\mathbf{P} \perp \mathbf{B}$ in the entire envelope at both $870\ \mu\text{m}$ and $450\ \mu\text{m}$ as the Ideal model (first column). Such polarization pattern is achieved due to the efficient IA of all aligned grain in the envelope driven by the fast Barnett relaxation.

Figure 11 shows the similar results as Figure 10 but zoom in into 1000 au from the center. For PM and SPM grains with $N_{cl} = 100$ (second and third columns), the polarization pattern is uniform with $\mathbf{P} \parallel \mathbf{B}$ at $870\ \mu\text{m}$ due to the emission of VLGs with wrong IA. At $450\ \mu\text{m}$, it becomes complicated with $\mathbf{P} \parallel \mathbf{B}$ beyond 300 au and $\mathbf{P} \perp \mathbf{B}$ within 300 au from the protostar. The change of the polarization pattern in the inner ~ 300 au region with wavelengths is due to the change in IA of the emission source from VLGs with wrong IA to micron-sized grains with right IA. Indeed, for PM grains, grains in the central region do not radiate polarized emission because they are not aligned with \mathbf{B} here (Figure 5, red line). Therefore, the polarization vectors $\mathbf{P} \perp \mathbf{B}$ in the inner ~ 200 au region at $450\ \mu\text{m}$ (second

column) is originated from the polarized emission of sub-micron grains with efficient IA in the boundary of the envelope (Figure 6, left panel, red line). For SPM with $N_{cl} = 100$, they can have the magnetic alignment and also efficient IA in the central region. The polarization signal with $\mathbf{P} \perp \mathbf{B}$ in the inner ~ 300 au region at $450\ \mu\text{m}$ (third column) thus comes from both the emission of aligned dust grains with efficient IA within ~ 400 au from the protostar and beyond 4000 au in the envelope (Figure 6, left panel, orange line). For SPM grains with high $N_{cl} = 10^4$, the polarization pattern is uniform with $\mathbf{P} \perp \mathbf{B}$ at both $870\ \mu\text{m}$ and $450\ \mu\text{m}$ as the Ideal model because of the efficient grain alignment by the MRAT mechanism.

7 EFFECT OF IRON INCLUSIONS ON $P - I$ RELATIONSHIP

In all polarization maps shown in Section 6, one can see that the polarization degree tends to decrease toward the central region. In this section, we will study in detail the dependence of the polarization degree $p(\%)$ on the magnetic properties of grains.

Figure 12 shows the variation of polarization degree $p(\%)$ with normalized intensity I/I_{\max} with I_{\max} the maximum intensity of thermal emission obtained in the center of the protostellar core. The projected distances to the center on x-z plane d_{proj} corresponding to each value of I/I_{\max} are shown in the upper x axis. Scattered points represent the values of $p - I/I_{\max}$ on the ring of height $d_{\text{resol}} = 120$ au and radius of d_{proj} , solid color lines show the average polarization degree obtained by our models for different magnetic properties of grains. The result from model Ideal is plotted by the black dashed line for comparison.

The upper left panel of Figure 12 shows the results obtained at $870\ \mu\text{m}$ for model Realistic-rIA. In contrast to the constant $p \sim 45\%$ with distances in Ideal model, the calculated polarization degree for model Realistic-rIA decreases continuously with increasing intensity toward the center, and generally is larger for SPM grains with higher fraction of iron inclusions. Particularly, PM grains only produce the constant low $p \sim 3\%$ in the envelope, i.e., $d_{\text{proj}} > 5000$ au, because they mainly have inefficient IA driven by slow internal relaxation. Moving toward the center, p decreases to negligible values due to the loss of grain alignment within 1000 au (Figure 5). In contrast, SPM grains with N_{cl} changing from 100 to 10^4 produce the constant high polarization degree from $p \sim 4\%$ up to $p \sim 45\%$ in the envelope due to the increase of amount of grains with efficient IA at high- J attractors, i.e., higher $f_{\text{high-}J}$ and broader range of $a_{\min,AJ}^{\text{high-}J} - a_{\max,AJ}^{\text{high-}J}$ (Figures 6 and 7). The polarization degree produced by SPM slightly decreases to $p \sim 3 - 10\%$ near the center due to the reduced internal and external alignment by the MRAT mechanism in the dense central region.

The upper right panel of Figure 12 shows the variation of $p(\%)$ with I/I_{\max} obtained for model Realistic-wIA at $870\ \mu\text{m}$. Similar as the left panel for model Realistic-rIA, one obtains the decrease of p with increasing intensity due to the reduced grain alignment efficiency by the MRAT mechanism in dense environments and the increase of p with increasing levels of iron locked inside dust grains. However, the polarization degree produced by model Realistic-wIA is slightly smaller than model Realistic-rIA as a result of the cancelling effect between polarized emission from grains with right and wrong IA.

The lower left (for model Realistic-rIA) and lower right panels (for model Realistic-wIA) of Figure 12 show the similar results as the upper panels, but for the wavelength of $450\ \mu\text{m}$. Generally, one can obtain the similar reduction of p with I/I_{\max} and the rise of

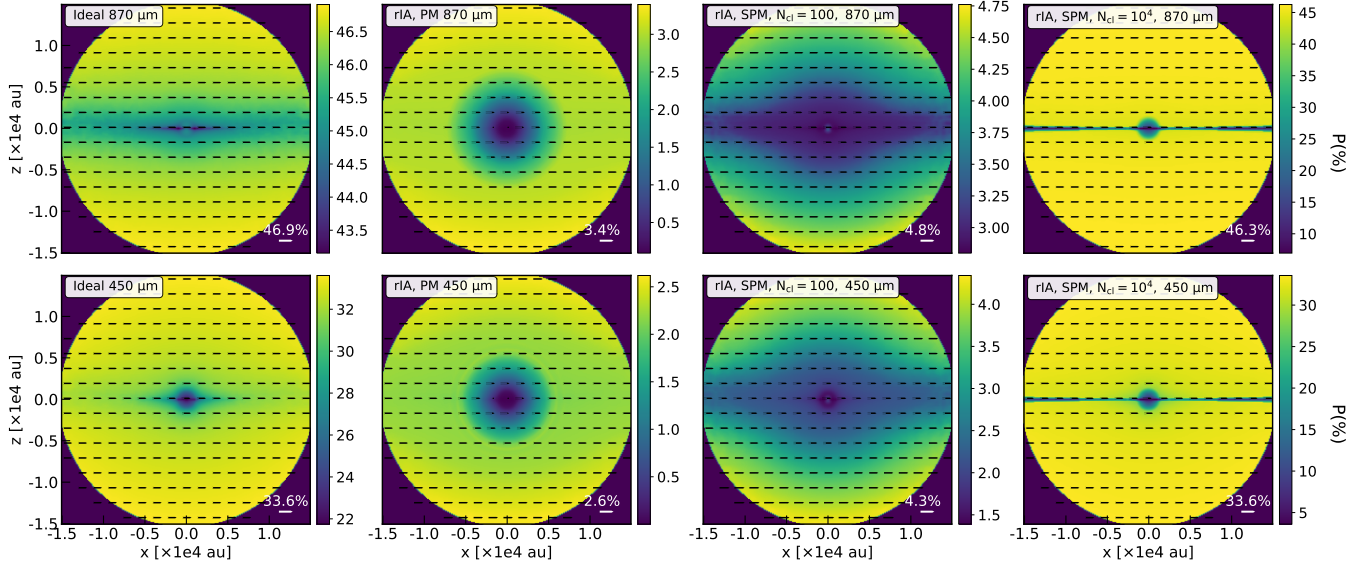


Figure 8. Synthetic polarization maps obtained in the envelope on the x - z plane at $870\ \mu\text{m}$ (upper panels) and $450\ \mu\text{m}$ (lower panels) for model Ideal (first column) and model Realistic-rIA for PM grains (second column) and SPM grains with $N_{\text{cl}} = 100$ (third column) and $N_{\text{cl}} = 10^4$ (fourth column). The color code shows the polarization degree, black segments show polarization vectors \mathbf{P} scaled with the polarization degree, the magnetic field is along the vertical direction (z axis). Our models of PM and SPM grains show the uniform polarization pattern with $\mathbf{P} \perp \mathbf{B}$ at $870\ \mu\text{m}$ and $450\ \mu\text{m}$ because all aligned dust grains have right IA. The polarization degree generally decreases inward due to the reduced grain alignment efficiency in the dense central region. The lower p on the equatorial plane is due to the reduced RATs efficiency, i.e., larger a_{align} , and the reduced amount of grains with perfect magnetic alignment, i.e., smaller $a_{\text{max,JB}}^{\text{DG},1}$ and $a_{\text{max,JB}}^{\text{DG},1}$.

where $\mathbf{k} \perp \mathbf{B}$ (see Appendix C for details).

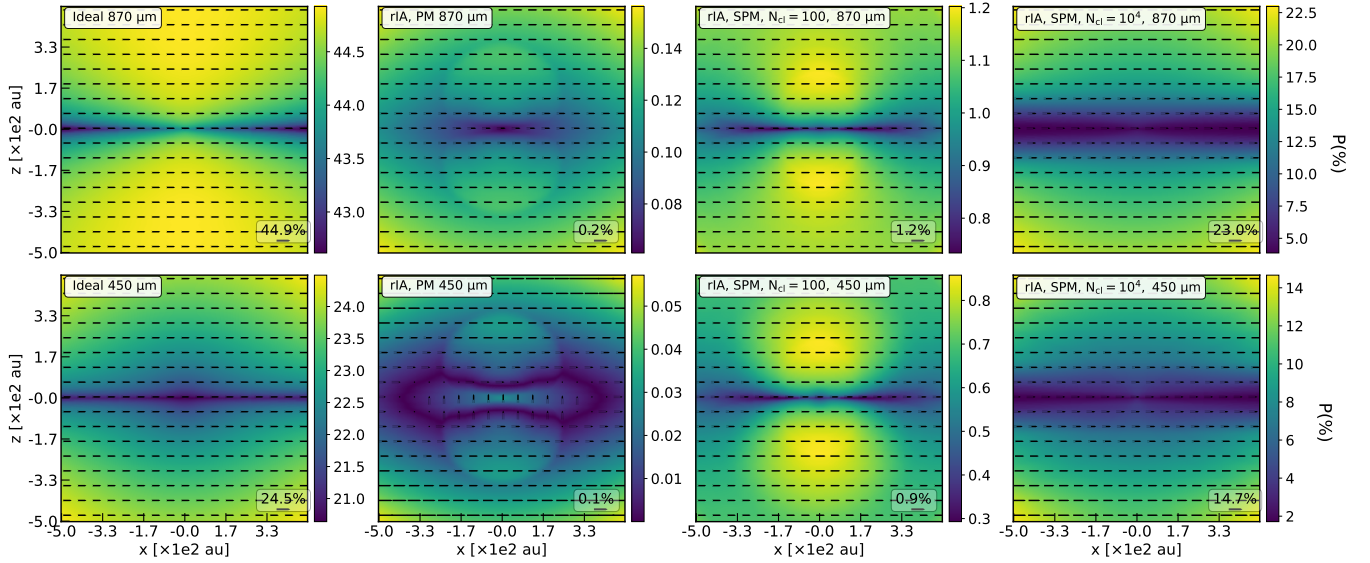


Figure 9. Similar as Figure 8 but focusing in the central region of scale 1000 au. The polarization patterns produced by both PM and SPM grains are uniform with $\mathbf{P} \perp \mathbf{B}$ at both $870\ \mu\text{m}$ and $450\ \mu\text{m}$ if all grains have right IA. The polarization degree is slightly smaller on the equatorial plane due to the reduced RAT efficiency when $\mathbf{k} \perp \mathbf{B}$.

p with N_{cl} as the calculation at $870\ \mu\text{m}$. However, in contrast to the smooth reduction of $p(450\ \mu\text{m})$ with I/I_{max} produced by model Realistic-rIA, in model Realistic-wIA, one can see the sudden drop of the polarization degree to $p < 1\%$ at the distance where the polarization degree changes from high value of $p \sim 10 - 45\%$ in

the envelope to low $p \sim 1\%$ in the center, which is termed as the "valley-polarization hole". The presence of the polarization valley is originated from the cancelling effect of the polarization signal radiating from grains with right and wrong IA. The V-shape of the $p - I/I_{\text{max}}$ curve corresponds to the gap with $p < 1\%$ between the

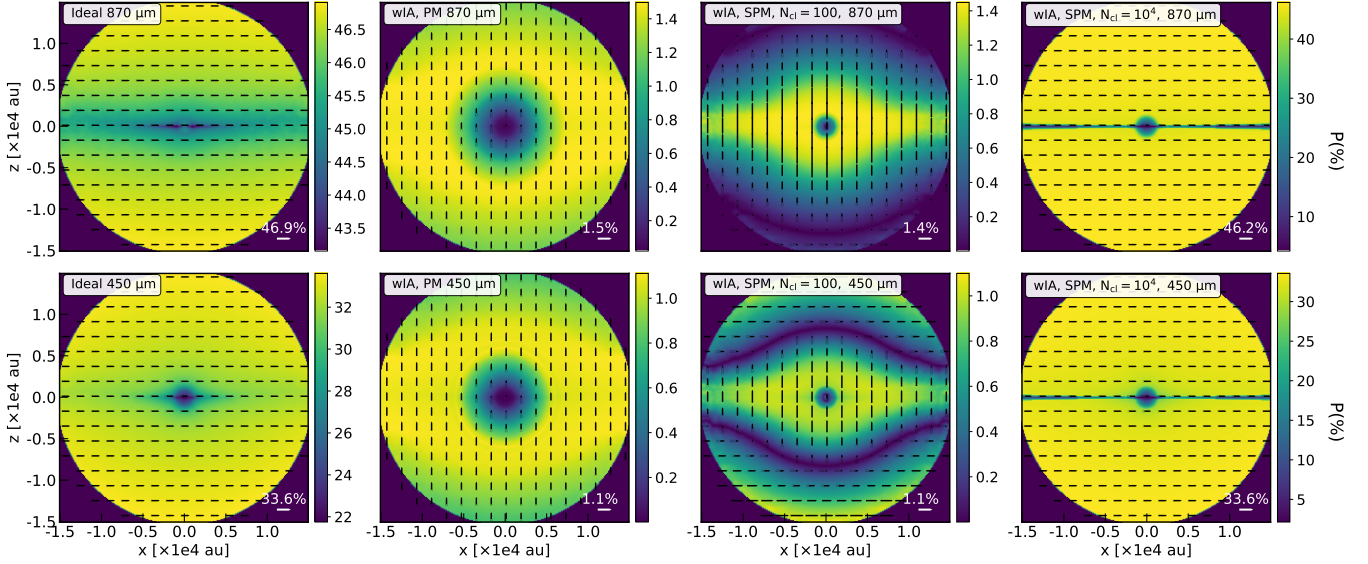


Figure 10. Synthetic polarization maps produced by Ideal model (first column) and model Realistic–wIA for PM grains and SPM grains with $N_{cl} = 100$ and 10^4 (second to fourth columns). With the presence of grains with wrong IA by slow internal relaxation, PM grains produce the uniform polarization pattern with $\mathbf{P} \parallel \mathbf{B}$ at both $870 \mu\text{m}$ and $450 \mu\text{m}$ due to the dominant emission from VLGs with wrong IA. SPM grains with $N_{cl} = 100$ produce the uniform polarization pattern with $\mathbf{P} \parallel \mathbf{B}$ at $870 \mu\text{m}$, but the complex one with $\mathbf{P} \perp \mathbf{B}$ beyond ~ 5000 au and $\mathbf{P} \parallel \mathbf{B}$ within 5000 au at $450 \mu\text{m}$. The variation of \mathbf{P} with wavelengths beyond ~ 5000 au is driven by the change in IA of the emission source, from VLGs with wrong IA to micron-sized grains with right IA (Figure 6, left panel). In contrast, SPM grains with $N_{cl} = 10^4$ produce the uniform polarization pattern with $\mathbf{P} \perp \mathbf{B}$ as model Ideal due to enhanced grain alignment by the MRAT alignment.

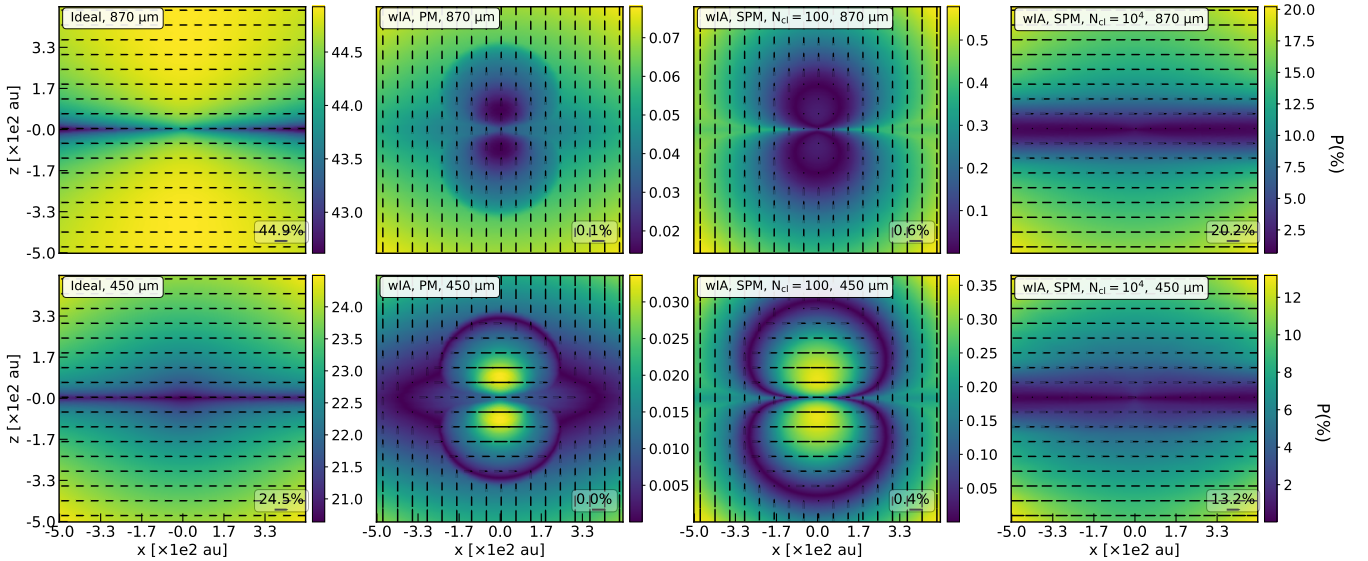


Figure 11. Similar to Figure 10 but zoom in into the inner region of 1000 au around the protostar. For PM and SPM with $N_{cl} = 100$, polarization vectors are uniform with $\mathbf{P} \parallel \mathbf{B}$ at $870 \mu\text{m}$ but become complicated with $\mathbf{P} \parallel \mathbf{B}$ beyond 200 au and $\mathbf{P} \perp \mathbf{B}$ within 200 au at $450 \mu\text{m}$. The polarization flipping in the center is due to the change of the emission source from VLGs with wrong IA to micron-sized grains with right IA. In contrast, SPM grains with $N_{cl} = 10^4$ produce the uniform polarization pattern with $\mathbf{P} \perp \mathbf{B}$ at both $870 \mu\text{m}$ and $450 \mu\text{m}$ as Ideal model because most grains of $a \geq 1 \mu\text{m}$ can have efficient IA even in the central region.

outer envelope with $\mathbf{P} \perp \mathbf{B}$ and the inner region with $\mathbf{P} \parallel \mathbf{B}$ shown in the third column of Figure 10. The second change of the polarization pattern from $\mathbf{P} \parallel \mathbf{B}$ beyond > 300 au to $\mathbf{P} \perp \mathbf{B}$ within ~ 300 au (Figure 11, third column) is also featured by the second valley at $d_{\text{proj}} < 500$ au (the orange and green lines in the upper right panel).

8 EFFECT OF IRON INCLUSIONS ON THE POLARIZATION BY DICHOIC EXTINCTION

Next, we examine the effect of iron inclusions on the polarization by dichroic extinction of aligned dust grains. Brauer et al. (2016) sug-

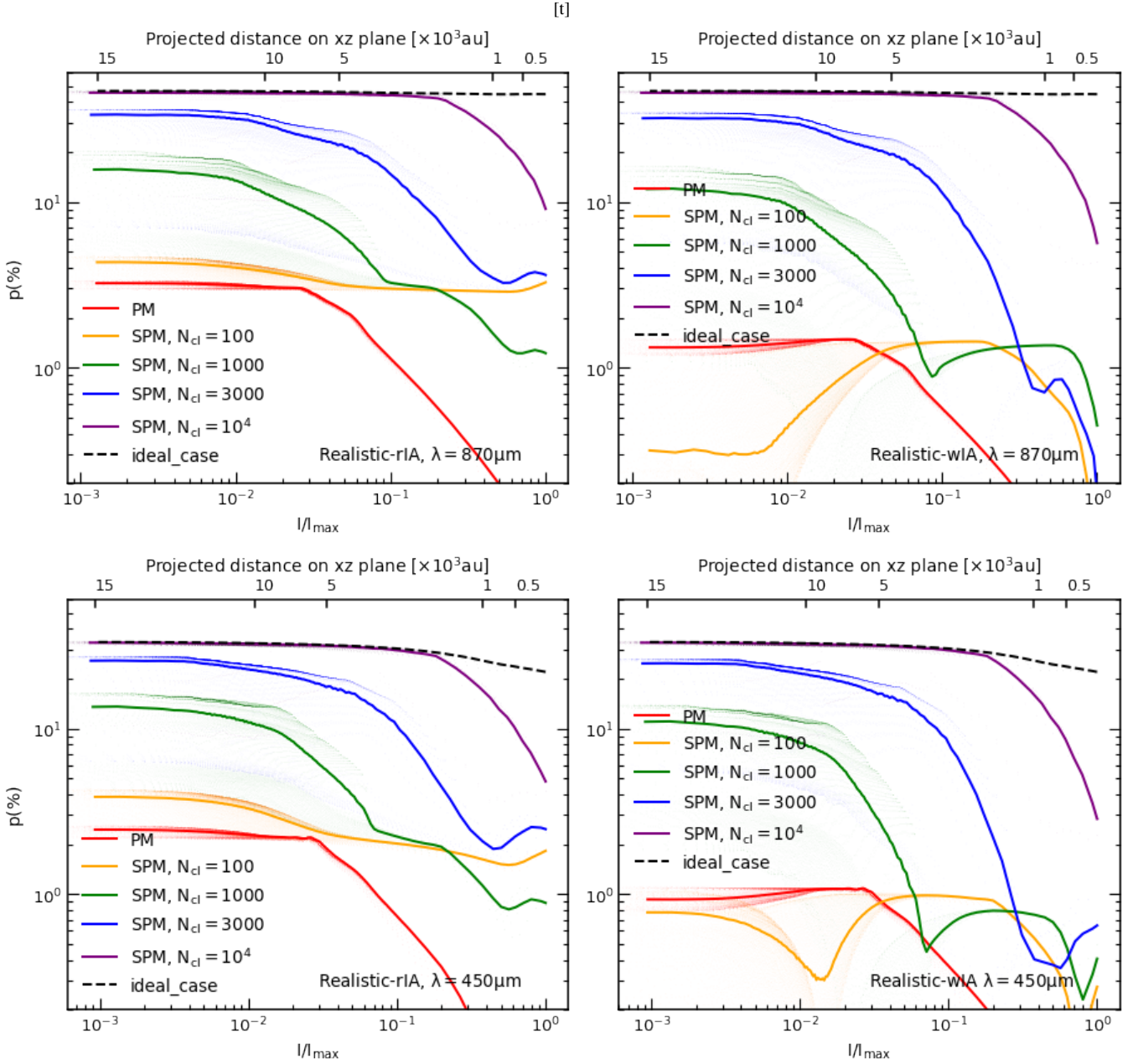


Figure 12. Variation of the polarization degree at $870\ \mu\text{m}$ (upper panels) and $450\ \mu\text{m}$ (lower panels) with the normalized intensity I/I_{max} for different magnetic properties of grains. The result from model Ideal is plotted by the black dashed line for comparison. The left panel shows the results for model Realistic-rIA, and the right panel is for model Realistic-wIA. In our models, the polarization degree always decreases with increasing I/I_{max} and generally increases with increasing N_{cl} . And this feature is not different between the calculations at $870\ \mu\text{m}$ and $450\ \mu\text{m}$. In addition, if grains with wrong IA exist in the core, one will obtain the “valley-polarization hole” with $p < 1\%$ in $p - I/I_{\text{max}}$ curve caused by the cancelling effect of polarized emission from grains with wrong and right IA.

gested that the dichroic extinction by aligned VLGs in protostellar cores can reduce polarized thermal emission and become the main source of polarization at sub-mm wavelengths. We first study the effect of iron inclusions on the polarization pattern observed in optically thick wavelengths of $250\ \mu\text{m}$ and $89\ \mu\text{m}$ (Table 5) in Section 8.1 and the relationship of $p - I/I_{\text{max}}$ in Section 8.2.

8.1 Polarization maps

Figure 13 shows the polarization maps obtained in the central region of $1000\ \text{au}$ at $250\ \mu\text{m}$ (upper panels) and $89\ \mu\text{m}$ (lower panels) for model Ideal in the first column and model Realistic-rIA for PM and SPM in other columns. In the Ideal model, the polarization pattern changes from $\mathbf{P} \perp \mathbf{B}$ at $250\ \mu\text{m}$ to $\mathbf{P} \parallel \mathbf{B}$ at $89\ \mu\text{m}$ due to the change in the polarization mechanism from dichroic emission to dichroic extinction by aligned VLGs. For our model of PM grains (second column), the polarization pattern is uniform with $\mathbf{P} \parallel \mathbf{B}$ at both $250\ \mu\text{m}$ and $89\ \mu\text{m}$ as a result of the polarization by dichroic extinc-

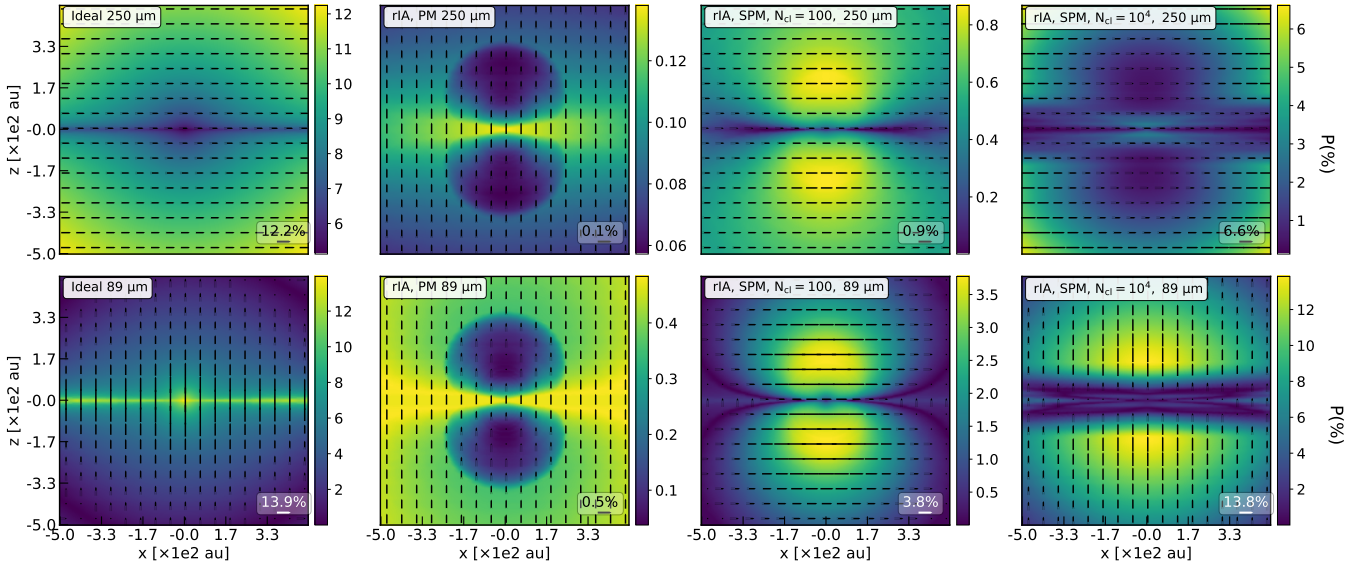


Figure 13. Synthetic polarization maps calculated in the central region of 1000 au at $250\ \mu\text{m}$ (upper panels) and $89\ \mu\text{m}$ (lower panels) for model Ideal and model Realistic–rIA for PM and SPM grains. In the Ideal model and our model for SPM grains with $N_{\text{cl}} = 10^4$, the polarization pattern can rotate 90° from $\mathbf{P} \perp \mathbf{B}$ at $250\ \mu\text{m}$ to $\mathbf{P} \parallel \mathbf{B}$ at $89\ \mu\text{m}$ due to the change of the polarization mechanism from dichroic emission to dichroic extinction. This effect does not happen for SPM grains with low $N_{\text{cl}} = 100$ because of the reduced polarization by dichroic extinction caused by the weak alignment of VLGs with \mathbf{B} .

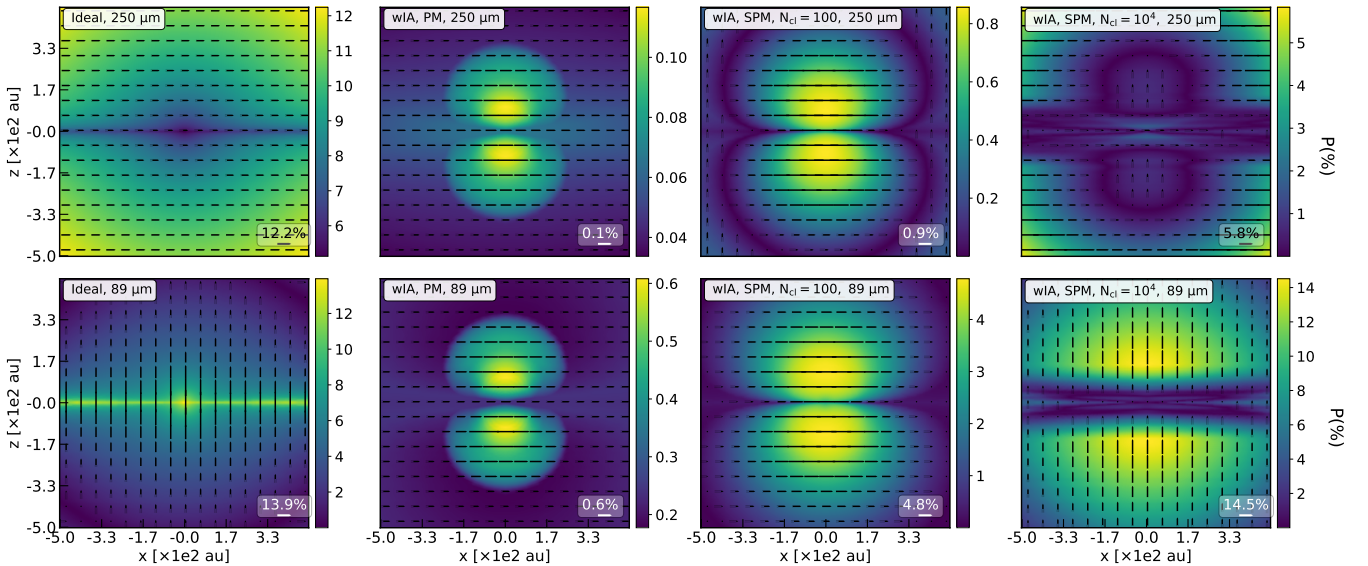


Figure 14. Similar results as Figure 13 but for model Realistic–wIA. The 90° flipping of \mathbf{P} due to the change of the polarization mechanism only happens for SPM grains with high $N_{\text{cl}} = 10^4$. For PM and SPM grains with $N_{\text{cl}} = 100$, dichroic emission is still the main source of polarization at optically thick wavelengths due to the reduced alignment degree of VLGs with \mathbf{B} .

tion by aligned VLGs. The reason for the efficient polarization by dichroic extinction is as follows. For PM, most of aligned grains in the protostellar envelope have the inefficient IA by slow internal relaxation. Thus, VLGs can strongly attenuate polarized thermal emission from micron-sized aligned dust grains, letting dichroic extinction be the main source of polarization at optically thick wavelengths of $\lambda \leq 250\ \mu\text{m}$.

In contrast, the polarization pattern produced by SPM grains with $N_{\text{cl}} = 100$ (third column) is uniform in the central region with $\mathbf{P} \perp$

\mathbf{B} at both $250\ \mu\text{m}$ and $89\ \mu\text{m}$. The independence of \mathbf{P} with wavelengths ($\mathbf{P} \perp \mathbf{B}$ from $870\ \mu\text{m}$ to $89\ \mu\text{m}$, Figure 11) is explained as follows. For SPM grains with $N_{\text{cl}} = 100$, sub-micron and micron-sized aligned grains near the protostar and in the outer envelope can have efficient IA by enhanced Barnett relaxation by iron inclusions. However, VLGs have inefficient IA due to slow internal relaxation due to their larger sizes (Figure 6). Consequently, VLGs cannot efficiently attenuate polarized emission from smaller grains. As a result, dichroic emission is still the main polarization mechanism at

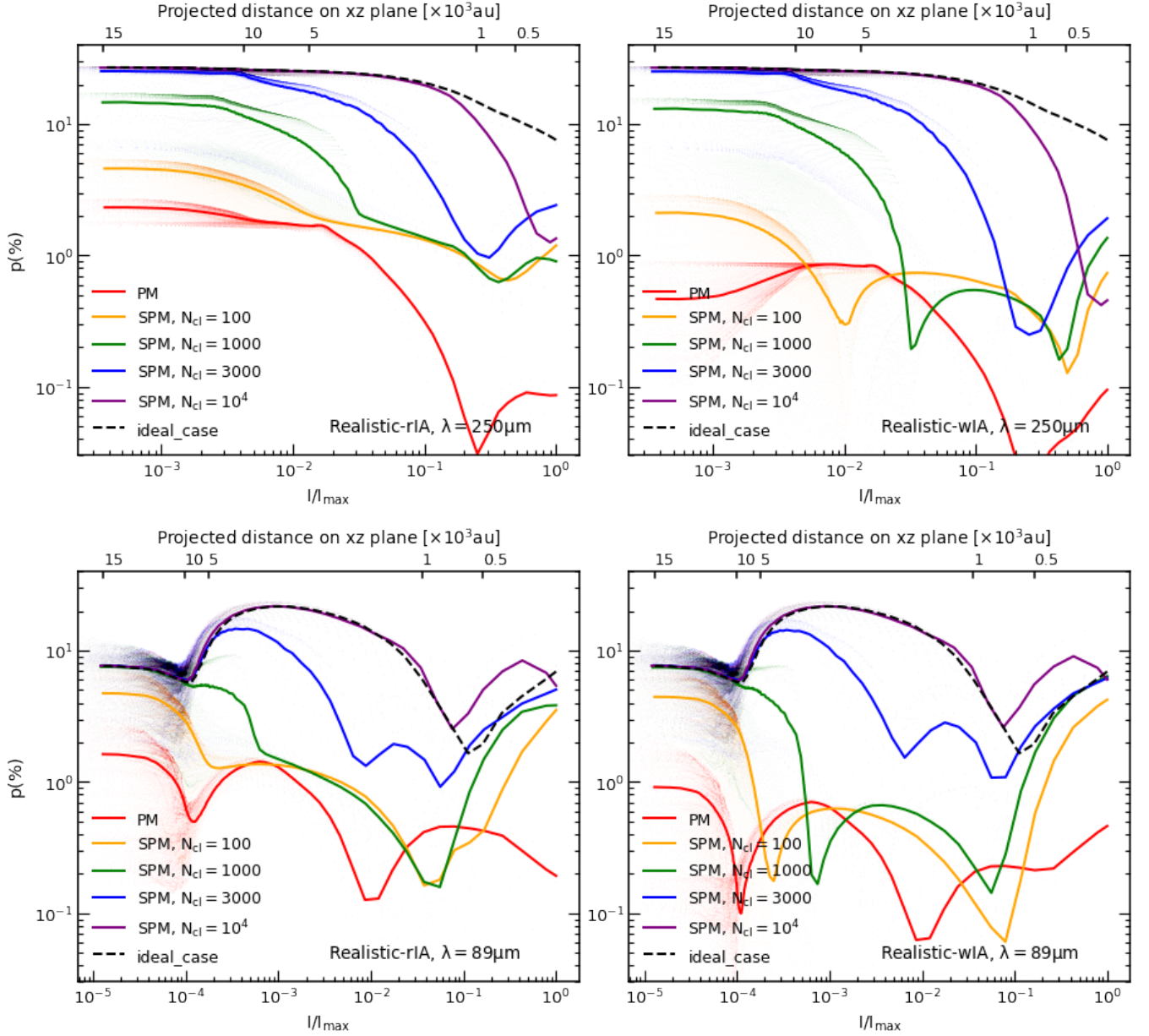


Figure 15. Effect of iron inclusions on the variation of p with I/I_{\max} at $250\,\mu\text{m}$ (upper panels) and $89\,\mu\text{m}$ (lower panels) for model Realistic-rIA (left column) and Realistic-wIA (right column). At $250\,\mu\text{m}$, the polarization degree produced by model Ideal (black dashed line) slightly decreases with increasing intensity due to the extinction effect by aligned VLGs. Our models also show the reduction of p with I/I_{\max} , but with steeper slope due to the additional effect from the weak grain alignment by the MRAT mechanism in dense environments. The variation of p with I/I_{\max} is more complicated at $89\,\mu\text{m}$ due to the joint polarization by dichroic emission from micron-sized grains and dichroic extinction by VLGs. But in general, grains with higher N_{cl} produce high $p(\%)$ due to enhanced MRAT efficiency on grains.

optically thick wavelengths of $\lambda \leq 250\,\mu\text{m}$. The situation will be different for SPM grains with $N_{\text{cl}} = 10^4$ (fourth column). The polarization pattern can change from $\mathbf{P} \perp \mathbf{B}$ at $250\,\mu\text{m}$ to $\mathbf{P} \parallel \mathbf{B}$ at $89\,\mu\text{m}$ due to the change of the polarization mechanism as model Ideal. The activation of the polarization by dichroic extinction here is due to the enhanced internal and external alignment of VLGs by efficient MRAT alignment.

Figure 14 shows the similar results as Figure 13 but for model Realistic-wIA. For PM and SPM grains with $N_{\text{cl}} = 100$, one gets the uniform polarization pattern with $\mathbf{P} \perp \mathbf{B}$ as a result of the dichroic

emission of aligned dust grains at both $250\,\mu\text{m}$ and $89\,\mu\text{m}$ due to the inefficient alignment of VLGs. In contrast, SPM grains with high $N_{\text{cl}} = 10^4$ produce the change of polarization pattern from $\mathbf{P} \perp \mathbf{B}$ at $250\,\mu\text{m}$ to $\mathbf{P} \parallel \mathbf{B}$ at $89\,\mu\text{m}$ due to the change of the polarization mechanism.

Indeed, the polarization mechanism behind the polarization pattern produced by PM grains is different between model Realistic-rIA (due to dichroic extinction by aligned VLGs) and model Realistic-wIA (due to dichroic emission of micron-sized

aligned grains). Such a different polarization mechanism is attributed to the stronger reduced extinction efficiency of VLGs with wrong IA.

8.2 Intensity-dependent Polarization Degree

The upper panels of Figure 15 show the effect of iron inclusions on the mean variation of $p(\%)$ with I/I_{\max} calculated at $250\,\mu\text{m}$ for model Realistic-rIA (left panel) and Realistic-wIA (right panel). The result from model Ideal is plotted by the black dashed line for comparison. In the model Ideal, the polarization degree decreases from $p \sim 30\%$ from $d_{\text{proj}} \geq 1000$ au to $p \sim 8\%$ in the center as a result of the dichroic extinction by aligned VLGs. For model Realistic-rIA (left panel) and Realistic-wIA (right panel), p also decreases with increasing I/I_{\max} , but with a steeper slope than model Ideal due to the additional effect from the inefficient internal and external alignment of grains with \mathbf{B} (for SPM grains) or the loss of grain alignment (for PM grains) in the central region. For example, the polarization degree produced by SPM grains with $N_{\text{cl}} = 10^4$ reduces from $p \sim 30\%$ from $d_{\text{proj}} \geq 1000$ au to $p \sim 1\%$ in the center. SPM with lower N_{cl} and PM grains produce lower p , typically with $p \sim 3 - 20\%$ in the envelope and $p \ll 1\%$ (for PM) and $p \sim 1\%$ (for SPM). And similar to Figure 12, the polarization fraction produced by model Realistic-wIA is smaller than model Realistic-rIA. One also will obtain the valley-polarization hole with $p < 1\%$ in the transition distance between the envelope with high $p(\%)$ (and $\mathbf{P} \perp \mathbf{B}$) and the central region with low p (and $\mathbf{P} \parallel \mathbf{B}$) resulted from the cancelling effect of polarized emission from aligned dust grains with right and wrong IA.

One interesting feature obtained at $250\,\mu\text{m}$ is the slight rise of $p(250\,\mu\text{m})$ with increasing I/I_{\max} at $d_{\text{proj}} < 1000$ au for SPM grains with low $N_{\text{cl}} < 10^3$. This feature arises from the strong emission of grains with efficient IA near the protostar (Figure 6), which corresponds to the polarization pattern with $\mathbf{P} \perp \mathbf{B}$ in the inner 1000 au region in Figures 13 and 14.

The lower panels of Figure 15 show the similar results as the upper panels but at $89\,\mu\text{m}$. The $p - I/I_{\max}$ relationship becomes more complicated due to the joint polarization mechanism between dichroic emission and dichroic extinction by aligned dust grains. In detail, for model Ideal (see the black dashed line), the polarization degree is constant at $p \sim 8\%$ at $d_{\text{proj}} > 10000$ au, then rises to the peak of $p \sim 20\%$ at $d_{\text{proj}} \sim 5000$ au, decreases to $p \sim 10\%$ at $d_{\text{proj}} \sim 1000$ au, and rises again to $p \sim 8\%$ in the center. The first rise of p in the envelope is due to the high emission of warm grains at short wavelengths (in the envelope, polarization by dichroic emission is still the main source of polarization due to low gas density). The following decrease of p with increasing intensity arises from the extinction by aligned VLGs. And the rise of p from $d_{\text{proj}} \leq 500$ au toward the center is due to the increased efficiency of polarization by dichroic extinction in dense regions around the protostar.

For the realistic model of grain alignment (solid lines), the polarization degree generally follows the similar complex dependence with intensity as model Ideal, but with lower $p \sim 1 - 10\%$ due to the inefficient grain alignment in dense environments. However, except the case of SPM grains with high $N_{\text{cl}} = 10^4$ that the variation of p with I/I_{\max} is controlled by the joint effect of polarization by dichroic emission and dichroic extinction, the decrease and increase of p for SPM with low $N_{\text{cl}} \leq 10^3$ are attributed to the change in IA efficiency of the emission source, from efficient IA to inefficient IA by slow internal relaxation in the envelope and the opposite trend for grains in the central region.

9 EFFECT OF IRON INCLUSIONS ON POLARIZATION SPECTRUM

Lastly, we study the effect of iron inclusions on the wavelength-dependent polarization degree $p(\lambda)$ (i.e., polarization spectrum), from $89\,\mu\text{m}$ to $2\,\text{mm}$. The results calculated in the central region at $d_{\text{proj}} = 200$ au are shown in the upper panels of Figure 16, and the results in the envelope at $d_{\text{proj}} = 12000$ au are shown in the lower panels. The beam size is 120 au in both cases. The left column shows the results for model Realistic-rIA and the right column is for model Realistic-wIA. The polarization curve for the ideal case is plotted by the black dashed line for comparison.

In the ideal case, the polarization degree calculated at $d_{\text{proj}} = 200$ au decreases continuously from $p > 30\%$ at $2\,\text{mm}$ to $p \sim 1\%$ at $\lambda \sim 100\,\mu\text{m}$ due to the increased dichroic extinction by aligned VLGs at short wavelengths. At $\lambda < 100\,\mu\text{m}$, dichroic extinction by aligned VLGs becomes the main source of polarization, inducing the increase of $p(\%)$ with decreasing wavelengths.

For our realistic model of grain alignment, the polarization degree calculated at $d_{\text{proj}} = 200$ au also decreases then increases with decreasing wavelengths from $2\,\text{mm}$ to $89\,\mu\text{m}$. The polarization degree produced by SPM grains with larger N_{cl} is higher, but it is always smaller than model Ideal with $p \leq 10\%$. However, for SPM with high $N_{\text{cl}} = 10^4$, the curvature of the polarization curve is controlled by the joint action of polarization by dichroic emission (at $\lambda > 200$) and dichroic extinction (at $\lambda < 200\,\mu\text{m}$) as model Ideal. For SPM with lower $N_{\text{cl}} \leq 10^3$, the decrease and increase of p with decreasing λ is due to the change in IA of the polarized emission source, from grains with inefficient IA at $\lambda > 600\,\mu\text{m}$ to grains with efficient IA at $\lambda < 600\,\mu\text{m}$. If grains with slow internal relaxation have wrong IA (upper right panel), the V-shape of the polarization curve is clearer corresponding to the polarization flipping in the central region from $\mathbf{P} \parallel \mathbf{B}$ at $870\,\mu\text{m}$ (Figure 11, upper center panel) and $2\,\text{mm}$ (Appendix D, Figure D2, lower center panel) to $\mathbf{P} \perp \mathbf{B}$ at $\leq 450\,\mu\text{m}$ (Figure 11, lower center panel and Figure 14). The valley-polarization hole on $p(\lambda)$ caused by the change in IA of the emission source appears at optically thin wavelengths $\lambda \sim 400 - 600\,\mu\text{m}$, while the valley-polarization hole caused by the change of the polarization mechanism appears at optically thick wavelengths of $\lambda < 300\,\mu\text{m}$.

Toward the envelope (lower panels), the polarization degree produced by both model Ideal, Realistic-rIA, and Realistic-wIA just slightly decreases with decreasing wavelengths as a result of the weak emission of cold dust grains at short wavelengths. The polarization degree obtained in the envelope is generally higher than one in the central region (upper panels) because of increasing grain alignment efficiency by the MRAT mechanism with decreasing gas density. SPM grains with higher N_{cl} produces higher $p(\%)$, typically with $p \sim 1 - 10\%$ in the envelope for $N_{\text{cl}} \leq 10^3$ and $p \sim 10 - 45\%$ for $N_{\text{cl}} = 10^4$.

10 DISCUSSION

10.1 Effects of Iron Inclusions on Grain Alignment in Protostellar Cores

The alignment of dust grains with \mathbf{B} (i.e., magnetic alignment) induces the polarization of thermal dust emission and background starlight. Dust polarization is a powerful tool for studying magnetic fields in astrophysics and understanding the role of \mathbf{B} -fields in star and planet formation. However, grain alignment (both internal and external) depends on the local conditions and grain properties. In the diffuse ISM and MCs, PM grains can have efficient internal align-

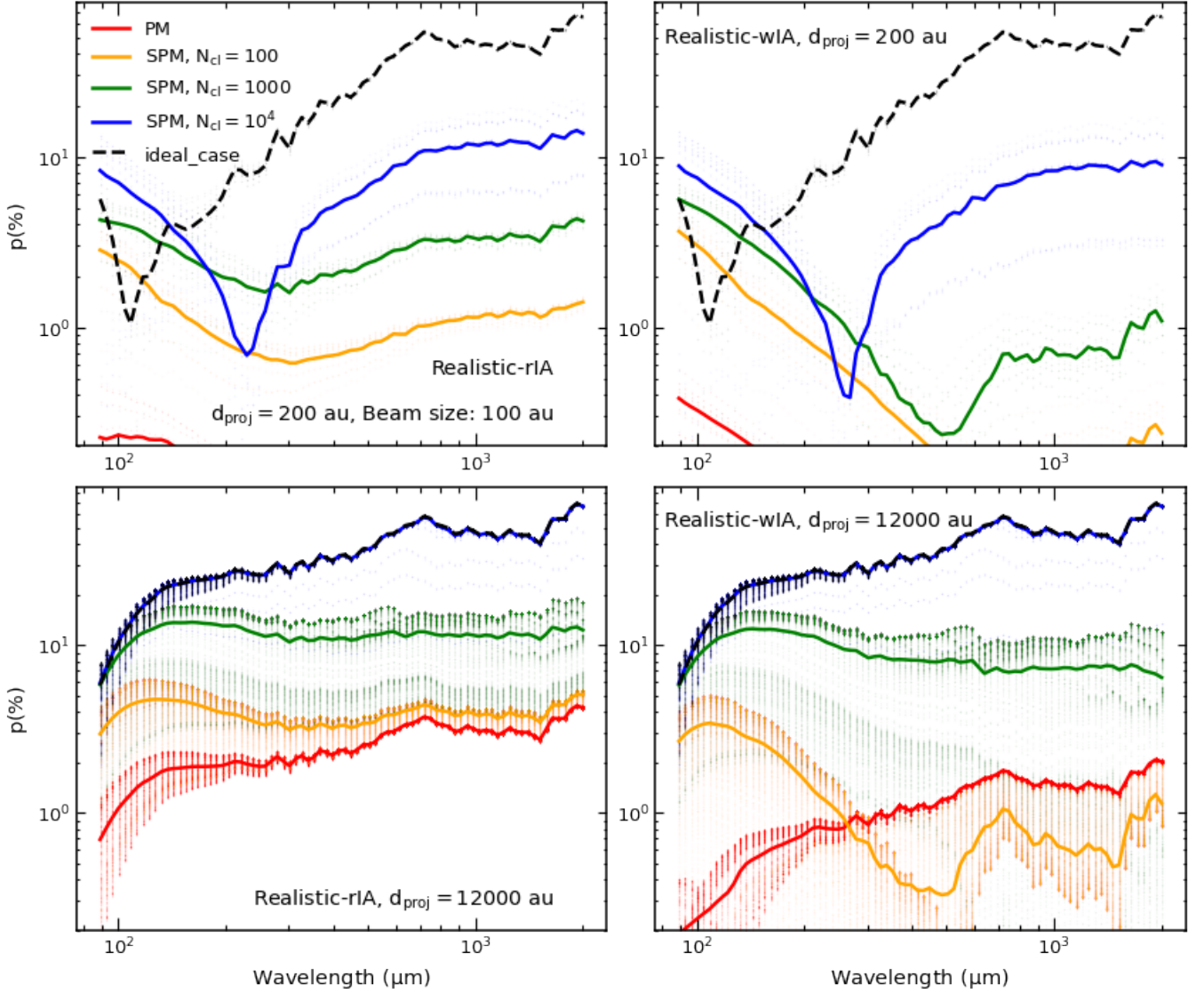


Figure 16. Effect of iron inclusions on the variation of p from $89 \mu\text{m}$ to 2 mm at the projected distance to the protostar of $d_{\text{proj}} = 200 \text{ au}$ (upper panels) and $d_{\text{proj}} = 12000 \text{ au}$ (lower panels) for model Realistic-rIA (left column) and Realistic-wIA (right column). At $d_{\text{proj}} = 200 \text{ au}$, p produced by model Ideal (black dashed line) and our models for SPM grains with $N_{\text{cl}} = 10^4$ decreases continuously from 2 mm to $\lambda \sim 100 - 200 \mu\text{m}$ then rises toward $\lambda = 89 \mu\text{m}$ due to the increased polarization by dichroic extinction. SPM grains with low $N_{\text{cl}} = 100$ also produce the decrease and increase of p (%) with decreasing wavelengths, but it is due to the enhanced emission of micron-sized grains with efficient IA at shorter wavelengths. At $d_{\text{proj}} = 12000 \text{ au}$, p (%) slightly decreases with decreasing λ due to the weak emission of cold dust grains at shorter wavelengths.

ment (IA) with the grain longest axis perpendicular to its angular momentum due to fast internal relaxation (Lazarian 2007; Hoang 2022). Moreover, the grain angular momentum can be efficiently aligned with \mathbf{B} by RATs due to the fast Larmor precession compared to the grain randomization by gas collisions (Hoang & Lazarian 2014; Hoang 2022). Thus, thermal dust polarization is always perpendicular to \mathbf{B} (see Tram & Hoang 2022 for a review). The existence of iron clusters (SPM) embedded in dust grains can enhance the degree of RAT alignment due to the joint effect of enhanced magnetic relaxation and RATs (a mechanism called MRAT), resulting in perfect grain alignment (Hoang & Lazarian 2016b). Consequently, dust polarization is a robust tool for tracing \mathbf{B} -fields in the diffuse ISM and MCs.

In dense environments as starless cores, the RAT alignment ef-

ficiency is significantly reduced due to the strong attenuation of ISRF by dust extinction and stronger gas randomization (Hoang et al. 2021). In protostellar cores with an embedded protostar, dust grains near the protostar are predicted to be more efficiently aligned with \mathbf{B} due to the contribution of protostellar radiation (Hoang et al. 2021). However, the gas randomization is also enhanced due to the high gas density, which can significantly suppress the alignment of grains with magnetic fields, as shown in Hoang (2022). Thus, the pressing question is whether dust polarization can reliably trace \mathbf{B} -fields in protostellar environments (Hoang & Lazarian 2016b; Yang 2021).

Using the RAT paradigm in which grains can be aligned at low-J and high-J attractors, numerical calculations by Hoang et al. (2022) show the crucial importance of iron inclusions on both internal and external alignment of grains with \mathbf{B} in protostellar environments.

Specifically, the authors show that PM grains cannot be aligned with \mathbf{B} , and only SPM grains can have the magnetic alignment due to the enhanced Larmor precession. Iron inclusions also help grains that rotate suprathermally have fast internal relaxation (then efficient IA) due to enhanced Barnett relaxation. However, they do not help grains at low- J attractors due to their slow rotation.

Our detailed modeling of grain alignment using the RAT paradigm with radiative transfer with POLARIS confirms the numerical calculations of grain alignment in protostellar cores from previous studies (Hoang (2022); Hoang et al. (2022)). Particularly, in Section 5.2, we show that PM grains only can be aligned with \mathbf{B} in the protostellar envelope due to the reduced gas randomization, but most of them have slow internal relaxation at both low and high- J attractors. In contrast, SPM grains of micron-sizes can have the magnetic alignment and a fraction of them can have efficient IA in the dense central region with $n_{\text{H}} > 10^7 \text{ cm}^{-3}$ due to the enhanced Barnett relaxation and Larmor precession by iron inclusions (Figures 5 and the left panel of 6). However, we found that even with a high level of iron inclusions, micron-sized grains aligned with \mathbf{B} at low- J attractors cannot have the fast internal relaxation due to its thermal rotation (the right panel of Figure 6). Consequently, they may align with their longest axis perpendicular or parallel with \mathbf{B} , which causes the ambiguity on the orientation between \mathbf{P} and \mathbf{B} .

The external alignment between SPM grains with \mathbf{B} can be enhanced by the joint effect of RATs and enhanced magnetic relaxation, as predicted by the MRAT mechanism (Hoang & Lazarian 2016b). We found that this effect is very efficient in increasing the external alignment of SPM grains with a high fraction of iron inclusions in the protostellar envelope. It allows all SPM grains to have perfect alignment ($f_{\text{high-}J} = 1$) with \mathbf{B} , regardless of the difference on the grain sizes and their orientation in the envelope. However, in the central region, the efficiency of magnetic relaxation is negligible due to the reduction of the grain magnetic susceptibility with dust temperature in hot environments near the protostar (Figure 7) and the enhancement of gas randomization. As a result, both PM and SPM grains near the protostar are only aligned with \mathbf{B} by RATs, with the fraction of grains at high- J attractors varying from 0.25 – 0.7, depending on the grain shape, grain size, etc (Herranen et al. 2021).

10.2 Dependence of dust polarization pattern at optically thin wavelengths on Iron inclusions

As discussed in Section 10.1, large (micron-sized) grains in protostellar cores tend to have inefficient IA due to slow internal relaxation, even when they rotate suprathermally at high- J attractors. Different from grains with fast internal relaxation that always have right IA ($\hat{\mathbf{a}}_1 \parallel \mathbf{J}$), the slow internal relaxation produces the uncertainty in the alignment direction between $\hat{\mathbf{a}}_1$ and \mathbf{J} . Hoang & Lazarian (2009) showed that grains with slow internal relaxation can still have right IA at high- J attractors due to RATs, but grains at low- J attractors may have right IA or wrong IA ($\hat{\mathbf{a}}_1 \perp \mathbf{J}$). A detailed study for the conditions for the right or wrong IA is not yet available.

In Section 6, we show that if grains with slow internal relaxation have right IA (model Realistic-rIA), the polarization patterns are always uniform with $\mathbf{P} \perp \mathbf{B}$ in the entire protostellar core from mm to sub-mm wavelengths, regardless of the grain magnetic properties (Figures 8, 9, and D1). In contrast, if grains with slow internal relaxation have wrong IA (model Realistic-wIA), the polarization patterns will depend on the magnetic properties of grains. Particularly, PM grains produce the uniform polarization pattern with $\mathbf{P} \parallel \mathbf{B}$ at both mm and sub-mm. SPM grains with a moderate level of iron inclusions produce the uniform pattern with $\mathbf{P} \parallel \mathbf{B}$ at 2mm (Figure

D2) and 870 μm (Figure 10), but the complex ones at 450 μm with the polarization pattern changing from $\mathbf{P} \perp \mathbf{B}$ to $\mathbf{P} \parallel \mathbf{B}$ from the outer to the inner envelope (Figure 10 and \mathbf{P} changing from $\mathbf{P} \parallel \mathbf{B}$ to $\mathbf{P} \perp \mathbf{B}$ from the outer to the inner region of the central region (Figure 11). SPM grains with a high level of iron inclusions simply produce the uniform polarization pattern, with $\mathbf{P} \perp \mathbf{B}$ due to the efficient alignment of large grains by MRAT alignment (Figures 10, 11, and D2).

In summary, in contrast to the coherent polarization pattern with $\mathbf{P} \perp \mathbf{B}$ at sub-mm/mm observed from the diffuse ISM and MCs, the polarization patterns observed toward protostellar cores are diverse due to the existence of large grains with slow internal relaxation. It strongly depends on the magnetic properties of grains and the nature of internal alignment between $\hat{\mathbf{a}}_1$ and \mathbf{J} . This complicated feature causes the confusion on the orientation of \mathbf{P} produced by thermal emission from magnetically aligned dust grains, especially when the level of iron locked inside dust grains is unknown. However, we found that the abundance of embedded iron is revealed through the polarization degree, which will be discussed in the next section. It gives us a hint for constraining the orientation between \mathbf{P} and \mathbf{B} , and this issue will be discussed in detail in Section 10.9.

10.3 Dependence of polarization degree on iron inclusions and maximum grain size

In Section 7, we showed that the calculated polarization degree $p(\%)$ is higher for higher values of N_{cl} , assuming a constant volume filling factor of iron clusters, ϕ_{sp} . We found that in particularly, PM grains only can produce low $p \sim 1\%$ in the envelope and negligible polarization signal in the inner 1000 au region where grains are not aligned with \mathbf{B} . In contrast, iron inclusions can lead VLGs to achieve perfect alignment in the envelope and produce the maximum polarization degree up to $p \sim 40\%$ here. However, they cannot strongly enhance RAT alignment in the central region due to the stronger gas randomization. As a result, the polarization degree decreases from the envelope toward the protostar. But in contrast to the negligible $p < 1\%$ in the central region produced by PM grains, SPM grains produce $p > 1\%$ because micron-sized grains can be aligned with \mathbf{B} here. The dependence of p on iron inclusions are nearly similar for both model with and without grains with wrong IA.

In our modelling till now, we have fixed the volume filling factor of iron clusters $\phi_{\text{sp}} = 0.005$ that corresponds to 1.67% (Hoang & Lazarian 2016b) iron abundance present in the form of embedded iron clusters, and vary N_{cl} to describe different magnetic properties of grains. Indeed, Jenkins (2009) showed that $\sim 90\%$ of iron can be locked inside grains, that corresponds to $\phi_{\text{sp}} \sim 0.3$ if all iron are in the form of clusters. That means with a higher ϕ_{sp} , one only needs a small number of iron atoms per each cluster to achieve the high magnetic susceptibility that can drive most grains to be perfectly aligned with \mathbf{B} as our studied case with $N_{\text{cl}} = 10^4$ and $\phi_{\text{sp}} = 0.005$ (Equation 3).

To generalize the dependence of the polarization degree on the level of iron inclusions, which is described by a term $N_{\text{cl}}\phi_{\text{sp}}$, we adopt models Realistic-rIA-amax and Realistic-wIA-amax with different maximum grain sizes from $a_{\text{max}} = 5 \mu\text{m}$ to $a_{\text{max}} = 150 \mu\text{m}$ (Table 1) and plot the results in Figure 17. The left column shows the results calculated by model Realistic-rIA-amax, and the right column is for model Realistic-wIA-amax. The upper panels show the results calculated in the central region at $d_{\text{proj}} = 200 \text{ au}$, and the lower panels are for the envelope at $d_{\text{proj}} = 12000 \text{ au}$. The minimum $N_{\text{cl}}\phi_{\text{sp}} = 0.01$ corresponds to the magnetic susceptibility of PM

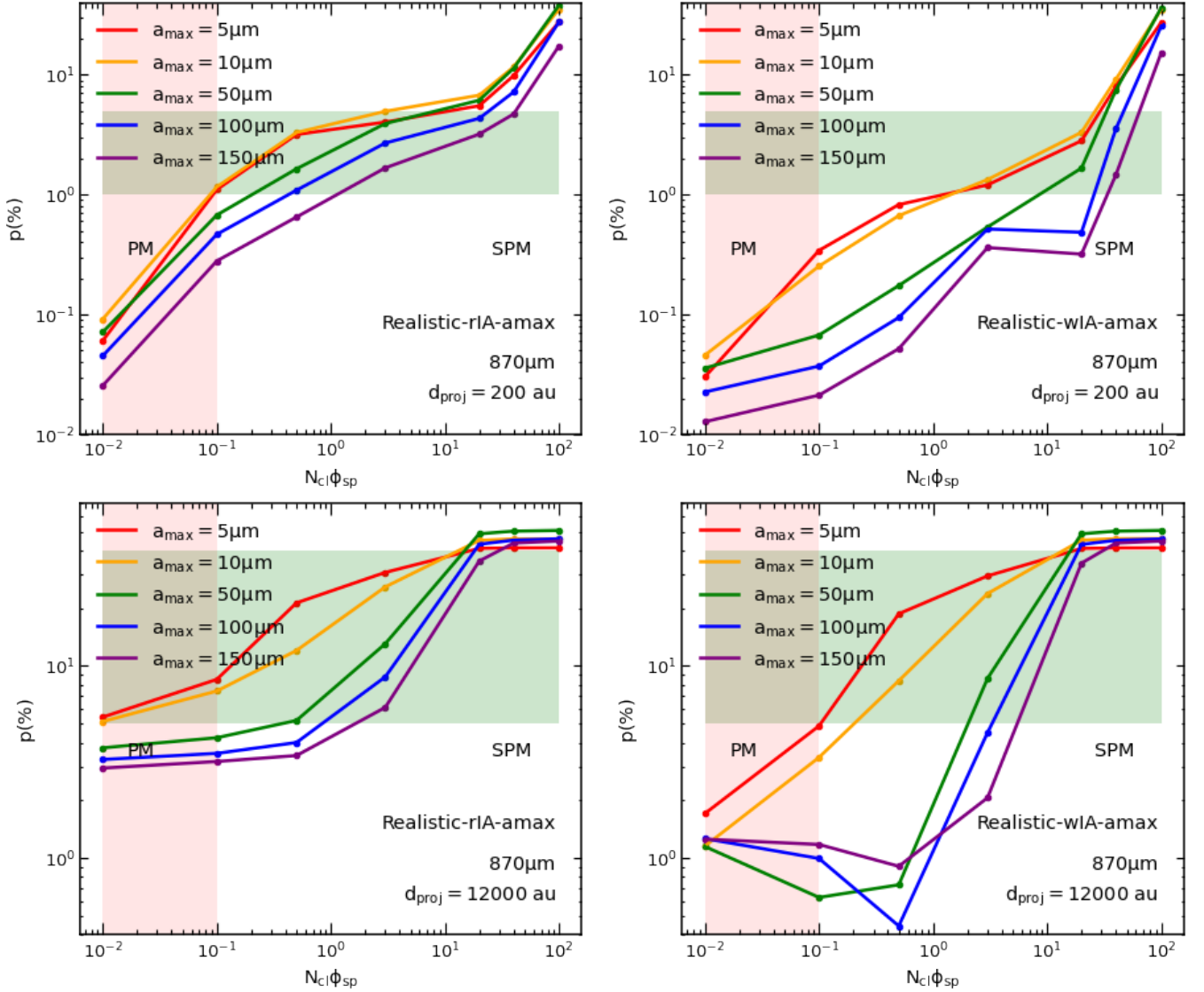


Figure 17. Dependence of p calculated at $d_{\text{proj}} = 200$ au (upper panels) and $d_{\text{proj}} = 12000$ au (lower panels) as the function of iron fractions locked inside dust grains $N_{\text{cl}}\phi_{\text{sp}}$ from model Realistic-rIA-amax (left column) and model Realistic-wIA-amax (right column), with different grain size from $a_{\text{max}} = 5 \mu\text{m}$ to $a_{\text{max}} = 150 \mu\text{m}$. The red shaded area marks the value produced by PM grains, and the green shaded area marks the polarization degree observed toward protostellar cores by ALMA. The polarization degree increases with increasing the levels of iron inclusions locked inside grains, and one will obtain higher $p(\%)$ if grains with slow internal relaxation have right IA. The high amount of iron is required to reproduce observed polarization fraction of $p > 1\%$ in the central region and $p \sim 5 - 40\%$ in the envelope of Class 0/I YSOs.

(Equation 1), which is marked by the red box. The maximum value $N_{\text{cl}}\phi_{\text{sp}} = 100$ is for SPM grains with the magnetic susceptibility enhanced by a factor of $\sim 10^4$ compared to PM. One can clearly see that grains with higher level of iron inclusions radiate stronger polarized thermal emission with higher $p(\%)$. In the central region, iron inclusions help grains to be stably aligned with \mathbf{B} and produce the detected level of polarization of $p > 1\%$. In the envelope, high levels of iron inclusions lead grains to achieve perfect alignment with \mathbf{B} and produce very high polarization up to $p \sim 40\%$, as predicted by the MRAT mechanism (Hoang & Lazarian 2016b). With the same amount of iron inclusions, the model with grains having wrong IA produce lower p than model without grains having wrong IA as a result of the reduced dust polarization due to the co-existence of grains with right and wrong IA.

Figure 18 shows the variation of $p(\%)$ with a_{max} calculated by the model Realistic-rIA-amax (left column) and model Realistic-wIA-amax (right column) at $d_{\text{proj}} = 200$ au (upper panels) and $d_{\text{proj}} = 12000$ au (lower panels). For a fixed level of iron inclusions, the polarization degree decreases with increasing maximum grain size because large grains tend to have inefficient alignment with \mathbf{B} -fields in dense environments. Thus, higher levels of iron inclusions are required to present inside micron-sized grains to help them efficiently align with \mathbf{B} and produce the detected fraction of polarization of $p > 1\%$ in both the central region and the envelope. For example, with $a_{\text{max}} = 10 \mu\text{m}$, grains need $N_{\text{cl}}\phi_{\text{sp}} \sim 3$ to produce $p \sim 1\%$ at $d_{\text{proj}} = 200$ au, but if they grow to $a_{\text{max}} = 100 \mu\text{m}$, the level of iron inclusions must increase to $N_{\text{cl}}\phi_{\text{sp}} \sim 30$ to produce $p \sim 1\%$ in the central region. The value of $N_{\text{cl}}\phi_{\text{sp}}$ must increase

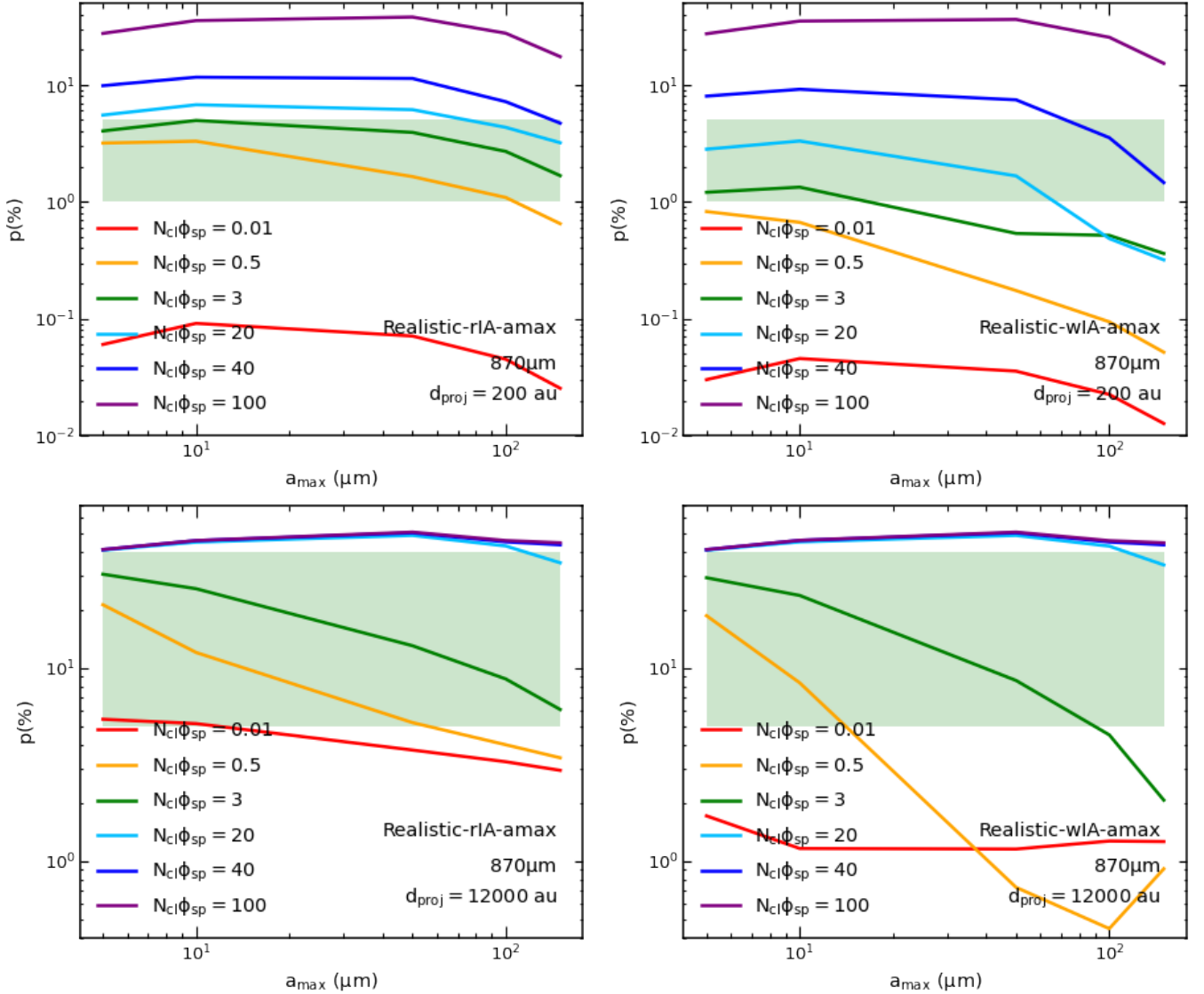


Figure 18. Similar as Figure 17 but for the variation of $p(\%)$ with maximum grain size a_{\max} . The presence of large grains generally reduces the fraction of polarization. Therefore, they must contain a high level of iron inclusions in order to produce the detected level of $p \geq 1\%$ in the central region and $p \geq 10\%$ in the envelope.

more to produce $p \sim 1\%$ if grains with slow internal relaxation have wrong IA.

Besides the fraction of iron locked inside grains, magnetic field strength also affects on the alignment of grains with \mathbf{B} . The stronger magnetic field strength enhances the Larmor precession and the magnetic relaxation (Section 2), allowing more large grains to be efficiently aligned with \mathbf{B} in the densest central region. In our modeling, we have adopted the uniform $B = 134 \mu\text{G}$ in the entire protostellar core to emphasize the effects of grain alignment physics on synthetic dust polarization. However, the magnetic field strength is amplified with increasing gas density inward of the protostar as a result of the freezing of B-fields. Observations toward Class 0/I YSO L1448 IRS 2 by Kwon et al. (2019) reveal the highly order hourglass-shape magnetic field in the protostellar system, and they estimated the magnetic field strength in the inner 100 au region of $B \sim 600 \mu\text{G}$. Myers & Basu (2021) also found the positive correlation between the magnetic field strength measured by the David Chandrasekhar Fermi (DCF) method (Chandrasekhar & Fermi 1953) and the gas density

of $B_{\text{pos}} \sim n_{\text{H}}^{0.66 \pm 0.05}$ in the sample of 17 low-mass prestellar and protostellar cores. To understand how the magnetic field strength affects the magnetic alignment in the densest central region, we increase the magnetic field strength in the central 1000 au region into $B = 1 \text{ mG}$ while keeping the same $B = 134 \mu\text{G}$ at $r > 1000 \text{ au}$, denoted as model Realistic-rIA-amax-B and Realistic-wIA-amax-B (Table 4). The variation of $p(\%)$ with $N_{\text{cl}}\phi_{\text{sp}}$ in the central region at $d_{\text{proj}} = 200 \text{ au}$ is shown in Figure 19.

The left panel of Figure 19 shows the results for model Realistic-rIA-amax-B and the right panel is for model Realistic-wIA-amax-B. Comparing to the upper panels of Figure 17, one gets higher $p(\%)$ for all values of $N_{\text{cl}}\phi_{\text{sp}}$. For low $N_{\text{cl}}\phi_{\text{sp}} < 20$, the difference is clearer as a result of the extend of the range of grain alignment to larger sizes, i.e., higher $a_{\text{max,JB}}^{\text{Lar}}$, due to the enhanced Larmor precession by stronger magnetic field strength. For high $N_{\text{cl}}\phi_{\text{sp}} > 20$ in which most large micron-sized grains are aligned with \mathbf{B} , the increase of $p(\%)$ is not clear because

the stronger \mathbf{B} -field strength cannot enhance the magnetic relaxation over the strong gas randomization here. It means that grains within few hundreds of au around the protostar are mainly aligned with \mathbf{B} by RATs (instead of MRAT alignment as grains with a high level of iron inclusions in the envelope).

10.4 Implications for the high polarization degree observed by ALMA toward protostellar envelopes

In dense environments such as protostellar cores, one usually expects to observe a much lower dust polarization degree than in the diffuse ISM due to the inefficient alignment of grains with magnetic fields, according to the RAT theory (Lazarian & Hoang 2007). However, SMA and ALMA observations toward Class 0/I YSOs reveal a high degree of dust polarization up to $p \sim 10 - 40\%$ in the envelope (Hull et al. 2014; Cox et al. 2018; Galametz et al. 2019), much higher than the maximum values of $p \sim 20\%$ observed in the diffuse ISM (Planck Collaboration et al. 2015). The polarization degree observed in the central region is low but still detectable of $p > 1\%$. Although the RAT alignment theory expects the rise of p toward the protostar due to increasing radiation field (Hoang et al. 2021), the reduction of polarization degree toward the central region is still possible if the randomization effect by gas-grain collisions is more effective than the grain alignment by RATs. However, the numerical modeling with POLARIS by Le Gouellec et al. (2020) showed that the RAT alignment mechanism implemented in the current version of POLARIS produces a much lower polarization degree than observations toward both low and high-mass protostars by ALMA. They found that ALMA data only can be successfully reproduced by the model in which all grains are perfectly aligned with \mathbf{B} .

Theoretical studies in Hoang (2022) and Hoang et al. (2022) and our detailed modelling of grain alignment by the MRAT mechanism in Section 5.2 clearly show that large micron-sized grains can achieve the efficient magnetic alignment in protostellar environments if they contain a high level of iron inclusions. This effect is more prominent in the envelope, where VLGs can have perfect alignment and produce the high polarization degree up to $p \sim 40\%$. Thus, the detection of high $p \sim 40\%$ toward Class 0/I YSOs by ALMA and the implication of perfect grain alignment by Le Gouellec et al. (2020) can be successfully reproduced by the MRAT mechanism. Moreover, this finding indicates that dust grains in protostellar environments must contain iron inclusions.

10.5 Toward constraining iron abundance embedded in dust using dust polarization

Iron is among the most abundant element in the Universe. Observations reveal that more than 90% of iron abundance are missing from the gas (Jenkins 2009), which implies that iron must be dominantly present inside dust grains (Dwek 2016). Yet, observational study of iron in dust is rather difficult. Hoang & Lazarian (2016b) first showed that one can constrain the level of iron in dust using sub(mm) polarization data. Lazarian & Hoang (2019) obtained the lower and upper limit for magnetic susceptibility using the ALMA polarization patterns toward protostellar disks.

A synthetic modeling of dust polarization by Lam et al. (2021), which assumes the perfect alignment for all grains with Larmor precession faster than the gas randomization, found that the magnetic susceptibility of grains of $a \geq 1 \mu\text{m}$ must be increased by a factor of 20 compared to PM to reproduce $p \geq 1\%$ in the inner 100 au of a dozen of Class 0/I YSOs observed by ALMA (Cox et al.

2018). Moreover, a synthetic modelling with POLARIS by Valdivia et al. (2019), which does not consider the grain magnetic properties, concluded that grains must grow to $a \sim 10 - 50 \mu\text{m}$ to reproduce $p \geq 1\%$ observed in the samples of Class 0 YSOs by Hull et al. (2014). Recently, numerical studies of grain alignment in protostellar cores and protoplanetary disks by Hoang (2022) and Hoang et al. (2022) showed that large micron-sized grains must contain the high level of iron inclusions to be efficiently aligned with \mathbf{B} in such dense environments and produce polarized thermal emission.

In Section 10.3, we show the dependence of p with the level of iron inclusions $N_{\text{cl}}\phi_{\text{sp}}$ in Figure 17. The green shaded area in the left and right panel of the figure shows the polarization degree observed by ALMA, JVLA, SMA, etc, toward Class 0/I YSOs (Hull et al. 2014, Ko et al. 2020, Le Gouellec et al. 2020, Cox et al. 2018). It is very clear that grains must be SPM with the magnetic susceptibility enhanced by a factor of ≥ 5 compared with PM grains to reproduce $p > 1\%$ in the central region and $p \sim 5 - 40\%$ in the envelope. Using our modeling results of polarization degree and observed polarization, we can infer again the level of iron inclusions locked inside dust grains. For example, to reproduce $p \sim 1\%$ at $d_{\text{proj}} = 200$ au with $a_{\text{max}} = 10 \mu\text{m}$, one needs $N_{\text{cl}}\phi_{\text{sp}} \geq 1$. It corresponds to $N_{\text{cl}} = 200$ if $\phi_{\text{sp}} = 0.005$ (or 1.67% of iron abundance locked inside grains under the form of cluster), or $N_{\text{cl}} = 10$ if $\phi_{\text{sp}} = 0.1$ (or 30% of iron abundance locked inside grains). If grains grow to VLGs with $a_{\text{max}} = 100 \mu\text{m}$, they need more embedded iron of $N_{\text{cl}}\phi_{\text{sp}} \geq 20$ to be aligned with \mathbf{B} in the central region. It corresponds to $N_{\text{cl}} = 4000$ and $N_{\text{cl}} = 20$ if $\phi_{\text{sp}} = 0.005$ and $\phi_{\text{sp}} = 0.1$, respectively.

Note that the main goal of our present study is to demonstrate the key effects of grain alignment physics on synthetic dust polarization in protostellar environments, thus we adopt the simple spherical symmetry for the protostellar core and uniform B-fields along the z direction. We also perform the synthetic modeling assuming that the magnetic field only lies in the plane of the sky to understand how the grain alignment efficiency affects properties of polarized dust emission. In realistic situations, magnetic fields in protostellar cores usually have the hourglass shape driven by gravitational collapse toward protostars, which are theoretically predicted by Fiedler & Mouschovias (1993), Allen et al. (2003), and widely confirmed by observations, e.g., Girart et al. (2006), Rao et al. (2009), Hull et al. (2014). The complex \mathbf{B} -field structure along the line of sight combined with the tangling of \mathbf{B} -fields by turbulence results in a smaller polarization degree than obtained by our modeling with uniform \mathbf{B} -fields. In addition, the gas density in the central region of our model is $n_{\text{H}} = 10^7 \text{ cm}^{-3}$, which is much lower than the measured gas density in protostellar disks of Class 0/I YSOs of $n_{\text{H}} \sim 10^8 - 10^9 \text{ cm}^{-3}$ (e.g., Sandell et al. 1991, Takahashi et al. 2012) and the gas density from MHD simulations of collapsing protostellar cores (Lam et al. 2019). The magnetic field strength is also correlated with the gas density instead of being uniform as our assumption. Thus, the higher gas density will decrease the efficiency of grain alignment, but higher B-field strength would help to enhance MRAT alignment efficiency in the central region. Detailed synthetic observations of non-ideal MHD simulations of collapsing protostellar cores are required to accurately understand how grains around protostars get aligned with \mathbf{B} and how much iron inclusions are needed to reproduce the observed polarization level of $p > 1\%$ from ALMA, JVLA, SMA, etc, observations. Such a study also allows us to better interpret observational data and clarify the role of B-fields the star formation process. We will present the results from this study in our followup paper.

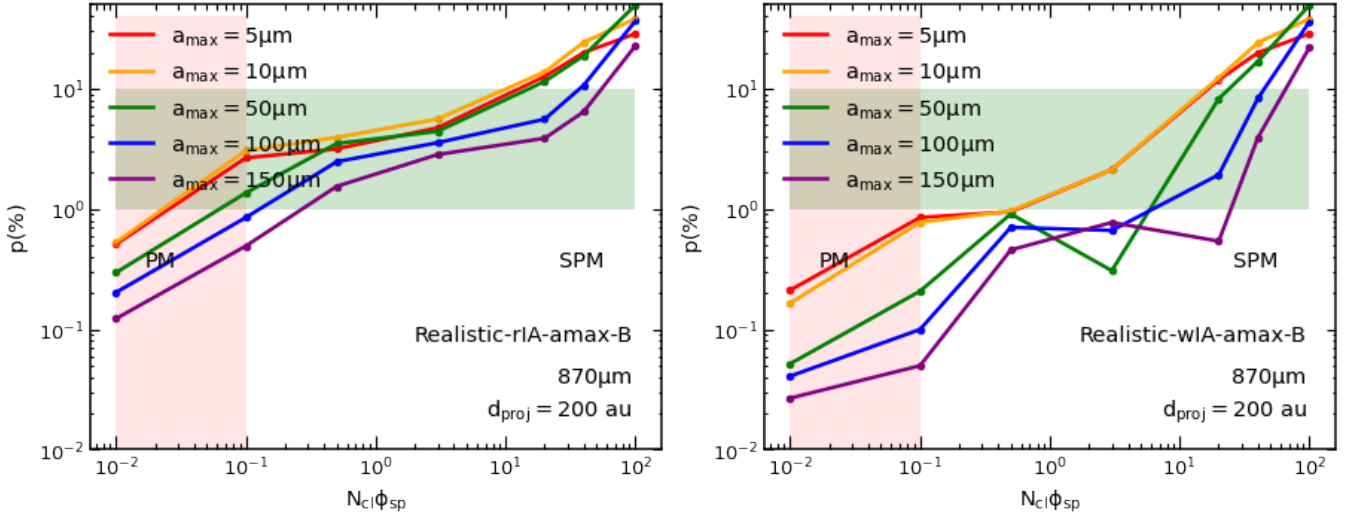


Figure 19. Dependence of p with $N_{\text{cl}}\phi_{\text{sp}}$ for different values of a_{max} for models with stronger \mathbf{B} -fields in the central region Realistic-rIA- a_{max} -B (left column) and model Realistic-wIA- a_{max} -B (right column) calculated in the central region at $d_{\text{proj}} = 200$ au. Similar as the left panel of Figure 17, only SPM grains can reproduce the observed degree of polarization of $p > 1\%$, and higher iron fractions are required to align grains with \mathbf{B} if grains grow to VLGs. The polarization degree increases with increasing \mathbf{B} -field strength for low $N_{\text{cl}}\phi_{\text{sp}} \leq 20$ as a result of the enhanced Larmor precession. However, stronger \mathbf{B} -fields does not help to increase $p(\%)$ for grains with high $N_{\text{cl}}\phi_{\text{sp}}$ because the MRAT alignment is not the major grain alignment mechanism in the dense central region.

10.6 Effect of iron inclusions on polarization by dichroic extinction

In protostellar environments, the polarization by dichroic extinction is expected to be activated at sub-mm (Brauer et al. 2016) due to the presence of VLGs (Kwon et al. 2009, Testi et al. 2014, Miotello et al. 2014). VLGs can strongly attenuate polarized thermal emission at sub-mm, and this feature is suggested to be the origin of the polarization hole (Brauer et al. 2016, Liu et al. 2016, Ko et al. 2020, Liu 2021). Polarization by dichroic extinction is suggested to become the main source of polarization at optically thick wavelengths and cause the 90° flipping of the polarization pattern between mm and sub-mm wavelengths observed in IRAS4A (Ko et al. 2020) and OMC-3/MMS 6 (Liu 2021).

However, the study by Brauer et al. (2016) and the discussion in Ko et al. (2020) and Liu (2021) assumed that VLGs are efficiently aligned with \mathbf{B} . In Section 5.2, we show that this situation only can happen if grains are SPM with a high level of iron inclusions (fourth column of Figures 13 and 14). If it is not the case, VLGs are not efficiently aligned with \mathbf{B} , then, they less attenuate polarized thermal emission and cannot become the main source of polarization at optically thick wavelengths. Thus, one will not obtain any change of the polarization pattern between optically thin and optically thick wavelengths (Figures 13 and 14).

Furthermore, even if VLGs are efficiently aligned \mathbf{B} in protostellar environments, the extinction by aligned VLGs is not efficient in reducing polarized thermal emission in the central region compared to the effect of the inefficient grain alignment on the polarization degree (Section 8.2). Brauer et al. (2016) showed that the efficiency of polarization by dichroic extinction increases with increasing gas density. But the high gas density makes the magnetic alignment of VLGs more difficult, which mimics the effect of polarization by dichroic extinction in dense environments. Thus, simply attributing the extinction by aligned dust grains to any anomalous features observed

in dense environments without examining in detail the level of iron inclusions may cause the wrong interpretation of dust polarization.

10.7 Implications for the origin of polarization holes and the role of iron inclusions

Polarization observations toward Class 0 YSOs usually report the reduction of the polarization degree at sub-mm/mm wavelengths toward the central region of protostellar cores. For example, the existence of polarization hole is widely reported on 30 star-forming cores observed at 1.3mm by CARMA (Hull et al. 2014), 10 Class 0 YSOs observed at $870\ \mu\text{m}$ by ALMA (Cox et al. 2018), 6 objects in Bok globules observed at $870\ \mu\text{m}$ by SCUBA (Henning et al. 2001, Wolf et al. 2003). Multi-wavelength observations toward NGC 1333 IRAS4A, OMC-3/MMS 6, and NGC 2071 also show the similar feature from sub-mm to mm wavelengths (Ko et al. 2020, Liu 2021, Fanciullo et al. 2022).

Many scenarios are proposed to explain the polarization hole toward protostars, including the inefficient grain alignment by RATs (Hoang & Lazarian 2016b; Hoang et al. 2021), the dichroic extinction by aligned VLGs (Brauer et al. 2016), or the inclination angle and the geometrical effect of magnetic fields due to the self-collapse protostellar cores (Tazaki et al. 2017).

Polarization by dichroic extinction suggested by Brauer et al. (2016) is the promising explanation of the polarization hole. But as we discuss in Section 10.6, dichroic extinction by aligned grains only plays a minor role on reducing polarized thermal emission around protostars. We show that the reduced internal alignment and external alignment by the MRAT mechanism in the dense central region is the more effective mechanism producing the polarization hole in protostellar cores (Section 8.2). Furthermore, this mechanism does not require the presence of aligned VLGs in very dense environments. Thus, we suggest that this scenario as a main mechanism for explaining the origin of polarization holes in different class 0/I YSOs.

We note that the inefficient grain alignment in dense environments depends on the magnetic properties of grains. In particular, the polarization hole will be due to the loss of grain alignment in dense central region if grains are PM. In contrast, for SPM grains, it is because of the increase of grains with inefficient IA by slow internal relaxation and the reduced efficiency of MRAT alignment with increasing gas randomization. Since the magnetic properties of grains can be inferred from the observed polarization degree (Section 10.5), one then can know in detail the behind mechanism which is responsible for the reduction of p toward the central region of protostellar cores.

10.8 On the 90° rotation of polarization vectors

Another interesting feature observed toward Class 0 YSOs is the change of the polarization pattern with wavelengths. Particularly, the polarization patterns in the inner 100 au region of Class 0 YSO NGC 1333 IRAS4A (Ko et al. 2020) and OMC-3/MMS (Liu 2021) change 90° from mm observed by JVLA to sub-mm observed by ALMA. Another case is the MC NGC2071 which shows the 90° difference of \mathbf{P} in the central region between 870 μm observed by JCMT and 158 μm and 214 μm observed by SOFIA.

Fanciullo et al. (2022) argued that the twist of the polarization pattern observed in NGC 2071 may be due to the presence of grains with wrong IA suggested by Hoang (2022). In Figure 10, we show that if SPM grains have a moderate level of iron inclusions and have wrong IA by slow internal relaxation, the polarization pattern at the outer boundary of the envelope can change from $\mathbf{P} \parallel \mathbf{B}$ at 870 μm (see also the map at mm in Figure D2) to $\mathbf{P} \perp \mathbf{B}$ at 450 μm due to the change in IA of the emission source. In our calculations, this feature happens at optically thin wavelengths. The flipping of \mathbf{P} between 214 μm and 870 μm observed in the MC NGC 2071 also appears in optically thin central region. Thus, we suppose that this anomalous feature be due to the change in IA of the emission source, in which JCMT and SOFIA measure polarized emission from large grains with wrong IA with $\mathbf{P} \parallel \mathbf{B}$ and from smaller grains with right IA with $\mathbf{P} \perp \mathbf{B}$, respectively. Indeed, the gas density and the maximum grain size of the MC NGC 2071 are different from our model adopted for the protostellar core. However, we expect the similar results for dense regions inside MCs because the inefficient IA is naturally produced if the gas randomization is stronger than the internal relaxation.

For the case of IRAS4A and OMC-3/MMS 6, Ko et al. (2020) and Liu (2021) found that the cores of two objects are optically thick at sub-mm measured by ALMA and optically thin at mm measured by JVLA. Therefore, they assign the polarization flipping in the inner 100 au region to the change of the polarization mechanism from dichroic emission to dichroic extinction. However, as we show in Section 8.1 and discuss in Section 10.6, the change of the polarization pattern from optically thin to optically thick wavelengths in protostellar environments only can happen if VLGs contain a very high level of iron inclusions (Figures 13 and 14). In our calculations, the inner 1000 au region becomes optically thick at 250 μm , and VLGs must have $N_{\text{cl}}\phi_{\text{sp}} = 50$ (~ 5000 larger than PM) to produce the polarization flipping between 250 μm and 89 μm . For IRAS4A and OMC-3/MMS 6, Ko et al. (2020) and Liu (2021) found that inner 100 au region becomes optically thick at ≤ 1 mm, indicating that these objects are very dense. Thus, to activate the effect of dichroic extinction at ≤ 1 mm, grains in IRAS4A and OMC-3/MMS 6 must have much higher iron inclusions than our studied case. However, the amount of iron locked inside grains still be constrained by the crystalline structure of grains (Yang 2021). Thus, one cannot increase amount of iron too much to make the scenario proposed by Ko et al. (2020) and Liu (2021) come true. In case that polarization by dichroic extinction

is not effective, we suppose that the change in IA of the emission source from inefficient IA at mm to efficient IA at sub-mm to be the reason of the 90° flipping of \mathbf{P} with wavelengths. However, IRAS4A and OMC-3/MMS 6 have higher luminosity and higher gas density (Sandell et al. 1991, Takahashi et al. 2012) than our studied parameters. The strong radiation field can allow more large grains near the source to be aligned with \mathbf{B} with efficient IA (Figure 6, left panel) and activate polarization by dichroic extinction at sub-mm. However, the strong radiation field also can disrupt large grains by Radiative Torque Disruption (RAT-D) mechanism proposed by Hoang et al. (2019) (Hoang et al. 2021). If it is the case, the polarization by dichroic extinction cannot cause the change of \mathbf{P} with wavelengths. The detail study of grain alignment by the MRAT mechanism and grain disruption by RAT-D around high-luminosity protostar is required to accurately figure out the physics behind the twist of the polarization pattern of IRAS4A and OMC-3/MMS 6.

One interesting feature is that if the change of the polarization pattern with wavelengths is caused by the change in IA of the emission, it implies that grains with slow internal relaxation in the studied objects have wrong IA. Until now, the detailed study about the dynamics of grains with slow internal relaxation is still missing. Thus, it is necessary to study basic properties and effects of environments on establishing the alignment direction of grains with slow internal relaxation. Knowing this information allows us to accurately model grain alignment in dense environments, which is the key for better analyzing dust polarization.

10.9 From polarization vectors to the magnetic field direction

Here we discuss the conditions for which the polarization vectors can be rotated by 90° to infer the magnetic field direction in dense environments. As discussed in Section 10.2, the orientation of \mathbf{P} with \mathbf{B} strongly depends on the level of iron locked inside grains and the internal alignment direction. Furthermore, multi-wavelength observations from mm to sub-mm should be done to accurately answer the question whether we should rotate \mathbf{P} by 90° or not to infer \mathbf{B} .

In particular, if the polarization pattern does not change from mm to sub-mm, it can be classified to three cases: SPM grains with the high level of iron inclusions, SPM grains with a moderate level of iron inclusions which have right IA with slow internal relaxation, and PM grains. For the first and second cases, grains always align with their longest axis perpendicular to \mathbf{B} and thus emit polarized thermal radiation with $\mathbf{P} \perp \mathbf{B}$. This case is accompanied by a high polarization degree of $p > 5\%$ in the envelope and $p > 1\%$ in the central region. With this case, we can confidently rotate \mathbf{P} by 90° to reconstruct \mathbf{B} -fields morphology on the plane of sky. For the last case, \mathbf{P} can be perpendicular or parallel to \mathbf{B} , but the expected polarization degree is rather low of $p \sim 1\%$ in the envelope and $p \ll 1\%$ in the central region. If it is the case, we should keep \mathbf{P} because we don't exactly know whether the grain longest axis is perpendicular to parallel to \mathbf{B} , or dust polarization does not trace the magnetic field direction. Until now, all observations show the high polarization level of $p > 5\%$ in protostellar envelopes, which requires dust grains to be SPM rather than PM. Therefore, one can infer \mathbf{B} -fields in the envelope by rotating the polarization orientation by 90°.

If the polarization pattern changes with wavelengths, it can originate from the change in IA of the emission source (Figures 10 and 9), or due to the change of the polarization mechanism. The latter case happens at optically thick wavelengths, but it requires the additional information of iron fractions locked inside dust grains before giving the conclusion as discussed in Section 10.8. Given this case, the po-

larization signal at optically thin wavelengths is due to polarization by dichroic emission while signal at optically thick wavelengths is due to polarization by dichroic extinction. Thus, we can rotate \mathbf{P} at optically thin wavelengths by 90° to infer \mathbf{B} , and keep \mathbf{P} at optically thick wavelengths. If the origin is the former scenario, large grains tend to have wrong IA due to slow internal relaxation and produce $\mathbf{P} \parallel \mathbf{B}$, while small grains can have efficient IA and produce $\mathbf{P} \perp \mathbf{B}$. For this case, we should keep \mathbf{P} at long wavelengths and rotate \mathbf{P} at shorter wavelengths by 90° to reconstruct magnetic fields structure.

In conclusion, we suggest that multi-wavelength polarimetric observations toward protostellar cores are required to accurately probe the dust, gas, and magnetic properties around protostars. A combined analysis of multi-wavelength polarization patterns and polarization degrees from synthetic observations with real observations will help us to first constrain amount of iron locked inside grains, then the grain alignment efficiency in studied environments, and lastly magnetic field geometry.

11 CONCLUSIONS

In our study, we have incorporated the magnetic properties of dust grains and the advanced grain alignment within the RAT paradigm into the POLARIS code. Then, we used the updated version of POLARIS to study the effects of iron inclusions on grain alignment and synthetic polarimetric observations of the protostellar core. Our findings are summarized as follows:

(i) Paramagnetic (PM) grains are not aligned with \mathbf{B} in the central region with high gas density of $n_{\text{H}} \geq 10^7 \text{ cm}^{-3}$ due to the grain randomization by gas collisions that occurs faster than the Larmor precession. They can be aligned with \mathbf{B} in the envelope but always have inefficient IA due to slow internal relaxation. In contrast, superparamagnetic (SPM) grains can have the magnetic alignment with efficient IA in the protostellar core due to the enhanced Barnett relaxation and Larmor precession by iron inclusions. The grain alignment efficiency increases with the increasing level of iron inclusions locked inside dust grains. However, in the protostellar central region, large grains of $a \geq 1 \mu\text{m}$ aligned with \mathbf{B} at low- J attractors always have slow internal relaxation and can align their longest axis perpendicular or parallel with \mathbf{B} .

(ii) The polarization patterns produced by both PM and SPM grains are uniform with $\mathbf{P} \perp \mathbf{B}$ at optically thin wavelengths when grains with slow internal relaxation have right IA. In contrast, when grains with slow internal relaxation have wrong IA, the polarization pattern produced by PM grains will be uniform in space but with $\mathbf{P} \parallel \mathbf{B}$. SPM grains with a moderate level of iron inclusions produce the uniform pattern with $\mathbf{P} \parallel \mathbf{B}$ at mm, but they produce complex ones at sub-mm with $\mathbf{P} \perp \mathbf{B}$ in the boundary of the envelope and in the inner ~ 300 au region, and $\mathbf{P} \parallel \mathbf{B}$ in the middle region of the core. The change in polarization pattern with the radial distance and wavelengths at optically thin wavelengths is due to the change in the internal alignment (IA) of the emission source. For SPM grains with a high level of iron inclusions, the polarization pattern is uniform, with $\mathbf{P} \perp \mathbf{B}$ from mm to sub-mm wavelengths because of the efficient grain alignment by the MRAT mechanism.

(iii) The polarization degree increases with increasing the abundance of iron present in dust, $N_{\text{cl}}\phi_{\text{sp}}$, but always decreases in the central region near the protostar. PM grains produce a low polarization of $p \sim 1\%$ in the envelope because of their inefficient grain alignment and a negligible polarization level in the inner 1000 au because they are not aligned with \mathbf{B} there. In contrast, SPM grains with a high level of iron inclusions can achieve perfect alignment by

the MRAT mechanism and produce a very high polarization degree up to $p \sim 40\%$ in the envelope. It successfully explains the detection of high $p \sim 40\%$ by ALMA toward Class 0 YSOs. The polarization fraction produced by SPM grains slightly decreases to $p < 10\%$ in the central region due to the reduced MRAT alignment efficiency in very dense environments.

(iv) The polarization by dichroic extinction at optically thick sub-mm wavelengths is less efficient than previously thought due to the weak alignment of VLGs in protostellar environments. We found that the inefficient grain alignment in dense regions induces much stronger reduction of $p(\%)$ with increasing intensity than the extinction effect by VLGs. Furthermore, dichroic extinction cannot become the main source of polarization at sub-mm and cannot induce the polarization flipping from $\mathbf{P} \perp \mathbf{B}$ at optically thin wavelengths to $\mathbf{P} \parallel \mathbf{B}$ at optically thick wavelengths, excepts for SPM grains with very high levels of iron inclusions. The estimated amount of iron inclusions locked inside dust is required to accurately quantify the efficiency of grain alignment and interpret polarimetric data observed at optically thick wavelengths.

(v) We found that if grains with wrong IA exist in protostellar cores, the change in IA of the polarized emission source can cause the 90° flipping of the polarization pattern between the envelope and the central region, and between mm and sub-mm. This feature happens at optically thin wavelengths, and be a potential mechanism for the variation of \mathbf{P} with distances and wavelengths. In addition, it also helps us to study the dynamic of grains with slow internal relaxation.

(vi) The polarization degree increases with increasing iron abundance in the dust but decreases with increasing the maximum grain size. VLGs must be SPM with the magnetic susceptibility enhanced by a factor of $\geq 10^3$ compared to PM to reproduce the observed level of polarization of $p \geq 1\%$ in the central region and high $p \sim 5-40\%$ in the envelope. Thus, it opens the new tool for tracing the level of iron inclusions locked inside dust grains via dust polarimetry. Knowing the magnetic properties of grains in dense environments is very important for probing the reability of studying magnetic fields by using dust polarization.

(vii) We find that, in addition to the increase of gas randomization toward protostars, the decrease of grain magnetic susceptibility with increasing dust temperature can also decrease the efficiency of external alignment (via the Larmor precession) and internal alignment (via Barnett relaxation). Therefore, although the RAT alignment increases toward the protostar, the decrease of grain magnetic susceptibility and increase of gas randomization leads to the rapid decrease of p toward the protostar. This is a new effect that can reproduce the polarization hole in the central region.

ACKNOWLEDGEMENTS

We thank Stefan Reissl for help with the Polaris code during the initial stage of this work. We thank the members of Vietnam Astrophysics Research Network (VARNET) for various discussion and comments. T.H. is supported by the National Research Foundation of Korea (NRF) grant funded by the Korea government (MSIT (No. 2019R1A2C1087045)). J.-G.K acknowledges support from the EA-COA Fellowship awarded by the East Asia Core Observatories Association.

DATA AVAILABILITY

The data underlying this article will be shared on reasonable request to the corresponding author.

REFERENCES

- Allen A., Li Z.-Y., Shu F. H., 2003, *ApJ*, **599**, 363
- Andersson B. G., Lazarian A., Vaillancourt J. E., 2015, *ARA&A*, **53**, 501
- Barnett S. J., 1915, *Phys. Rev.*, **6**, 239
- Bethell T. J., Chepurinov A., Lazarian A., Kim J., 2007, *ApJ*, **663**, 1055
- Bok B. J., 1977, *PASP*, **89**, 597
- Brauer R., Wolf S., Reissl S., 2016, *A&A*, **588**, A129
- Chandrasekhar S., Fermi E., 1953, *ApJ*, **118**, 113
- Cho J., Lazarian A., 2007, *The Astrophysical Journal*, **669**, 1085
- Clemens D. P., Yun J. L., Heyer M. H., 1991, *ApJS*, **75**, 877
- Clemens D. P., et al., 2020, *ApJS*, **249**, 23
- Collaboration P., et al., 2020, *Astronomy and Astrophysics*, **641**, A12
- Cox E. G., Harris R. J., Looney L. W., Li Z.-Y., Yang H., Tobin J. J., Stephens I., 2018, *The Astrophysical Journal*, **855**, 92
- Crutcher R. M., 2012, *ARA&A*, **50**, 29
- Davis Leverett J., Greenstein J. L., 1951, *ApJ*, **114**, 206
- Dent W. R. F., Pinte C., Cortes P. C., Ménard F., Hales A., Fomalont E., de Gregorio-Monsalvo I., 2019, *MNRAS*, **482**, L29
- Dolginov A. Z., Mitrofanov I. G., 1976, *Ap&SS*, **43**, 291
- Draine B. T., 1996, in Roberge W. G., Whittet D. C. B., eds, *Astronomical Society of the Pacific Conference Series Vol. 97, Polarimetry of the Interstellar Medium*. p. 16 ([arXiv:astro-ph/9603053](https://arxiv.org/abs/astro-ph/9603053))
- Draine B. T., Hensley B. S., 2021, *The Astrophysical Journal*, **909**, 94
- Draine B. T., Lazarian A., 1998, *ApJ*, **508**, 157
- Draine B. T., Weingartner J. C., 1996, *ApJ*, **470**, 551
- Dwek E., 2016, *The Astrophysical Journal*, **825**, 136
- Fanciullo L., et al., 2022, *Monthly Notices of the Royal Astronomical Society*, **512**, 1985
- Fiedler R. A., Mouschovias T. C., 1993, *ApJ*, **415**, 680
- Frank A., et al., 2014, in Beuther H., Klessen R. S., Dullemond C. P., Henning T., eds, *Protostars and Planets VI*. p. 451 ([arXiv:1402.3553](https://arxiv.org/abs/1402.3553)), doi:10.2458/azu_uapress_9780816531240-ch020
- Galametz M., et al., 2018, *A&A*, **616**, A139
- Galametz M., Maury A. J., Valdivia V., Testi L., Belloche A., André P., 2019, *A&A*, **632**, A5
- Girart J. M., Rao R., Marrone D. P., 2006, *Science*, **313**, 812
- Greenberg J. M., 1968, in Middlehurst B. M., Aller L. H., eds, *Nebulae and Interstellar Matter*. p. 221
- Guillet V., Hennebelle P., Forêts G. P. d., Marcowith A., Commerçon B., Marchand P., 2020, *Astronomy & Astrophysics*, **643**, A17
- Henning T., Wolf S., Launhardt R., Waters R., 2001, *ApJ*, **561**, 871
- Hensley B. S., Draine B. T., 2021, *The Astrophysical Journal*, **906**, 0
- Herranen J., Lazarian A., Hoang T., 2021, *ApJ*, **913**, 63
- Hirashita H., Li Z. Y., 2013, *MNRAS*, **434**, L70
- Hoang T., 2022, *The Astrophysical Journal*, **928**, 102
- Hoang T., Lazarian A., 2008, *Monthly Notices of the Royal Astronomical Society*, **388**, 117
- Hoang T., Lazarian A., 2009, *The Astrophysical Journal*, **697**, 1316
- Hoang T., Lazarian A., 2014, *Monthly Notices of the Royal Astronomical Society*, **438**, 680
- Hoang T., Lazarian A., 2016a, *The Astrophysical Journal*, **821**, 91
- Hoang T., Lazarian A., 2016b, *ApJ*, **831**, 159
- Hoang T., Tram L. N., Lee H., Ahn S.-H., 2019, *Nature*, **3**, 766–775
- Hoang T., Tram L. N., Lee H., Diep P. N., Ngoc N. B., 2021, *ApJ*, **908**, 218
- Hoang T., Tram L. N., Minh Phan V. H., Giang N. C., Phuong N. T., Dieu N. D., 2022, *AJ*, **164**, 248
- Hull C. L. H., Zhang Q., 2019, *Frontiers in Astronomy and Space Sciences*, **6**, 254
- Hull C. L. H., et al., 2014, *The Astrophysical Journal Supplement Series*, **213**, 13
- Jenkins E. B., 2009, *The Astrophysical Journal*, **700**, 1299
- Jones R. V., Spitzer Lyman J., 1967, *ApJ*, **147**, 943
- Kataoka A., Machida M. N., Tomisaka K., 2012, *ApJ*, **761**, 40
- Kataoka A., Tanaka H., Okuzumi S., Wada K., 2013, *A&A*, **557**, L4
- Ko C.-L., Liu H. B., Lai S.-P., Ching T.-C., Rao R., Girart J. M., 2020, *ApJ*, **889**, 172
- Krumholz M. R., Federrath C., 2019, *Frontiers in Astronomy and Space Sciences*, **6**, 7
- Kwon W., Looney L. W., Mundy L. G., Chiang H.-F., Kemball A. J., 2009, *ApJ*, **696**, 841
- Kwon W., Stephens I. W., Tobin J. J., Looney L. W., Li Z.-Y., van der Tak F. F. S., Crutcher R. M., 2019, *The Astrophysical Journal*, **879**, 25
- Lam K. H., Li Z.-Y., Chen C.-Y., Tomida K., Zhao B., 2019, *Monthly Notices of the Royal Astronomical Society*, **489**, 5326
- Lam K. H., Chen C.-Y., Li Z.-Y., Yang H., Cox E. G., Looney L. W., Stephens I., 2021, *MNRAS*, **507**, 608
- Lazarian A., 2007, *J. Quant. Spectrosc. Radiative Transfer*, **106**, 225
- Lazarian A., Hoang T., 2007, *MNRAS*, **378**, 910
- Lazarian A., Hoang T., 2008, *ApJL*, **676**, L25
- Lazarian A., Hoang T., 2019, *The Astrophysical Journal*, **883**, 122
- Lazarian A., Hoang T., 2021, *The Astrophysical Journal*, **908**, 12
- Lazarian A., Roberge W., 1997, *The Astrophysical Journal*, **484**, 230
- Lazarian A., Andersson B.-G., Hoang T., 2015, in Kolokolova L., Hough J., Levasseur-Regourd A.-C., eds, *Polarimetry of stars and planetary systems*. (New York: Cambridge Univ. Press), p. 81
- Le Gouellec V. J. M., et al., 2020, *A&A*, **644**, A11
- Leung C. M., 1985, in Black D. C., Matthews M. S., eds, *Protostars and Planets II*. pp 104–136
- Liu H. B., 2021, *The Astrophysical Journal*, **914**, 25
- Liu H. B., et al., 2016, *ApJ*, **821**, 41
- Lucy L. B., 1999, *A&A*, **344**, 282
- Martin P. G., 1974, *ApJ*, **187**, 461
- Mathis J. S., Rimpl W., Nordsieck K. H., 1977, *ApJ*, **217**, 425
- Mathis J. S., Mezger P. G., Panagia N., 1983, *A&A*, **500**, 259
- McKee C. F., Ostriker E. C., 2007, *ARA&A*, **45**, 565
- Miotello A., Testi L., Lodato G., Ricci L., Rosotti G., Brooks K., Maury A., Natta A., 2014, *A&A*, **567**, A32
- Morrish A. H., 2001, *The Physical Principles of Magnetism*
- Myers P. C., Basu S., 2021, *ApJ*, **917**, 35
- Nakano T., Nakamura T., 1978, *PASJ*, **30**, 671
- Okuzumi S., Tazaki R., 2019, *ApJ*, **878**, 132
- Okuzumi S., Tanaka H., Kobayashi H., Wada K., 2012, *ApJ*, **752**, 106
- Pattle K., Fissel L., 2019, *Frontiers in Astronomy and Space Sciences*, **6**, 15
- Planck Collaboration et al., 2015, *A&A*, **576**, A104
- Purcell E. M., 1979, *ApJ*, **231**, 404
- Rao R., Girart J. M., Marrone D. P., Lai S.-P., Schnee S., 2009, *ApJ*, **707**, 921
- Reissl S., Wolf S., Brauer R., 2016, *A&A*, **593**, A87
- Reissl S., Seifried D., Wolf S., Banerjee R., Klessen R. S., 2017, *Astronomy and Astrophysics*, **603**, A71
- Reissl S., Guillet V., Brauer R., Levrier F., Boulanger F., Klessen R. S., 2020, *A&A*, **640**, A118
- Roberge W. G., Degraff T. A., Flaherty J. E., 1993, *ApJ*, **418**, 287
- Sandell G., Aspin C., Duncan W. D., Russell A. P. G., Robson E. I., 1991, *ApJL*, **376**, L17
- Seifried D., Walch S., 2015, *MNRAS*, **452**, 2410
- Seifried D., Walch S., Reissl S., Ibáñez-Mejía J. C., 2018, [arXiv.org, astro-ph.GA](https://arxiv.org/abs/astro-ph.GA)
- Shu F. H., Adams F. C., Lizano S., 1987, *ARA&A*, **25**, 23
- Takahashi S., Saigo K., Ho P. T. P., Tomida K., 2012, *The Astrophysical Journal*, **752**, 10
- Tazaki R., Lazarian A., Nomura H., 2017, *ApJ*, **839**, 56
- Testi L., et al., 2014, in Beuther H., Klessen R. S., Dullemond C. P., Henning T., eds, *Protostars and Planets VI*. p. 339 ([arXiv:1402.1354](https://arxiv.org/abs/1402.1354)), doi:10.2458/azu_uapress_9780816531240-ch015
- Tram L. N., Hoang T., 2022, *arXiv e-prints*, p. [arXiv:2208.13195](https://arxiv.org/abs/2208.13195)
- Valdivia V., Maury A., Brauer R., Hennebelle P., Galametz M., Guillet V., Reissl S., 2019, *MNRAS*, **488**, 4897
- Wolf S., Launhardt R., Henning T., 2003, *The Astrophysical Journal*, **592**, 233

Wolf S., Launhardt R., Henning T., 2004, *Ap&SS*, 292, 239
 Yang H., 2021, *ApJ*, 911, 125

APPENDIX A: POLARIZED RADIATIVE TRANSFER EQUATION FOR THE STOKES PARAMETERS

The polarization state of radiation can be described by the Stokes vector $\mathbf{S} = (I \ Q \ U \ V)^T$ where Stokes I presents the total intensity, Stokes Q and U present the linear polarization, and Stokes V presents the circular polarization. The radiative transfer equation of the Stokes vector through a dusty environment is given by (Martin 1974, Reissl et al. 2016):

$$\frac{d}{ds} \begin{pmatrix} I \\ Q \\ U \\ V \end{pmatrix} = - \begin{pmatrix} \alpha_I & \alpha_Q & 0 & 0 \\ \alpha_Q & \alpha_I & 0 & 0 \\ 0 & 0 & \alpha_I & \kappa_Q \\ 0 & 0 & -\kappa_Q & \alpha_I \end{pmatrix} \begin{pmatrix} I \\ Q \\ U \\ V \end{pmatrix} + \begin{pmatrix} j_I \\ j_Q \\ 0 \\ 0 \end{pmatrix} \quad (\text{A1})$$

where α_I is the extinction coefficient over the grain size distribution:

$$\alpha_I = \int_{a_{\min}}^{a_{\max}} C_{\text{ext}}(a, \lambda) (dn/da) da, \quad (\text{A2})$$

α_Q is the linear polarization coefficient due to extinction:

$$\alpha_Q = \int_{a_{\text{align}}}^{a_{\text{max,Lar,JB}}} C_{\text{pol}}^{\text{ext}}(a, \lambda) (dn/da) da, \quad (\text{A3})$$

κ_Q is the circular polarization coefficient:

$$\kappa_Q = \int_{a_{\text{align}}}^{a_{\text{max,Lar,JB}}} C_{\text{circ}}(a, \lambda) (dn/da) da, \quad (\text{A4})$$

where $C_{\text{ext}}(a, \lambda)$ is the extinction cross section, $C_{\text{pol}}^{\text{ext}}(a, \lambda)$ is the linear polarization cross section, and $C_{\text{circ}}(a, \lambda)$ is the circular polarization cross section of the grain of size a and radiation wavelength λ .

Above, j_I and j_Q are the thermal dust emissivity from all dust grains and aligned dust grains, respectively. For dust grains at thermal equilibrium of temperature T_d , they are given by

$$j_I = \int_{a_{\min}}^{a_{\max}} C_{\text{abs}}(a, \lambda) B_{\lambda}(T_d(a)) (dn/da) da, \quad (\text{A5})$$

and

$$j_Q = \int_{a_{\text{align}}}^{a_{\text{max,Lar,JB}}} C_{\text{pol}}^{\text{abs}}(a, \lambda) B_{\lambda}(T_d(a)) (dn/da) da, \quad (\text{A6})$$

where $B_{\lambda}(T_d(a))$ is the Planck function at the grain temperature $T_d(a)$, $C_{\text{abs}}(a, \lambda)$ is the absorption cross section, and $C_{\text{pol}}^{\text{abs}}(a, \lambda)$ is the polarization cross section by absorption of the grain of size a .

The extinction cross section C_{ext} in Equation (A2) is calculated as :

$$C_{\text{ext}} = \frac{C_{\text{ext},x} + C_{\text{ext},y}}{2}, \quad (\text{A7})$$

and the linear polarization cross section $C_{\text{pol}}^{\text{ext}}$ in Equation (A3) is given by:

$$C_{\text{pol}}^{\text{ext}} = \frac{C_{\text{ext},x} - C_{\text{ext},y}}{2}. \quad (\text{A8})$$

$C_{\text{ext},x}$ and $C_{\text{ext},y}$ are the extinction cross section of grain of size for the electric field \mathbf{E} oscillating along x and y axis on the plane of sky, which is:

$$C_{\text{ext},x} = \langle C_{\text{ext}} \rangle + \frac{1}{3} R (C_{\text{ext},\parallel} - C_{\text{ext},\perp}), \quad (\text{A9})$$

and

$$C_{\text{ext},y} = \langle C_{\text{ext}} \rangle + \frac{1}{3} R (C_{\text{ext},\parallel} - C_{\text{ext},\perp}) (1 - 3 \sin^2 \psi) \quad (\text{A10})$$

The term $\langle C_{\text{ext}} \rangle$ is the extinction cross section over grain orientation in the grain frame, which is:

$$\langle C_{\text{ext}} \rangle = \frac{2C_{\text{ext},\parallel} + C_{\text{ext},\perp}}{3}, \quad (\text{A11})$$

where $C_{\text{ext},\parallel}$ and $C_{\text{ext},\perp}$ are the extinction cross section produced when the electric field \mathbf{E} oscillating along the major and minor axis of the grain, respectively.

Putting all terms above into Equations (A7) and (A8), one obtains

$$C_{\text{ext}} = \frac{(4 + 3R \cos^2 \psi - R) C_{\text{ext},\parallel}}{6} + \frac{(2 - 3 \cos^2 \psi + R) C_{\text{ext},\perp}}{6}, \quad (\text{A12})$$

and $C_{\text{pol}}^{\text{ext}}$ is:

$$C_{\text{pol}}^{\text{ext}} = \frac{(C_{\text{ext},\parallel} - C_{\text{ext},\perp}) R \sin^2 \psi}{2}, \quad (\text{A13})$$

where R is the Rayleigh reduction factor described in Section 4.1.3.

The values of C_{abs} , $C_{\text{pol}}^{\text{abs}}$, and C_{circ} have the same form with C_{ext} and $C_{\text{pol}}^{\text{ext}}$.

The term dn/da in Equation (A2) is the grain size distribution. Here we assume the typical power law of $dn/da = Ca^{-3.5}$ as in the diffuse ISM (the MRN distribution, Mathis et al. 1977) where C the normalization constant is determined by the gas-to-dust mass ratio:

$$\eta = \frac{\int_{a_{\min}}^{a_{\max}} m_d(a) n_H C a^{-3.5} da}{n_H m_H}, \quad (\text{A14})$$

where $m_d(a) = 4\pi\rho_s a^3/3$ is the mass of the grain of size a and axial ratio s .

APPENDIX B: VALIDITY OF THE ONE-CELL ASSUMPTION IN THE AZIMUTHAL DIRECTION

Figure B1 shows the comparison between the mean radiation field strength U (left panel) and the anisotropic degree γ_{rad} (right panel) as a function of distances to the central protostar using a spherical grid cell with $N_r \times N_\theta \times N_\phi = 250 \times 101 \times 1$ and $N_r \times N_\theta \times N_\phi = 250 \times 101 \times 60$, respectively. One can clearly see that U and γ_{rad} calculated from the model with $N_{\text{varphi}} = 1$ are nearly similar to the results from the model with $N_{\text{varphi}} = 60$ due to the spherical symmetry of the gas density model. Thus, using one cell along the azimuthal direction does not affect results of our adopted model.

APPENDIX C: GRAIN ALIGNMENT ALONG X AND Z DIRECTION

Figures C1 and C2 shows in detail the grain alignment of PM and SPM grains along the z and x direction, respectively (see the gas density map on x - z plane in the left panel of Figure 4). The upper left panel shows the minimum and maximum grain alignment size a_{align}

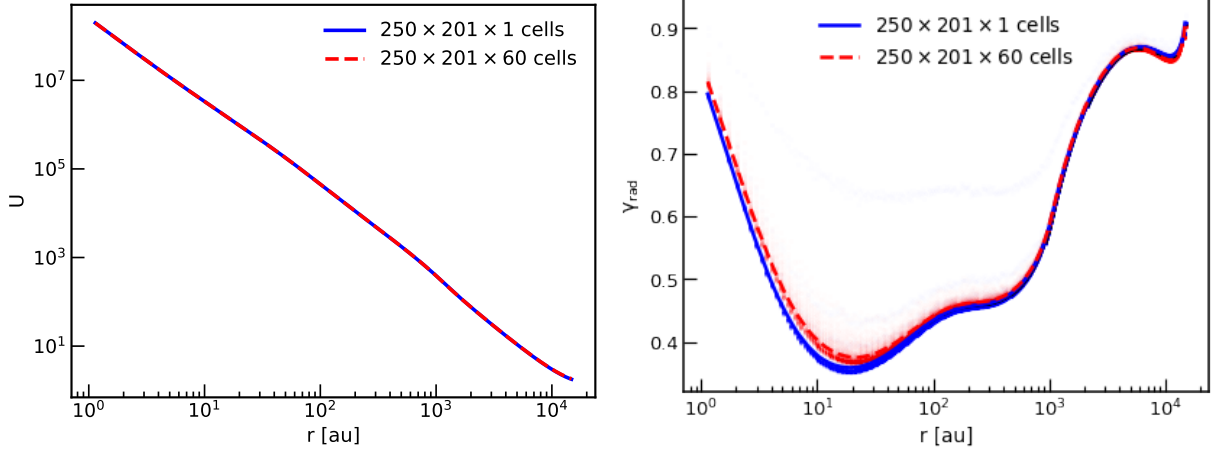


Figure B1. Variation of the mean radiation field strength U (left panel) and the anisotropic degree γ_{rad} with distances for the spherical grid model with $N_r \times N_\theta \times N_\phi = 250 \times 101 \times 1$ and $N_r \times N_\theta \times N_\phi = 250 \times 101 \times 60$, respectively. The grid model with one cell along the azimuthal direction gives a similar average U and γ_{rad} as the model with 60 cells on the azimuthal direction due to the symmetry of the gas density distribution inside the spherical core.

and $a_{\text{max},\text{JB}}^{\text{Lar}}$. The upper right and lower left panels show the minimum and maximum size for grains having fast internal relaxation at high- J and low- J attractors, respectively. The lower right panel shows the maximum size for grains having $f_{\text{high-}J} = 0.5$ and $f_{\text{high-}J} = 1$. In general, more large grains can be aligned with \mathbf{B} (i.e., larger range $a_{\text{align}} - a_{\text{max},\text{JB}}^{\text{Lar}}$), and have fast internal relaxation at high- J attractors (i.e., larger range $a_{\text{min},\text{AJ}}^{\text{high-}J} - a_{\text{max},\text{AJ}}^{\text{high-}J}$), in the envelope due to the reduced gas randomization. Iron inclusions allow more grains to have perfect magnetic alignment (i.e., $f_{\text{high-}J} = 1$) there due to the enhanced MRAT alignment.

However, one can see that the alignment efficiency of grains on the x direction is slightly smaller than grains on the z direction. It is because grains are spun up by RATs weaker in the area where the radiation field is perpendicular with B-field (Equation 18). As a result, the range of aligned dust grains having fast internal relaxation at high- J attraction reduces, i.e., larger a_{align} and larger $a_{\text{max},\text{AJ}}^{\text{high-}J}$, inducing lower $p(\%)$ on the equatorial as shown in the polarization maps in Section 6.

APPENDIX D: POLARIZATION MAP AT MILLIMETER WAVELENGTHS FOR $A_{\text{MAX}} = 100 \mu\text{m}$

Figure D1 shows the polarization patterns calculated at 2mm by model Ideal (first column) and model Realistic-rIA. The upper panels show the results in the envelope, and the lower panels show the results for the inner region of 1000 au around the protostar. The polarization patterns produced by both PM and SPM are uniform with $\mathbf{P} \perp \mathbf{B}$ from the envelope to the central region, assuming that grains with slow internal relaxation have right IA.

Figure D2 shows the similar results as Figure D1 but for model Realistic-wIA. Similar as the results at 870 μm (Figures 10 and 11), PM and SPM grains with $N_{\text{cl}} = 100$ produce the uniform polarization pattern with $\mathbf{P} \parallel \mathbf{B}$ from the envelope to the center due to the emission of VLGs with wrong IA at mm wavelengths. In contrast, SPM grains with $N_{\text{cl}} = 10^4$ produce the uniform pattern with $\mathbf{P} \perp \mathbf{B}$ in the entire protostellar core because of the efficient alignment of VLGs by the MRAT mechanism with \mathbf{B} .

APPENDIX E: POLARIZATION RESULTS FOR

$A_{\text{MAX}} = 10 \mu\text{m}$

E1 Iron Inclusions and Polarization Pattern

Figure E1 shows the polarization maps obtained from the outer envelope (first to third rows) to the central region (fourth to sixth rows) by model Realistic-rIA-a10 (Table 4). From the top to bottom, the observed wavelengths decrease from 2mm to 870 μm and 450 μm , while from the left to right, the results are for model Ideal-a10 (first column) and our models for PM and SPM grains with $N_{\text{cl}} = 100$ and $N_{\text{cl}} = 10^4$, assuming $\phi_{\text{sp}} = 0.005$. When all aligned dust grains have right IA, the polarization pattern (black segment) is uniform with $\mathbf{P} \perp \mathbf{B}$ from the envelope to the central region and does not change with wavelengths. The polarization degree (color code) decreases toward the center due to the inefficient magnetic alignment of grains in dense core.

Figure E2 shows similar results as Figure E1 but for model Realistic-wIA-a10. For PM grains (left column), the polarization pattern is quite uniform with $\mathbf{P} \parallel \mathbf{B}$ within 10000 au where most grains have wrong IA due to slow internal relaxation. However, beyond ~ 10000 au, \mathbf{P} flips 90° to $\mathbf{P} \perp \mathbf{B}$ because a small amount of micron-sized grains can have efficient IA by ISRF here (Figure 6, left panel). For SPM grains with $N_{\text{cl}} = 100$ (center column), the polarization pattern changes from $\mathbf{P} \perp \mathbf{B}$ beyond 5000 au (first three rows) to $\mathbf{P} \parallel \mathbf{B}$ in the inner region and changes back to $\mathbf{P} \perp \mathbf{B}$ within 200 au from the protostar (fourth to sixth rows) as a result of the complex distribution of grains with wrong and right IA from the center to the envelope (Figure 6, left panel). In contrast, SPM grains with $N_{\text{cl}} = 10^4$ (right column) produce much more simple polarization pattern, with $\mathbf{P} \perp \mathbf{B}$ in the entire protostellar core due to their efficient alignment with \mathbf{B} -fields.

One can see that that in the absence of VLGs, the polarization vectors do not rotate from $\mathbf{P} \parallel \mathbf{B}$ at mm to $\mathbf{P} \perp \mathbf{B}$ at sub-mm as in the case of model Realistic-wIA for SPM grains with $N_{\text{cl}} = 100$ and $a_{\text{max}} = 100 \mu\text{m}$ (Figures 10 and 11). It is because for the model with $a_{\text{max}} = 10 \mu\text{m}$, most all SPM grains have efficient IA and thus produce $\mathbf{P} \perp \mathbf{B}$ with wavelengths. In contrast, with the model of $a_{\text{max}} = 100 \mu\text{m}$, the main source for therma dust emission at mm (VLGs) arises from VLGs that have wrong IA due to slow internal relaxation, while the source of dust emission at sub-mm arises from

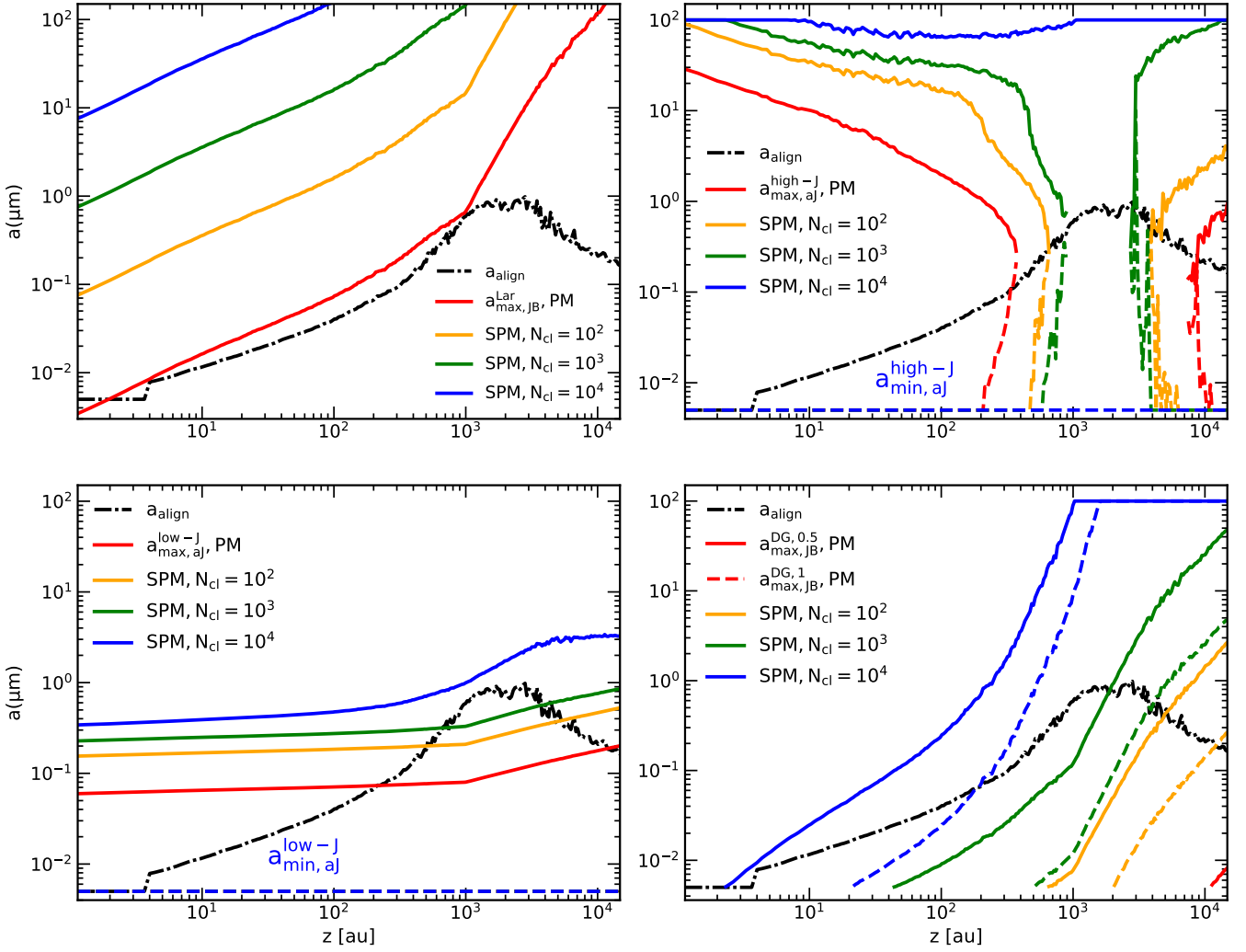


Figure C1. Variation along the z direction of the range of aligned dust grains $a_{\text{align}} - a_{\text{max},\text{JB}}^{\text{Lar}}$ (upper left panel), grains with fast internal relaxation at high and low- J attractors $a_{\text{min},\text{aJ}} - a_{\text{max},\text{aJ}}$ (upper right and lower left panels), and the maximum size that grains are aligned with \mathbf{B} by the MRAT mechanism, $a_{\text{max},\text{JB}}^{\text{DG},0.5}$, and $a_{\text{max},\text{JB}}^{\text{DG},1}$. The results are for PM and SPM grains with different N_{cl} . Generally, large grains can be aligned with \mathbf{B} and have fast internal relaxation in the envelope due to the reduced gas randomization. Iron inclusions enhance the internal and external alignment and help more large grains in the envelope to have perfect alignment with \mathbf{B} by MRAT alignment.

small (micron-size) grains that have efficient IA. Consequently, the polarization pattern changes with wavelengths due to the change in IA configuration of the emitting dust grains. This is an interesting feature that (may) be classified as an imprint of the grain growth process.

E2 Iron Inclusions and Intensity-dependent Polarization Degree

Figure E3 shows the effect of iron inclusions on the variation of $p(\%)$ with I/I_{max} at $870\mu\text{m}$ (upper panels) and $50\mu\text{m}$ (lower panels) for model Realistic-rIA-a10 (left column) and model Realistic-wIA-a10 (right column). The result for the ideal model of grain alignment is also plotted by the black dashed line for comparison. Similar as the results with $a_{\text{max}} = 100\mu\text{m}$, p always decreases with increasing I/I_{max} due to the decreased grain alignment efficiency in dense regions. The polarization degree produced by SPM grains with higher N_{cl} generally shows higher values thanks to the

enhanced grain alignment by the MRAT mechanism. In addition, if aligned dust grains have wrong IA, one will obtain the "valley-polarization hole" caused by the cancelling effect of polarized emission due to the co-existence of grains with right and wrong IA (left column).

E3 Iron Inclusions and Wavelength-dependent Polarization Degree

Figure E4 shows the effect of iron inclusions on the polarization curve $p(\lambda)$ observed at $d_{\text{proj}} = 200\text{ au}$ (upper panels) and $d_{\text{proj}} = 12000\text{ au}$ (lower panels) for model Realistic-rIA-a10 (left columns) and Realistic-wIA-a10 (right columns). Without the presence of VLGs (Section 9), the polarization degree is nearly independent with wavelengths from $89\mu\text{m}$ to 2mm in both the envelope and the central region. The slight rise of $p(\%)$ from 2mm to $89\mu\text{m}$ produced by SPM grains with $N_{\text{cl}} < 1000$ for model Realistic-wIA-a10 is

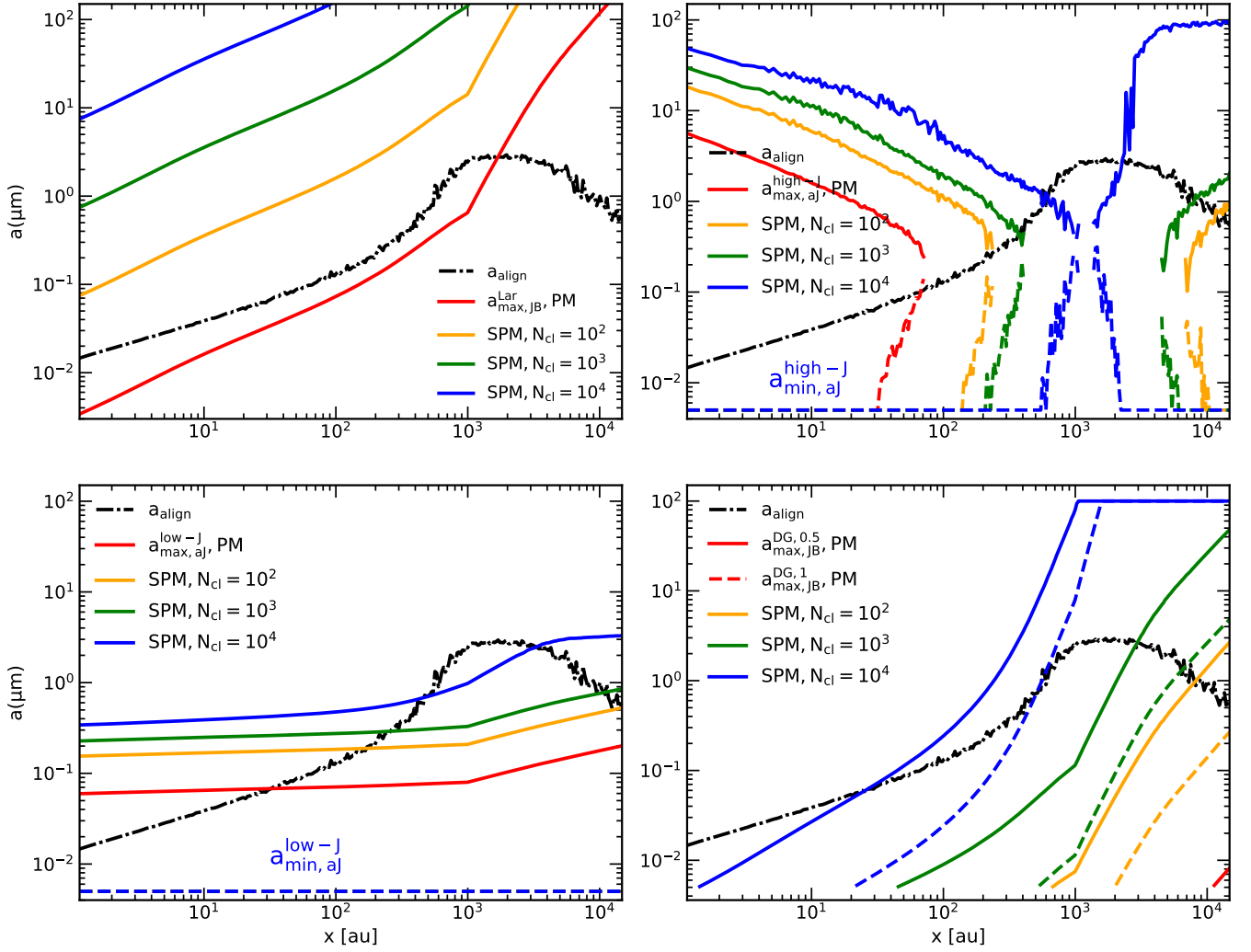


Figure C2. Similar as Figure C1 but for grains on the x direction. The variation of grain alignment along x is similar to along the z -direction, but alignment efficiency is weaker, i.e., narrow alignment range of $a_{\text{align}} - a_{\text{max,aj}}^{\text{Lar}}$ (upper left panel) and narrow range of grains with fast internal relaxation at high- J attractors $a_{\text{min,aj}}^{\text{high-J}} - a_{\text{max,aj}}^{\text{high-J}}$ (upper right panel), due to the reduced RATs efficiency in the area where $\mathbf{k} \perp \mathbf{B}$.

due to the increased emission of micron-sized grains with efficient IA at short wavelengths.

This paper has been typeset from a \LaTeX file prepared by the author.

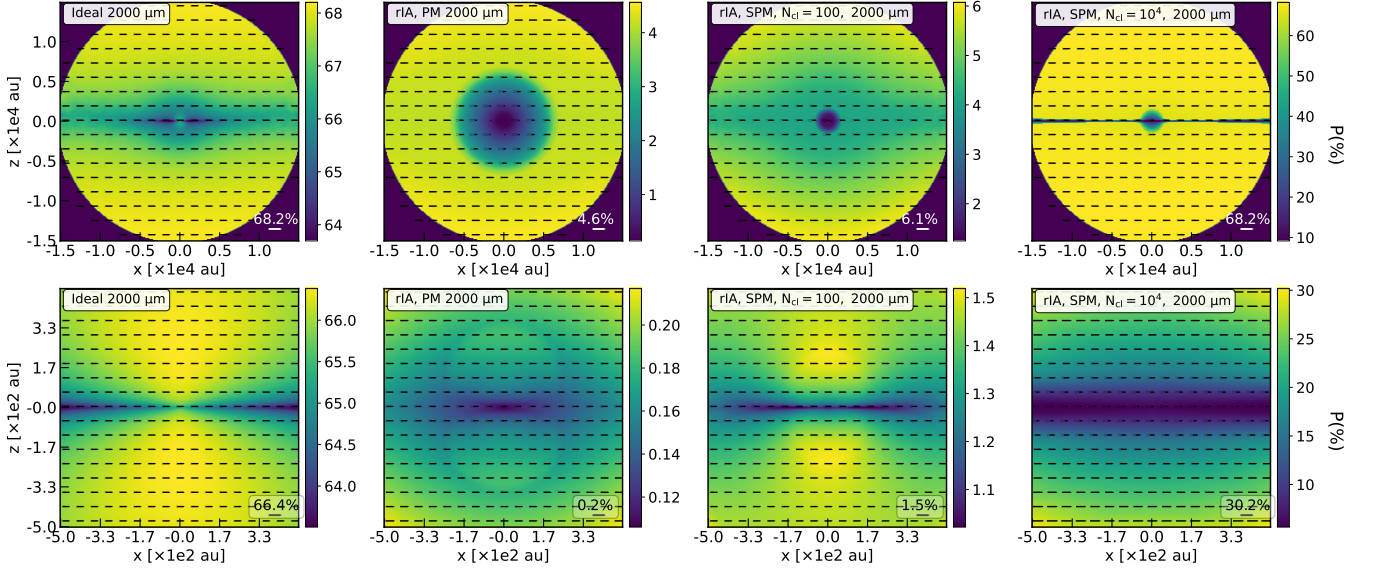


Figure D1. Polarization maps calculated at 2 mm for model Ideal (first column) and model Realistic–rIA. The upper panels show the results in the envelope, and the lower panels are for the inner 1000 au around the protostar. The polarization patterns for both PM and SPM grains are uniform with $\mathbf{P} \perp \mathbf{B}$ from the envelope to the center when grains with slow internal alignment have right IA. The polarization degree in our model decreases inward due to the inefficient alignment of grains with \mathbf{B} .

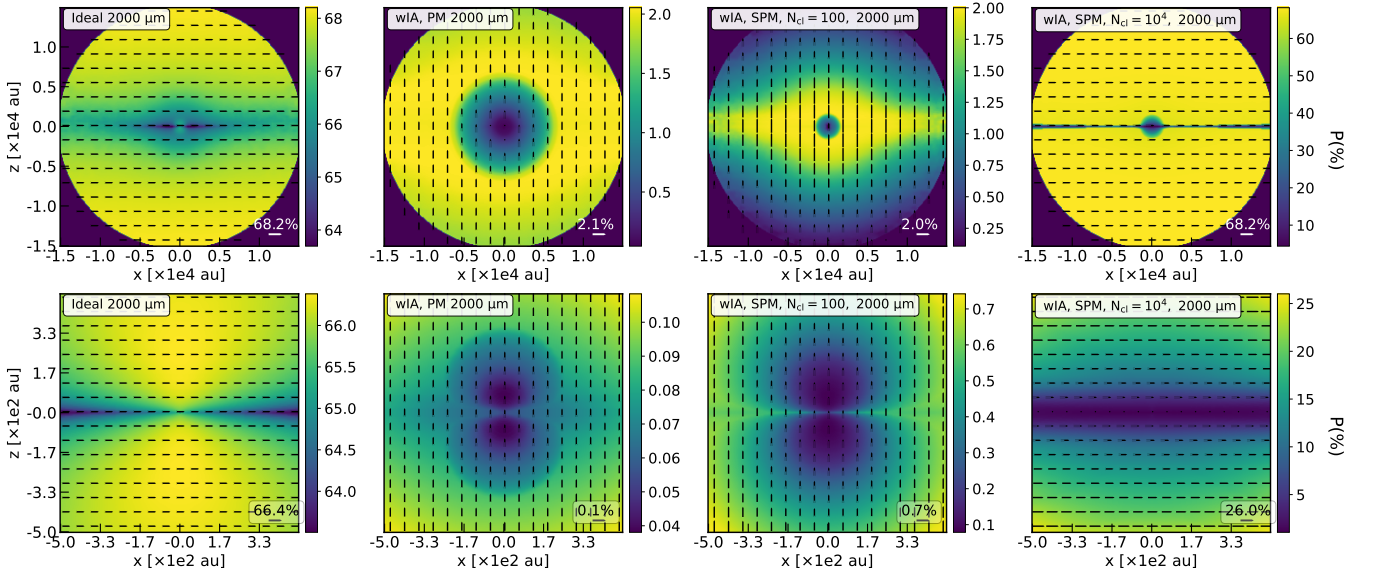


Figure D2. Similar as Figure D1 but for model Realistic–wIA. At mm, PM and SPM grains with low $N_{cl} = 100$ produce the uniform polarization pattern with $\mathbf{P} \parallel \mathbf{B}$ in the entire protostellar core due to the emission of grains with wrong IA. In contrast, SPM grains with high $N_{cl} = 10^4$ produce polarization vectors $\mathbf{P} \perp \mathbf{B}$ as model Ideal.

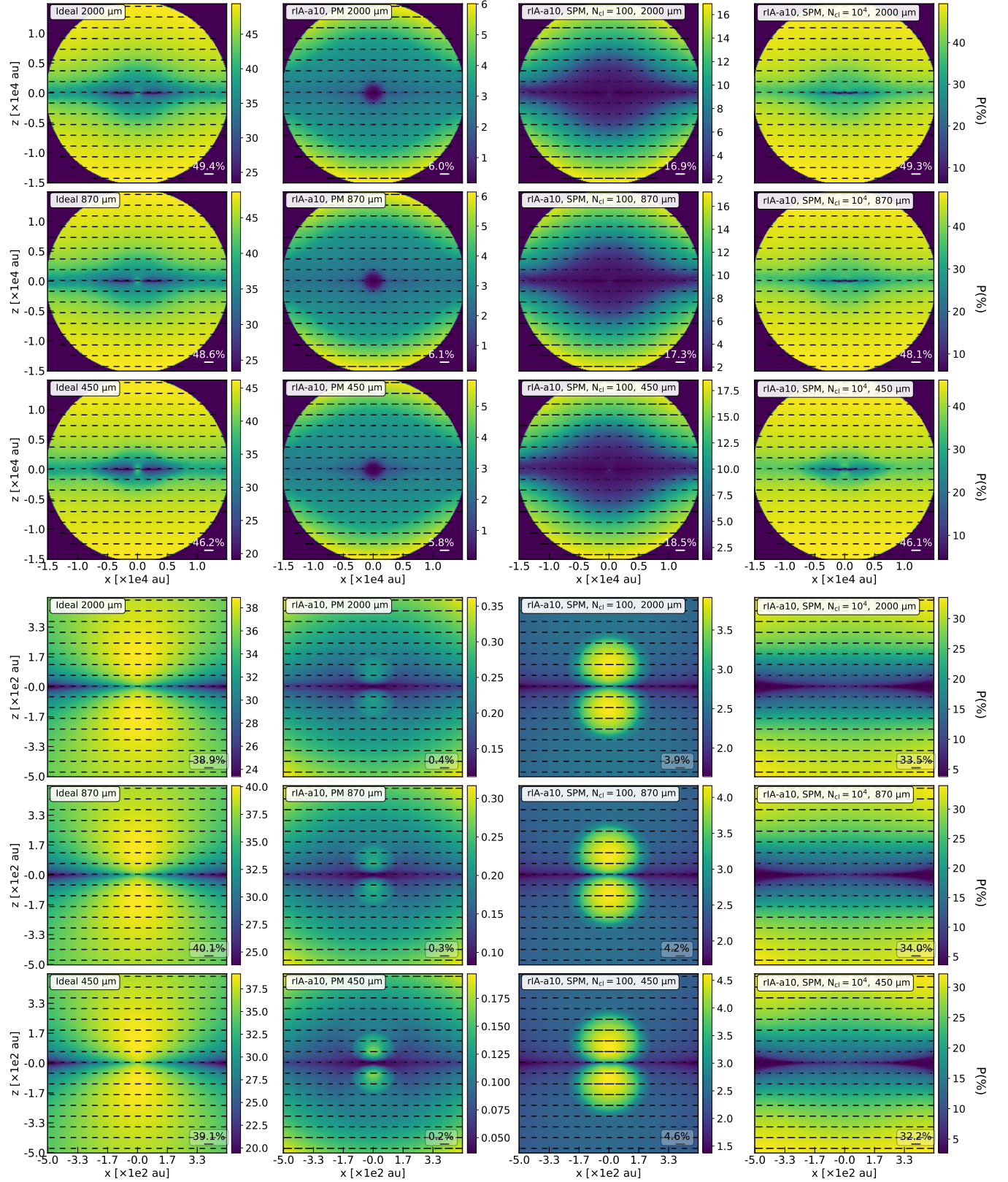


Figure E1. Polarization maps calculated in the envelope (first to third rows) and the inner region of 1000 au (fourth to sixth rows) for model Ideal–a10 (first column) and model Realistic–riA–a10 (second to fourth columns) (Table 4). For model that all grains have right IA, the polarization pattern is uniform in space with $\mathbf{P} \perp \mathbf{B}$ from 2mm to 450 μm .

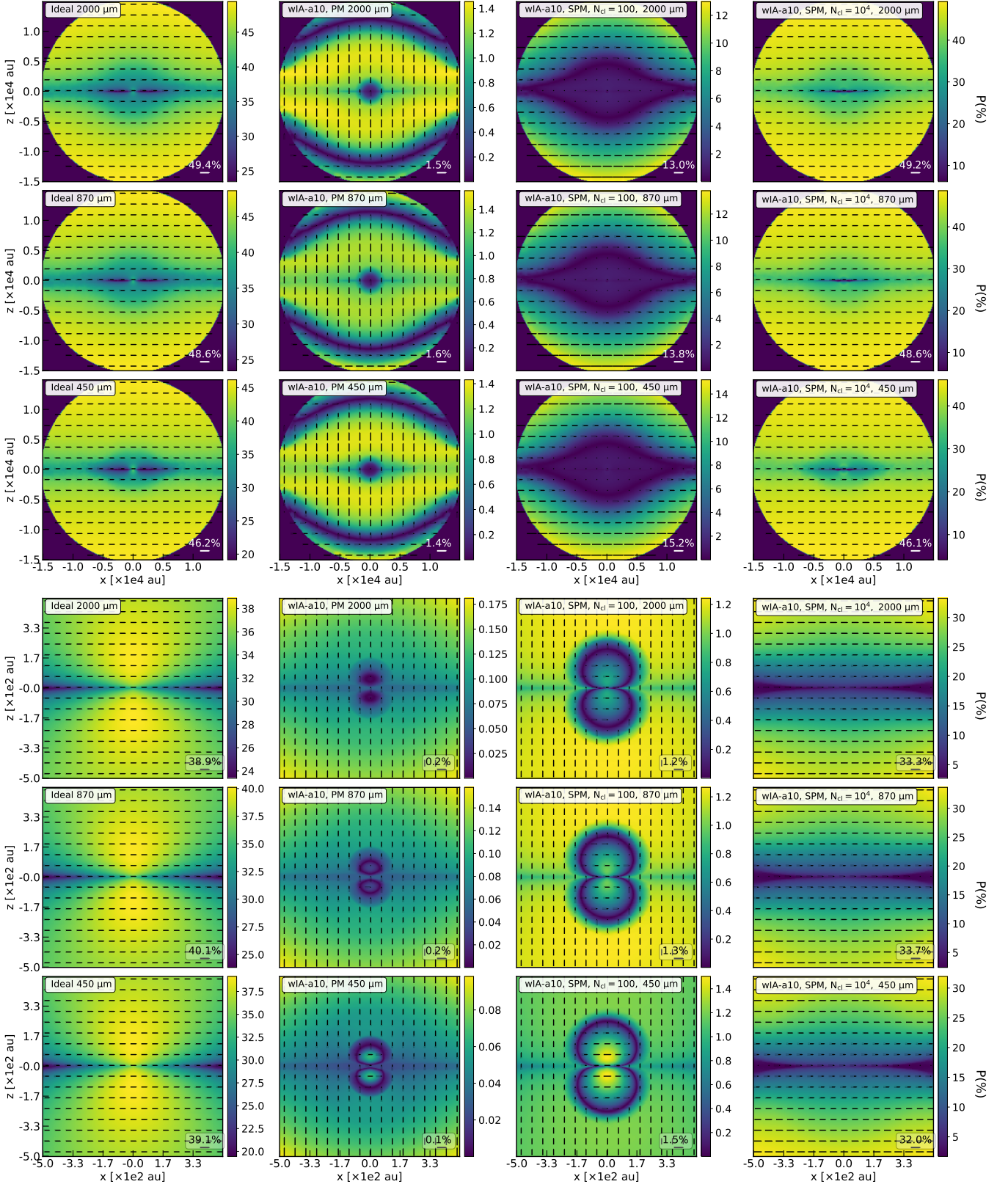


Figure E2. Similar as Figure E1 but for model Realistic-wIA-a10. In the presence of grains with wrong IA, at fixed wavelengths, the polarization pattern produced by PM and SPM grains with low N_{cl} changes from $\mathbf{P} \perp \mathbf{B}$ in the outer boundary of the envelope to $\mathbf{P} \parallel \mathbf{B}$ in the inner region and flips again to $\mathbf{P} \perp \mathbf{B}$ around protostar. This complicated polarization pattern is due to the complex distribution of grains with right and wrong IA in the protostellar core (e.g., Figure 6). For SPM grains with high $N_{cl} = 10^4$, \mathbf{P} is uniform with $\mathbf{P} \perp \mathbf{B}$. In addition, the polarization patterns in the entire protostellar core do not change with wavelengths for $a_{max} = 10 \mu\text{m}$.

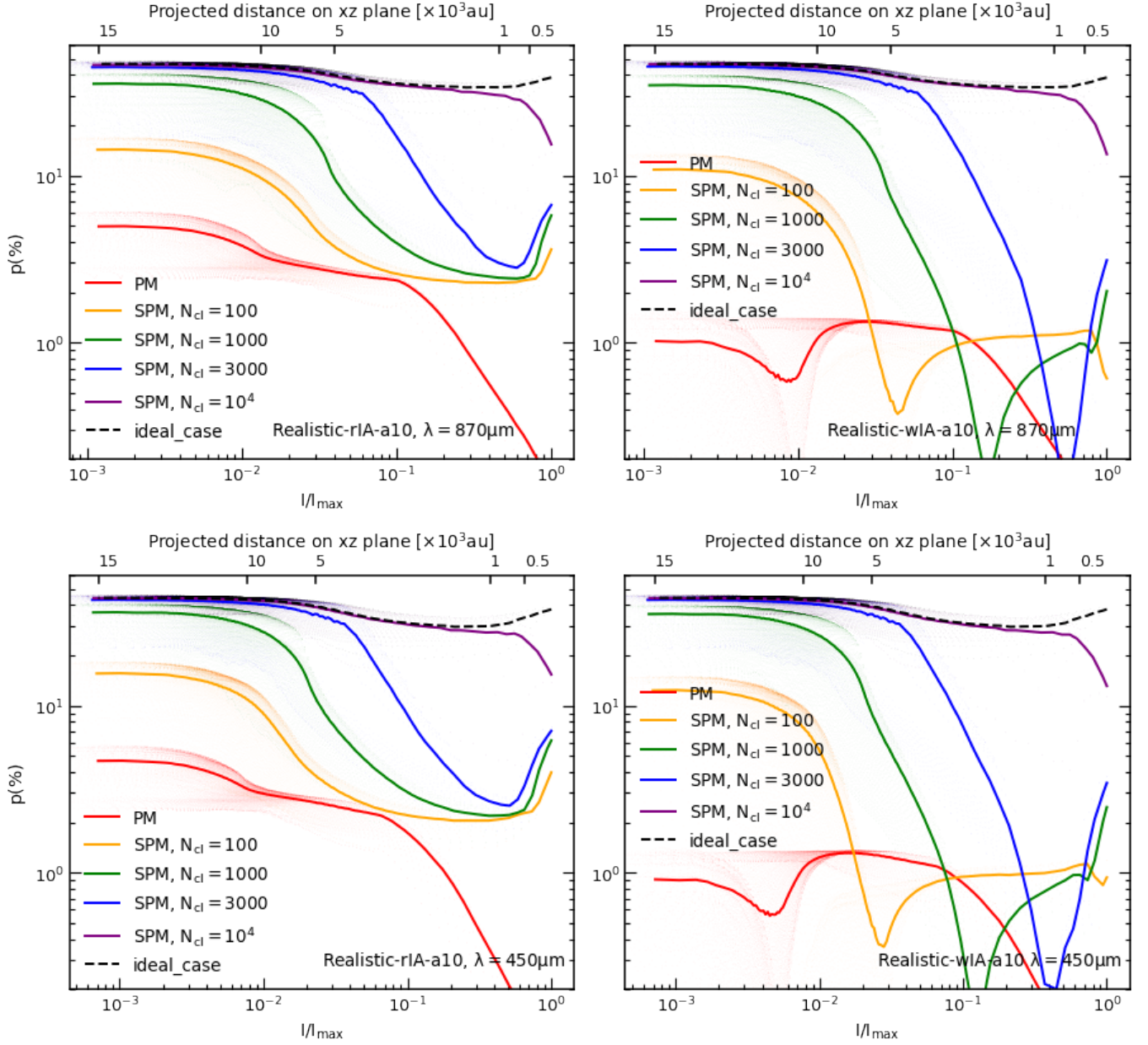


Figure E3. Effect of iron inclusions on the variation of p with I/I_{\max} at $870\,\mu\text{m}$ (upper panels) and $450\,\mu\text{m}$ (lower panels) for model Realistic-rIA-a10 (left column) and Realistic-wIA-a10 (right column). The polarization degree from our models always decreases with increasing intensity due to the reduced grain alignment efficiency in dense environments, and generally increases with increasing N_{cl} . If grains with wrong IA are present in the core, one will obtain the "valley-polarization hole" on $p - I/I_{\max}$ curve caused by the cancelling effect of polarized emission from grains with right and wrong IA.

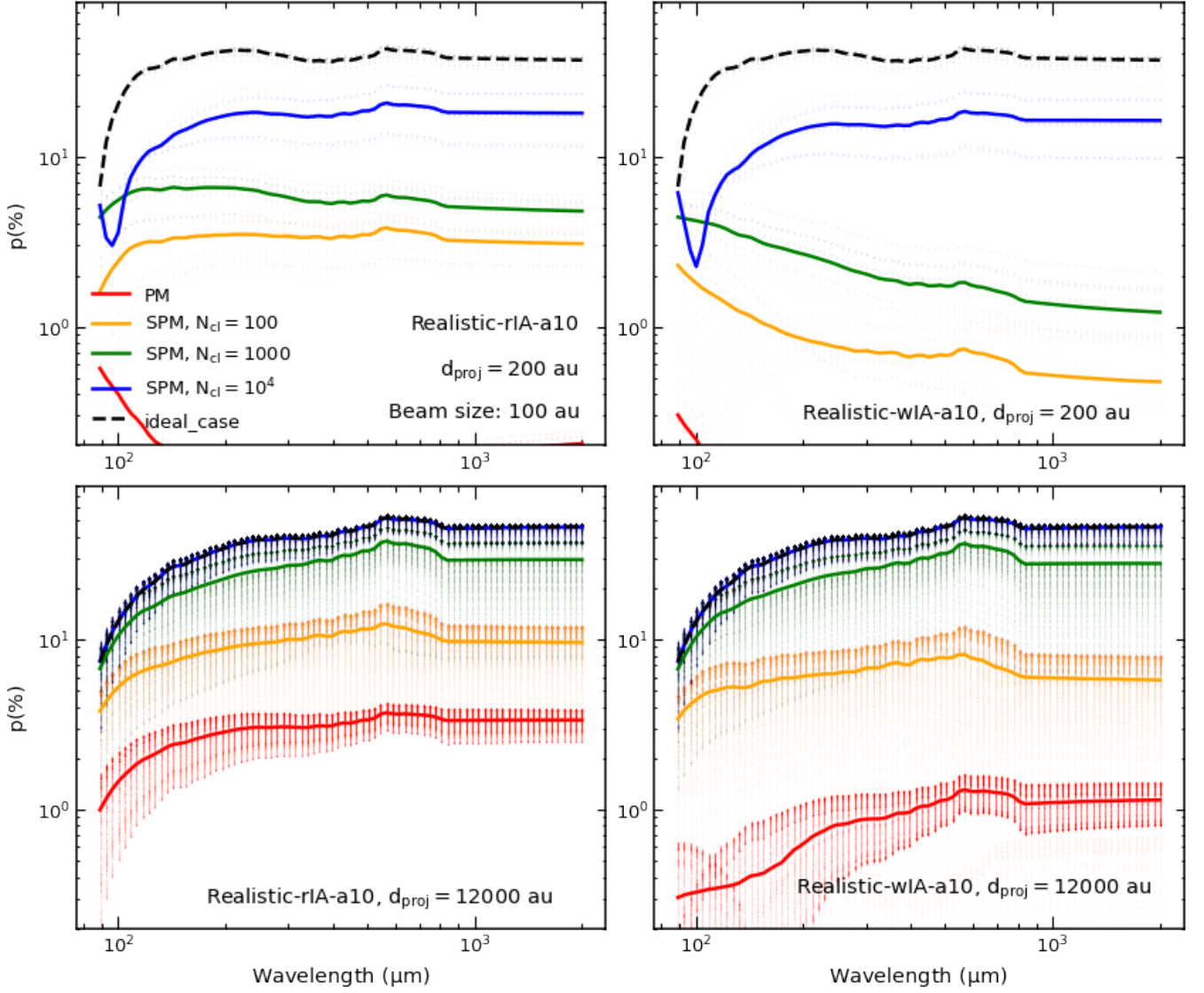


Figure E4. Effect of iron inclusions on the polarization curve $p(\lambda)$ from 2 mm to $89 \mu\text{m}$ calculated at $d_{\text{proj}} = 200$ au (upper panels) and $d_{\text{proj}} = 2000$ au (lower panels) for model Realistic-rIA-a10 (left column) and Realistic-wIA-a10 (right column). With $a_{\text{max}} = 10 \mu\text{m}$, the polarization degree is nearly independent with mm/sub-mm wavelengths in both the central region and the envelope (corresponds to the independence of the polarization patterns with wavelengths in Figures E1 and E2).